EPFL

Thèse n° 9675

Importance of 3D radiative transfer effects on high-resolution NO_2 remote sensing in cities

Présentée le 27 avril 2022

Faculté de l'environnement naturel, architectural et construit
Laboratoire de télédétection environnementale
Programme doctoral en génie civil et environnement

pour l'obtention du grade de Docteur ès Sciences

par

Marc Damien SCHWÄRZEL

Acceptée sur proposition du jury

Prof. D. Tuia, président du jury
Prof. A. Berne, Prof. D. Brunner, directeurs de thèse
Dr M. Van Roozendael, rapporteur
Prof. A. Damm-Reiser, rapporteur
Dr S. Takahama, rapporteur

École
polytechnique
fédérale
de Lausanne

2022

All models are wrong,
but some are useful.
–George E. P. Box

Acknowledgements

At an early academic career stage, nothing works without a good supervision and a healthy working environment. In my case it was rather an excellent supervision from many competent colleagues and a good working environment at Empa. Therefore, I would like to express my gratitude to the many people and organizations involved in my journey.

I especially want to thank Gerrit Kuhlmann for being present, ready to help, patient, and very qualified. With his insights and help I learned very important bases in my research field. The quality of my publications and my thesis has only been achieved thanks to our numerous discussions and his valuable inputs. I also want to thank Dominik Brunner for increasing the quality and the communication quality of my work with numerous inputs for my publications and talks. He was also very supportive in the diverse projects I had, e.g., joining an ESA joint training course on atmospheric composition in Romania[1]. Furthermore I want to thank Brigitte Buchmann, the PI of the project, for taking time guiding me through the academic/research life at Empa.

I want to thank Alexis Berne, my supervisor at EPFL, for the soft supervision and the support in my project. Sometimes having many supervisors is a struggle, but Alexis trusted Gerrit and Dominik, and I am convinced that many conflicts were therewith avoided. Thank you for our regular discussions that helped me sorting and highlighting the important aspects of my work and also for proofreading my thesis.

During my stay(s) in Munich, project and working colleagues from the Meteorological Institute at the Ludwig Maximilian University of Munich (LMU) supported me in many ways. I especially want to thank Claudia Emde and Fabian Jakub for technical support and interesting specific discussions at LMU. I also want to thank Bernhard Mayer for the fruitful discussions and accepting our collaboration, and all the other colleagues in Munich for contribution to a successful academic exchange.

I am particularly thankful to my colleagues at the Air Pollution/Environmental Technology Laboratory at Empa for the great working environment. I enjoyed coming daily to Empa,

[1]https://atmostraining.info/index.php/2019/08/01/first-joint-training-course-on-atmospheric-composition/#more-118, last access 13 January 2022.

especially with the generally difficult COVID-19 pandemic situation.

My private life also needs some credit. I want to thank Seraina Wyss who supported me morally during my thesis and serving as a guinea pig for presentation training. Thank you to my family Ruedi, Beatrice, and Fabienne for moral support.

Finally, I want to acknowledge the Swiss National Science Foundation (SNSF) for funding my project (grant no. 172533) and my stay in Munich.

Dübendorf, April 8, 2022 Marc Schwärzel

Abstract

Urban air quality is a major concern in the context of human health since cities are at the same time emission hot spots and home to a large fraction of the world's population. Airborne imaging spectrometers may be a valuable addition to traditional air pollution monitoring networks as they can be used to map the spatial distribution of air pollutants such as nitrogen dioxide (NO_2) at high spatial resolution. Retrieving NO_2 concentrations from such measurements requires information about the average path of the photons collected by the spectrometer, which depends on observation and solar geometry, surface reflectance, and atmospheric scattering by air molecules and aerosols. This is usually accounted for by an air mass factor (AMF) computed with a radiative transfer model (RTM). Since scattering processes are not homogeneous in the atmosphere, so-called box AMFs representing the AMFs for defined spatial grid boxes are calculated before being integrated to a total AMF. The actual 1D-layer AMFs (only account for vertical inhomogeneity of the atmosphere), traditionally used for NO_2 retrievals, are not sufficient to resolve the high spatial variability of NO_2 concentrations in cities. As a result, measured NO_2 distributions of such measurements are much smoother than one would expect from looking at other mapping techniques in cities (e.g., high-resolution dispersion model simulations of NO_2). Therefore, I study the impact of 3D and buildings in the radiative transfer calculation on the NO_2 concentrations retrieved from ground-based and airborne spectrometers. In this study, AMFs are computed with the MYSTIC solver of the libRadtran RTM. MYSTIC uses a Monte Carlo technique to simulate photons journeys in the atmosphere and retrieve different radiative transfer (RT) quantities. The MYSTIC AMF module has been extended to be a 3D radiative transfer code and is now able to account for complex ground features (i.e., buildings). With synthetic case studies, I demonstrate the importance of considering 3D features in the radiative transfer calculations. Considering the 3D path of photons in the retrievals affects the spatial structure of the sensitivity of ground-based and airborne instruments. Considering 3D radiative transfer features induces a horizontal smearing of the sensitivity, especially of features with high NO_2 concentrations, as for example exhaust plumes or roads. Buildings reduce the instrument sensitivity to the near-surface NO_2 and induce noticeable random noise that might explain part of the uncertainty observed in the retrieved NO_2 maps. Moreover, I implemented the developed features in the Empa APEX NO_2 retrieval algorithm and retrieved vertical column densities (VCD) and high-resolution near-surface NO_2 concentrations from the APEX airborne imaging spectrometer. Finally I evaluate the quality of near-surface NO_2 concentration maps by comparing the results to in situ measurements. The new modules are essential for analyzing NO_2 remote sensing data over cities as they will reduce systematic errors and spatially better allocate measurements. This pioneer research is intended to help the community identifying problems that might appear with the fast increase in horizontal resolution of satellites. The possible high resolution maps obtained from high-resolution trace gas remote sensing can support city authorities and different teams in the scientific community to access high-resolution ground NO_2 concentrations maps, to study urban air quality and to support urban development planning.

KEYWORDS – air pollution; radiative transfer modelling; trace gas remote sensing; nitrogen dioxide; airborne spectroscopy; photons paths in the urban canopy

Résumé

La qualité de l'air urbain est une préoccupation majeure dans le contexte de la santé humaine, car les villes sont à la fois des zones d'émissions et le lieu de résidence et d'activité d'une grande partie de la population mondiale. Les spectromètres aéroportés peuvent constituer un complément précieux aux réseaux traditionnels de mesure de surveillance de la pollution de l'air, car ils peuvent être utilisés pour cartographier la distribution spatiale de polluants atmosphériques tels que le dioxyde d'azote (NO_2) à haute résolution spatiale. La récupération des concentrations de NO_2 à partir de telles mesures nécessite des informations sur le trajet moyen des photons collectés par le spectromètre, qui dépendent de la géométrie de la mesure, de la position du soleil, de l'absorption et de la réflectance de la surface, ainsi que de l'absorption et de la diffusion atmosphérique par les molécules de l'air et par les aérosols. Ce phénomène est généralement pris en compte par un facteur appelé "air mass factor" (AMF) calculé à l'aide d'un modèle de transfert radiatif (MTR). Comme les processus de diffusion ne sont pas homogènes dans l'atmosphère, des box-AMF, représentant les AMF pour des cellules spatiales définies, sont calculés avant d'être intégrés en AMF total. Les AMF de couches 1D (i.e. 1D-layer AMFs, qui ne tiennent compte que de l'inhomogénéité verticale de l'atmosphère), traditionnellement utilisés pour la récupération de NO_2, ne sont pas suffisants pour résoudre la grande variabilité spatiale des concentrations de NO_2 dans les villes. Par conséquent, les distributions de NO_2 mesurées sont beaucoup plus lisses qu'attendues et comparées à d'autres techniques de cartographie de polluants dans les villes (par exemple, de modèles de dispersion de NO_2 à haute résolution). Par conséquent, j'étudie l'impact de la 3D et des bâtiments dans le calcul du transfert radiatif sur le NO_2 récupéré à partir de spectromètres terrestres et aéroportés. Dans cette étude, les AMFs sont calculés avec le solutionneur MYSTIC du MTR libRadtran. MYSTIC utilise une méthode de Monte Carlo pour simuler les trajets des photons dans l'atmosphère, pour ainsi calculer différentes quantités de transfert radiatif (TR). Le module AMF de MYSTIC a été étendu pour devenir un code de TR 3D et est maintenant capable de tenir compte de caractéristiques complexes du sol (par exemple les bâtiments). À l'aide d'études de cas synthétiques, je démontre l'importance de la prise en compte des caractéristiques 3D dans les calculs de transfert radiatif. La prise en compte de la trajectoire 3D des photons dans la récupération affecte la structure spatiale de la sensibilité de l'instrument, qu'il soit terrestre ou aéroporté et induit un lissage horizontal de la sensibilité, en particulier pour les éléments à forte concentration de NO_2, comme par exemple les panaches de pollution ou les routes. Les bâtiments réduisent, quant à eux, la sensibilité des instruments à la concentration de NO_2 proche du sol et induisent un bruit aléatoire important qui pourrait expliquer une partie de l'incertitude dans les cartes de NO_2. J'ai également implémenté les modules développés dans la routine de récupération de gaz à l'état de traces de l'Empa et récupéré des concentrations contenues dans une colonne atmospherique donnée (appelé VCD) et des cartes à haute résolution de NO_2 proche de la surface à partir du spectromètre aéroporté APEX. Enfin, j'évalue la qualité des cartes de NO_2 proche de la surface en comparant les résultats aux mesures in situ. Les nouveaux modules sont essentiels pour l'analyse des données de télédétection de NO_2 au-dessus des villes, car ils permettront de réduire les erreurs systématiques et de mieux comprendre la composante spatiale des concentrations. Cette recherche pionnière a pour but d'aider la communauté à identifier les problèmes qui pourraient apparaître avec l'augmentation rapide de la résolution horizontale des satellites. Les cartes à haute résolution obtenues par la télédétection de gaz à l'état de trace peuvent aider les autorités municipales et différentes équipes de la communauté scientifique à accéder à des cartes de concentration de NO_2 afin d'étudier la qualité de l'air urbain et de soutenir la planification du développement urbain.

Mots-clés – pollution de l'air ; modélisation du transfert radiatif ; télédétection des gaz à l'état de traces ; dioxyde d'azote ; spectroscopie aéroportée ; trajectoires des photons dans la canopée urbaine

Contents

Important acronyms

Acronym	Description
AMF	Air mass factor
AOD	Aerosol optical depth
APEX	Airborne Prism EXperiment - airborne spectrometer
DOAS	Differential optical absorption spectroscopy
HAPS	High-altitude pseudo-satellite
libRadtran	Library for radiative transfer - radiative transfer model
MYSTIC	A Monte Carlo radiative transfer solver
NO_2	Nitrogen dioxide
NSC	Near-surface concentration
PBL	Planetary boundary layer
PM	Particulate matter
RT	Radiative transfer
RTM	Radiative transfer model
SAA	Solar azimuth angle
SBI	Spectrolite Breadboard Instrument - airborne spectrometer
SCD	Slant column density
SZA	Solar zenith angle
TOA	Top of the atmosphere
VAA	Viewing azimuth angle
VCD	Vertical column density
VZA	Viewing zenith angle

List of Figures

List of Tables

1 General introduction

1.1 Air pollution

Air pollution presents a major threat to health and climate, as it is the largest environmental cause of disease and premature death in the world today (Landrigan et al., 2018). Short or long-term-exposure to air pollution can have severe impacts on human health with e.g., inflammation of the entire respiratory system or premature death (Bell et al., 2006; Beelen et al., 2014; Landrigan et al., 2018) and on ecosystems (Bouwman et al., 2002). It can also increase the effects of other environmental stresses such as pollen-induced respiratory allergies (D'Amato et al., 2014) and heat stress (Fischer and Schär, 2010; García-Herrera et al., 2010). Nitrogen dioxide (NO_2), ozone (O_3), and particulate matter (PM) are considered as the most harmful air pollutants in Europe (Guerreiro et al., 2014), as air pollution concentration limits, which are set by European and Swiss legislations, are frequently exceeded in urban areas where population densities are highest (BAFU, 2020). The World Health Organization recently updated its recommendations for the air pollution concentration limits (World Health Organization, 2021).

1.2 Nitrogen dioxide and its spatial and temporal variability in cities

Nitrogen oxides ($NO_x = NO + NO_2$) are important precursors of tropospheric ozone and particulate matter that respectively play an important role in the formation of photochemical smog and wintertime air pollution (Crutzen, 1970; Steinbacher et al., 2007). The NO_X air pollutants are mainly emitted by road traffic but also by residential heating, industrial facilities, power plants and some other sources. Because of these localized emissions and the short lifetime of a few hours (Schaub et al., 2007), NO_2 concentrations are characterized by high spatial and temporal variability, especially when atmospheric mixing is low. Because of this spatial variability, estimations of population exposure to NO_2 remains very challenging, and high-resolution pollution maps are therefore needed.

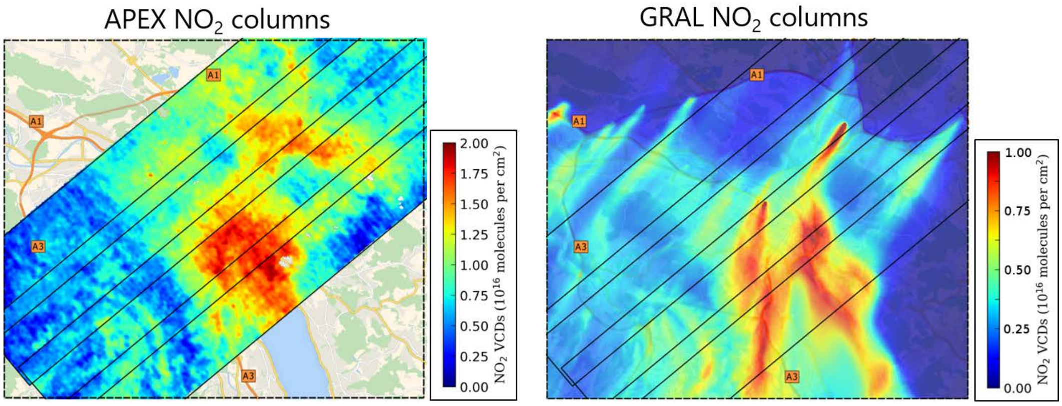

Figure 1.1 – NO_2 columns retrieved from APEX imaging spectrometer and from city-scale GRAMM/GRAL modelling system (preliminary results shown by Kuhlmann et al. (2017)).

The number of in-situ NO_2 measurement sites strongly increased in the past 40 years with the setup of regional and national monitoring networks such as NABEL in Switzerland (BAFU, 2020), but the density of the measurement network is still too low for resolving the spatial variability of the air pollutant within cities. One approach to overcome these limitations is to combine in-situ observations with geostatistical models such as land-use-regression models to generate city-wide maps (e.g. Mueller et al., 2015), but the sparseness of the measurement network limits the accuracy of the method. Deploying numerous low cost air quality sensors has also been exploited, but the precision and stability of the measurement remains a major obstacle (Heimann et al., 2015). Other alternatives are ground-based remote sensing instruments including concurrent multi-axis Differential Optical Absorption Spectroscopy (DOAS) and tomographic long-path DOAS systems (Leigh et al., 2007; Pöhler, 2010). These instruments present the disadvantage that they usually measure trace gases above the urban canopy, and therefore miss the important close-to-ground NO_2 concentrations. Furthermore, they measure the integrated NO_2 along the line of sight and to obtain accurate high-resolution air pollution maps for a city, a large amount of theses costly instruments and scanning paths are required (e.g., applying the Tomographic Differential Optical Absorption Spectroscopy - Tom-DOAS - technique described in Pundt et al. (2005)). Alternatively, air pollution dispersion models have been used to produce high-resolution air pollution maps at city scale (Berchet et al., 2017). This method critically depends on the quality of the underlying emission inventories and is computationally expensive to run over long periods (see NO_2 columns from the GRAMM-GRAL dispersion model on the right illustration in Fig. 1.1).

Alternative measurement methods are imaging spectrometers placed on satellite, aircraft, drones, and in the future possibly on High-Altitude Pseudo-Satellites (HAPS). An example is the airborne prism experiment (APEX) imaging spectrometer, which has been developed by a Swiss-Belgian consortium on behalf of the European Space Agency (ESA) and has been flown on an aircraft in various projects on behalf of the European remote-sensing community (Schaepman et al., 2015). The APEX instrument was one of the first airborne spectrometers

Table 1.1 – APEX specifications

Parameter	Visible & Near Infrared
Wavelength range	380-970 nm
Spectral resolution (FWHM)	0.6-6.3 nm
FOV across track	28 °
IFOV across track	0.0028 °
Swath width	3100 m
Ground speed	72 m s^{-1}
Exposure time	58 ms
δSCD detection limit	3.3 x 10^{15} molec cm^{-2}
Scanning	Push broom
Across-track spatial resolution	60 m
Along-track spatial resolution	80 m
Scanning	Push broom

suited for high-resolution NO_2 remote sensing in cities (Popp et al., 2012) (e.g., see NO_2 columns from the APEX instrument on the left illustration in Fig.1.1). Several APEX campaigns were conducted, where the instrument was installed on board of an German Aerospace Center (DLR) Dornier Do-228 airplane and flown over Zurich (between 2010 and 2016), Munich (in 2016) and other European cities to retrieve NO_2 maps with a spatial resolution of 50 m for the NO_2 product. Airborne spectroscopy presents the advantage of resolving the spatial distribution of the pollutant, but uncertainty in the measurement and in the retrieval remains large. Furthermore the relation between the measured column and the ground concentration is complex and the measurement only represents a snap-shot of the distribution at the time of the flight.

1.3 NO_2 retrieval from airborne spectrometers

Trace gas measurement with a spectrometer require a series of steps to retrieve the targeted trace gas quantity, here NO_2. First, the incoming light is split in discrete wavelength bands by a dispersion medium (e.g., prism, grating), then sensors, composed of e.g., CCD detectors, measure several wavelength bands. Once digitized, the measured signal is undergoing a complex spectral in-flight and off-line calibration (Hueni et al., 2013), from which a calibrated high resolution spectrum is obtained for every observed pixel. APEX is a push broom scanner, which means that it simultaneously measures several pixels in the across-track direction of flight (with a field of view of 28°) (see details in Tab. 1.1 based on https://earth.esa.int/web/eoportal/airborne-sensors/apex, last access 6 January 2022 and on Tack et al. (2019)).

The most commonly applied trace gas retrieval method in the ultraviolet, visible and near-infrared spectral range is the differential optical absorption spectroscopy (DOAS) (Platt and Stutz, 2008). It fits absorption cross sections of trace gases to the logarithm of the ratio of the measured spectrum and a reference spectrum based on the Beer-Lambert law. Broadband variations in the spectrum by atmospheric and ground effects are accounted for by a low order polynomial. The DOAS retrieval is usually computed using a dedicated retrieval software. The data used in this PhD thesis, was obtained using the Empa APEX NO_2 retrieval algorithm (also used in Kuhlmann et al., 2022) using the flexDOAS python DOAS retrieval library (Kuhlmann, 2021). The result of the DOAS retrieval is a slant column density (SCD), which is the integrated trace gas concentration along the optical path of the sunlight scattered towards the spectrometer (see SCD sketch in Fig. 1.2a). The optical path depends on the illumination and viewing geometry, on absorption and scattering by air molecules, aerosols and clouds, and surface reflectance.

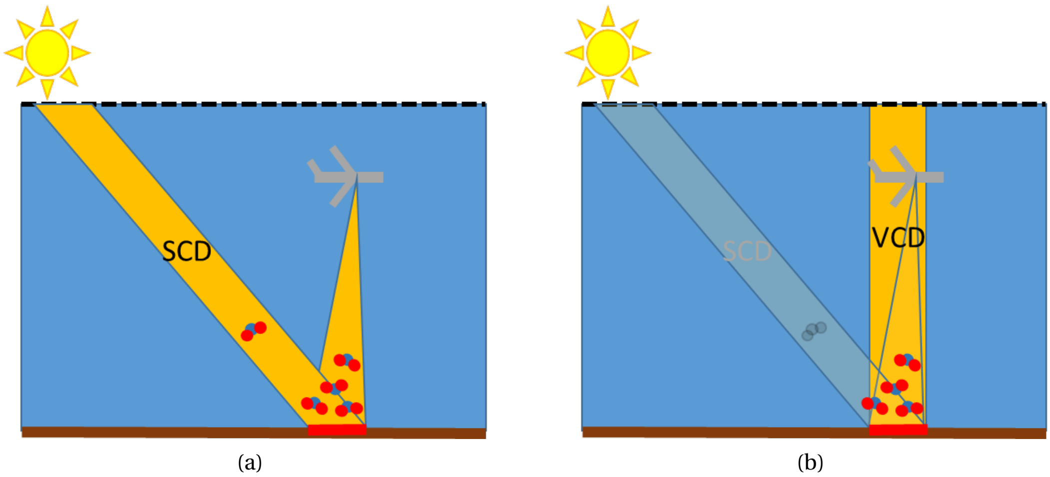

Figure 1.2 – Schematic representation of (a) SCDs and (b) VCDs for an airborne spectroscopy measurement with NO_2 molecules in red and blue.

A physically more meaningful quantity that is independent of the measurement geometry is the vertical column density (VCD), which is the integrated trace gas concentration from the ground to the top of the considered atmosphere (e.g., the top of the atmosphere - TOA) (see VCD sketch in Fig. 1.2b). The ratio between SCD and VCD is defined as an air mass factor (AMF) (Solomon et al., 1987), which can be computed with a radiative transfer model (RTM). To account for the vertical variability in atmospheric properties, AMFs are usually computed for discrete vertical layers (layer AMFs) assuming horizontal homogeneity (Palmer et al., 2001; Wagner et al., 2007; Rozanov and Rozanov, 2010).

1.4 Radiative transfer models in NO_2 retrievals

In the past decades, numerous RTMs have been developed with the possibility to calculate one-dimensional layer AMFs (e.g., Berk et al., 1999; Postylyakov, 2004; Rozanov et al., 2005; Wagner et al., 2007; Spurr et al., 2001; Iwabuchi, 2006; Iwabuchi and Okamura, 2017). The computation of layer AMFs is implemented in most trace gas retrieval algorithms for satellite and ground-based observations applied today (Boersma et al., 2011; Irie et al., 2011; Wenig et al., 2008; Wu et al., 2013). An alternative method is direct fitting, which is used in few algorithms (e.g., GODFIT in Lerot et al., 2010). The direct fitting method directly fits simulated backscattered spectral radiances from a radiative transfer model to measured radiances. For some specific applications, e.g., where the computation time for AMFs calculation is critical, precalculated lookup tables are used (e.g. Lee et al., 2009; Boersma et al., 2011).

In this PhD-thesis, I will use the Monte carlo code for the phYSically correct Tracing of photons In Cloudy atmospheres (MYSTIC) as solver of the libRadtran RTM (www.libradtran.org, last access: 25.11.2021), which uses a Monte Carlo method to compute photon paths in the atmosphere, accounting for scattering and absorption processes in the atmosphere and on the ground. More details about MYSTIC will be presented in Chap. 2.

1.5 Challenges in NO_2 retrievals from airborne spectrometers

Current airborne imaging spectroscopy retrievals assume horizontal homogeneity of ground and atmospheric absorption and scattering properties, and therefore apply 1D-layer AMFs to convert the measured SCDs to VCDs. High resolution air pollution maps obtained from airborne spectroscopy appear much smoother than what would be expected from the instrument spatial resolution and compared to maps from other air pollution mapping techniques (e.g., NO_2 columns from APEX compared to maps obtained from the GRAMM-GRAL city-scale dispersion model in Fig. 1.1, respectively left and right). Small structures (e.g., smaller roads) are not visible on airborne spectrometer maps, even if the spatial resolution for NO_2 is supposed to be lower than 50 x 50 m^2.

Part of the observed smearing of the NO_2 distribution may be attributable to atmospheric dispersion and mixing processes or to fast chemical processes affecting the NO_2 concentrations. Another part of the smearing may be induced by 3D radiative transfer effects, i.e., by the many different paths the photons followed through the atmosphere before being collected by the spectrometer. These paths are affected by illumination and measurement geometries, by atmospheric scattering processes, and by ground reflecting properties. The measured signals thus contain information collected along all these 3D paths.

In cities, absorption and reflecting properties affecting photons paths are highly inhomogeneous (e.g., NO_2 distribution or building shapes), and therefore the induced radiative transfer effects need to be studied, in the broader scope of airborne spectroscopy trace gas mapping. Those effects could become even more relevant as the spatial resolution of instruments increases with time. Newly launched satellites and future satellite missions with higher spatial resolution (e.g., GHGsat, Sentinel-2, CO2M, Nitrosat) might also face the described smearing issue in the future.

1.6 Research question and approach

The PhD thesis focuses on radiative transfer effects on airborne spectroscopy retrievals, especially the effects of 3D radiative transfer including the effects of buildings on the AMF calculation. The thesis is a core part of the HighNOCs project, whose goals were to develop and advance methods to derive high-resolution near-surface concentrations of NO_2 from airborne imaging spectrometers. The overarching goal of the project was to provide reliable, city-wide maps (<50×50 m^2 resolution) of near-surface NO_2 concentrations in order to better understand their sources and spatial distribution, and to evaluate the potential of this novel technology to complement ground-based urban air pollutant observations. MY specific contributions to the project were to validate and extend an existing radiative transfer model with 3D capabilities and to perform sensitivity studies. The goal of my work was to describe, understand and quantify the part of the smearing observed in NO_2 columns, obtained from airborne spectrometers flying over cities, attributed to the radiative transfer (see previous section and the smeared NO_2 maps in Fig. 1.1 left). Therefore, the following specific questions were formulated and addressed in this PhD thesis:

- What are the effects of 3D radiative transfer on airborne and ground based trace gas remote sensing?
- How do the buildings and the 3D optical path affect airborne imaging spectrometers?
- Can we improve the NO_2 VCDs and the near-surface concentration products if 3D and buildings radiative transfer effects are accounted for in the trace gas retrieval from airborne spectrometers?

To answer these questions, the MYSTIC radiative transfer solver had to be extended, first to include 3D-box AMFs calculations and then the urban canopy, to be able to account for complex surface properties (i.e., buildings). These extensions are fundamental to study the radiative transfer effects on NO_2 retrieval from airborne spectroscopy. Before addressing the individual questions presented above, I compare the 3D implementation with 1D-layer AMFs simulations from MYSTIC and other RTMs to verify the implementations and validate the developed MYSTIC modules. The implementation of 1D-layer and 3D-box AMFs into MYSTIC and its comparison with other RTM are presented in Chap. 3.

To study the 3D radiative transfer (RT) effects on trace gas retrieval from airborne spectroscopy, I first show the spatial distribution of the sensitivity of different instruments. Assessing the spatial structure of the sensitivity distribution, helps to identify the underlying physical processes that we will address in the following chapters. Second, I set up synthetic, close to real, scenarios, to study the effects in controlled environments, where I define the numerous parameters affecting the photon paths in the atmosphere. I also show the effect of 3D-box AMFs on the calculation of total AMFs. These synthetic case studies are presented in Chap. 3 and 4.

To evaluate the importance of considering and studying the effects of buildings in trace gas retrievals, I included buildings in the synthetic scenarios, and compared the simulations with and without buildings. In high-resolution simulations including real building data, I show the underlying physical processes impacting the radiative transfer calculation. The effects of buildings are presented in Chap. 4.

Last but not least, in Chap. 5, I implement the developed RT features in the Empa APEX NO_2 retrieval algorithm and evaluate the effects of 3D RT and buildings on real APEX measurements from different measurement campaigns over Zurich. I also compare the near-surface NO_2 concentration product calculated with the developed modules with immission measurement at air pollution monitoring sites.

1.7 Outline

This thesis is composed of a general methods section and three main chapters (chapter 3, 4 and 5). The content of chapters 3 and 4 was published in Atmospheric Measurement Techniques (Schwaerzel et al., 2020, 2021), and the content of chapter 5 is planned to be submitted to a peer-reviewed scientific journal after the submission of the thesis. In chapters 3, 4, and 5 , I used the "we" pronoun, as it was (and will be) used in the published versions. Chapters 2, 3,4 and 5 are briefly described here:

Chapter 2: General methods

The General methods chapter will present the methods and mathematical background shared by the chapters 3, 4 and 5. Methods specific to a given chapter will be addressed there.

Chapter 3: Three-dimensional radiative transfer effects on airborne and ground-based trace gas remote sensing

This chapter presents the validation of the 1D-layer AMFs module and its extension to 3D in the MYSTIC radiative transfer solver of the libRadtran RTM. The implementation was validated against a model cross-validation study from Wagner et al. (2007). The developed 3D module is shown to have an impact on the sensitivity distribution of ground-based MAX-DOAS measurements and airborne spectrometers. Additionally, we demonstrate the 3D effect on emission estimation from a synthetic NO_2 plume imaged by an airborne spectrometer.

Chapter 4: Impact of 3D radiative transfer on airborne NO_2 imaging remote sensing over cities with buildings

This chapter describes the implementation of complex surface properties (buildings) into the MYSTIC radiative transfer solver. I also present the spatial distribution of the sensitivity to NO_2 of an airborne spectrometer and study the impact of the 3D-box AMFs and Urban Canopy MYSTIC modules on the NO_2 retrieval with synthetic but realistic case studies over Zurich.

Chapter 5: APEX airborne spectrometer NO_2 VCDs and near-surface NO_2 concentrations obtained with 3D-box AMFs

In this chapter, I apply the developed 3D radiative transfer and the buildings features to real APEX data obtained during measurement campaigns in 2010, 2013 and 2016 in Zurich. I also compute ground NO_2 concentrations combining APEX airborne spectrometer data, 3D-box AMFs with buildings and NO_2 a priori fields from the GRAMM-GRAL city-scale dispersion model, and compared the results with near-surface NO_2 concentrations measurements at air pollution measurement sites in the canton of Zurich.

2 General methods

2.1 Trace gas remote sensing and radiative transfer

Atmospheric trace gases can be measured with ground-, aircraft- and space-based spectrometers that measure solar irradiance scattered into the line of sight of the instrument (see Fig. 2.1). In the case of aircraft- and space-based observations, a large fraction of the measured photons usually travels along a main path (thick dashed line) representing a single reflection at the surface. In the case of ground-based observations, the measured photons must follow a path with at least a single atmospheric scattering into the line of sight of the instrument (except for direct sun observations). Atmospheric scattering and absorption are determined by the distribution and properties of molecules, aerosols, and clouds and they depend on the wavelength of the radiation. Molecular scattering is particularly important in the UV range of the spectrum. Photons are absorbed by the trace gases along the optical path from the sun to the instrument. For a weak absorber such as NO_2, the abundance of the trace gas along the mean optical path can be obtained by fitting an absorption cross section to the measured spectrum, which we introduced previously as the DOAS technique. Thereby, the mean optical path is the total length of all individual photon paths divided by the number of photons collected by the instrument. The result of the fit is a SCD, which is defined as

$$SCD = \int_{path} c(l)\,dl, \tag{2.1}$$

with trace gas concentration c and pathlength dl. SCDs are not an intrinsic property of the atmosphere, since they depend on the illumination and viewing geometry. Therefore, for most applications, the main quantity of interest is the VCD. It is defined as

$$VCD = \int_{z_0}^{z_{top}} c(z)\,dz, \tag{2.2}$$

with surface elevation z_0 and top of the considered atmosphere z_{top}. The conversion factor from SCDs to VCDs was introduced as an AMF.

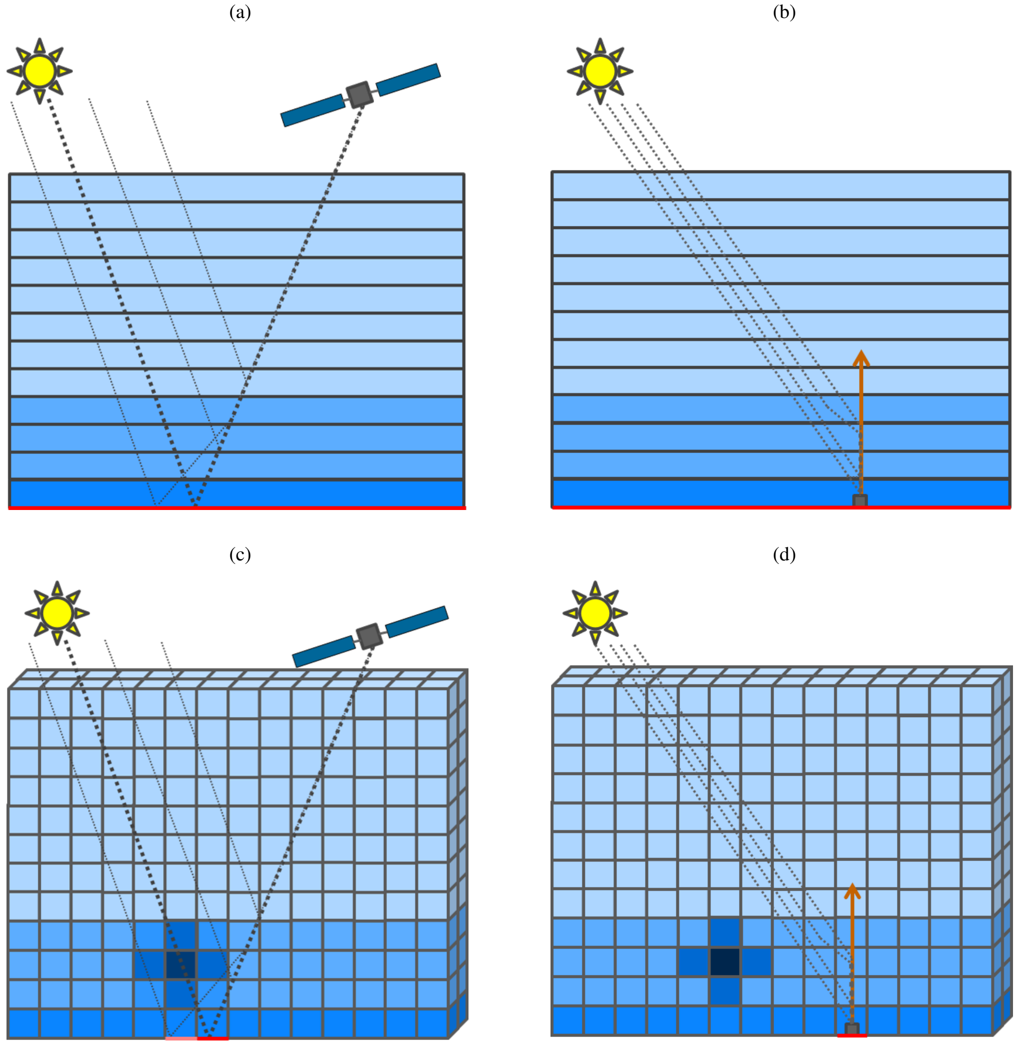

Figure 2.1 – Illustration of the difference between 1D-layer (a,b) and 3D-box AMFs (c,d) for two scenarios with downward-looking spaceborne (a,c) and upward-looking (orange array) ground-based (b,d) observations. Selected photon paths are shown as dashed lines and the thick dashed line represents the main optical path. 1D-layer AMFs implicitly assume horizontally uniform atmospheric and surface properties, whereas 3D-box AMFs fully account for both vertical and horizontal variability.

2.2 Air mass factors

The air mass factor (AMF) can be defined as

$$AMF = \frac{SCD}{VCD}, \tag{2.3}$$

ignoring the path-dependency of the absorption cross section. The AMF can be computed for a vertically varying atmosphere by dividing the atmosphere in layers with uniform properties (see Fig. 2.1a and b). The total AMF is then computed from the individual layer AMFs as

$$AMF = \frac{\sum_{k=1}^{n_z} AMF_k VCD_k}{\sum_{k=1}^{n_z} VCD_k}, \tag{2.4}$$

with AMF_k and VCD_k being the AMF and VCD in the k-th layer, respectively. The total AMF is thus not only a function of the atmospheric properties in each layer but also of the shape of the vertical profile of the trace gas (Palmer et al., 2001).

Alternatively, the atmosphere can be divided in boxes in all three dimensions (i, j, k) with homogeneous optical properties within each box (see Fig. 2.1c and d). Therewith, the total AMF accounts for the 3D distribution of the trace gas. The total AMF can be computed from the 3D-box AMFs $AMF_{i,j,k}$ as

$$AMF = \frac{\sum_{i=1}^{n_x} \sum_{j=1}^{n_y} \sum_{k=1}^{n_z} AMF_{i,j,k} VCD_{i,j,k}}{\sum_{k=1}^{n_z} VCD_k}, \tag{2.5}$$

where the denominator is a sum over VCDs in k different vertical layers that could, for example, be taken at the location of an instrument or above the ground pixel of an aircraft- or space-based instrument. In this case, the AMF can be interpreted as the instrument sensitivity to the trace gas under investigation for measuring that specific VCD.

2.3 Radiative transfer models

Atmospheric RTMs compute the radiative transfer of electromagnetic (EM) radiation through the atmosphere. EM radiation can originate from the sun, stars, the atmosphere, the Earth surface, synthetic light (e.g., lasers), and from other sources. In passive remote sensing, the sun is usually used as a light source. RT solvers use diverse methods to solve the integro-differential radiative transfer equation. For 1D radiative transfer models, a technique commonly applied is the so-called discrete ordinate technique where a system of linear differential equations is obtained after a Fourier and Legendre decomposition of the equation terms and by approximating the integral over all angles by a sum over discrete angles. Another computationally more expensive, but popular method is the Monte Carlo technique, which is particularly well suited for 3D radiative transfer modelling, as it calculates 3D paths of individual photons affected by atmospheric and ground scattering, and absorption properties. A Monte Carlo based RTM traces individual photons from the source (e.g., sun) to the instrument (e.g., airborne spectrometer) accounting for ground and atmospheric interactions. Photon paths are treated as a combination of random decisions with a given probability distribution for each interaction (e.g., probability distribution of the scattering direction). By tracing several thousands of photons, the averaged photon paths reaching the instrument become representative of the actual photon paths in the atmosphere (Mayer, 2009).

In this study we use MYSTIC, which is operated as one of about ten different radiative transfer equation solvers of the libRadtran package (Mayer and Kylling, 2005; Emde et al., 2016). The MYSTIC RT solver is based on the Monte Carlo principle to calculate different radiative quantities such as irradiance, radiance, absorption, emission, actinic flux, photon's path length and air mass factors (Mayer, 2009; Emde and Mayer, 2007; Schwaerzel et al., 2020). MYSTIC divides the atmosphere into 1D vertical layers or 3D grid boxes with homogeneous optical properties and saves the mean photon path length within each layer or box.

Here, I summarize MYSTIC's main steps to retrieve AMFs. The MYSTIC Monte Carlo code is extensively described in Mayer (2009). First, the (solar) photon starts at a random location on the TOA with the given solar zenith and azimuth angle. Second, the photon is assigned a random optical thickness to travel defined by a random number combined with the integrated atmosphere optical thicknesses on the theoretical direct path. Then the trajectory to the next interaction point is calculated combining the photon direction, its optical thickness to travel, and the optical thickness(es) of the air on the travel path. At the interaction point the photon will undergo a scattering or absorption event, which again is determined combining a random number and the probability of being scattered or absorbed (i.e., single scattering albedo), which depends on air composition of the grid cell. If the photon is scattered, a new photon direction will be calculated by combining a random number and a scattering phase function of the scattering object (e.g., atmospheric molecule, water droplet, ice crystal, or aerosol particle). Again the scattering object is determined combining a random number and the particles present in the grid box, where the scattering happens and the required specific phase function is read in from libRadtran. If the particle is absorbed, the tracing theoretically ends, but for computational efficiency and accuracy, the photon is forced to be scattered but the photon weight is reduced. The photon weight can be interpreted as its probability of continuing its path in the atmosphere. After the scattering process, the photon gets assigned a new random optical thickness to travel and is combined with the new direction. The steps described previously are repeated until the photon is captured by the instrument, leaves the model domain or hits the ground. Photons leaving the modelling domain through the side will reenter from the same location on the opposite boundary. Theoretically, the photon could also (very likely) leave the atmosphere at the TOA and its contribution to the AMF calculation would be null, but this is avoided by a backward mode, which is explained in the next paragraph. If the photon hits the surface between two interactions, it can be absorbed or scattered, which is defined combining a new random number with the reflectance of the surface. If the photon is reflected, MYSTIC applies a Lambertian reflection and the new direction is given by a random number. If the photon is absorbed, it will be forced to be reflected but its weight will be reduced, similarly to the atmospheric absorption described previously. Every time the photon crosses a grid box (or a layer in 1D simulation), the path length of the photon in the box is multiplied by its weight and stored. After tracing several thousands of photons, the photon path in each box is divided by the amount of simulated photons, which results in the mean photon path for each box. When divided by the height of the box, the result is a box AMF. Again, photons that are not collected by the instrument (i.e., leave the atmosphere at the TOA) would be theoretically ignored in the mean photon path calculation, but, as mentioned, the photons are traced backwards to avoid this issue.

To simulate RT quantities such as 3D-box AMFs, MYSTIC traces photons backwards from the instrument to the sun, which is equivalent to the forward mode but greatly enhances computational efficiency (Marchuk et al., 1980; Emde and Mayer, 2007). This technique is limited by the low probability of photons leaving the TOA in the direction of the sun, but MYSTIC therefore uses a directional estimate technique. A plane parallel geometry is used for 3D AMF calculations, while both plane parallel and spherical geometry is possible for 1D calculations. An example of a MYSTIC input file is shown in Appendix A. The implementation of 1D-layer and 3D-box AMFs will be described in more details in chapter 3.

3 Three-dimensional radiative transfer effects on airborne and ground-based trace gas remote sensing

This chapter was adapted from a publication[1] in the Atmospheric Measurement Technique peer-reviewed journal (Schwaerzel et al., 2020). I implemented the 3D-box AMF module in the MYSTIC solver and validated the implementation, designed and simulated the 3D scenarios, and wrote the paper. I had important inputs from Claudia Emde for the implementation of the MYSTIC module and from Gerrit Kuhlmann for the study design and setting up the manuscript. All coauthors contributed to revise the manuscript.

[1]Schwaerzel, M., Emde, C., Brunner, D., Morales, R., Wagner, T., Berne, A., Buchmann, B., and Kuhlmann, G. (2020). Three-dimensional radiative transfer effects on airborne and ground-based trace gas remote sensing. Atmospheric Measurement Techniques, 13(8):4277–4293.

Abstract: Air mass factors (AMFs) are used in passive trace gas remote sensing for converting slant column densities (SCDs) to vertical column densities (VCDs). AMFs are traditionally computed with 1D radiative transfer models assuming horizontally homogeneous conditions. However, when observations are made with high spatial resolution in a heterogeneous atmosphere or above a heterogeneous surface, 3D effects may not be negligible. To study the importance of 3D effects on AMFs for different types of trace gas remote sensing, we implemented 1D-layer and 3D-box AMFs into the MYSTIC RT solver. The 3D-box AMF implementation is fully consistent with 1D-layer AMFs under horizontally homogeneous conditions and agrees very well (<5 % relative error) with 1D-layer AMFs computed by other RTMs for a wide range of scenarios. The 3D-box AMFs make it possible to visualize the 3D spatial distribution of the sensitivity of a trace gas observation, which we demonstrate with two examples. First, we computed 3D-box AMFs for ground-based multi-axis spectrometer (MAX-DOAS) observations for different viewing geometry and aerosol scenarios. The results illustrate how the sensitivity reduces with distance from the instrument and that a non-negligible part of the signal originates from outside the line of sight. Such information is invaluable for interpreting MAX-DOAS observations in heterogeneous environments such as urban areas. Second, 3D-box AMFs were used to generate synthetic nitrogen dioxide (NO_2) SCDs for an airborne imaging spectrometer observing the NO_2 plume emitted from a tall stack. The plume was imaged under different solar zenith angles and solar azimuth angles. To demonstrate the limitations of classical 1D-layer AMFs, VCDs were then computed assuming horizontal homogeneity. As a result, the imaged NO_2 plume was shifted in space, which led to a strong underestimation of the total VCDs in the plume maximum and an underestimation of the integrated line densities that can be used for estimating emissions from NO_2 images. The two examples demonstrate the importance of 3D effects for several types of ground-based and airborne remote sensing when the atmosphere cannot be assumed to be horizontally homogeneous, which is typically the case in the vicinity of emission sources or in cities.

3.1 Introduction

Ground-based, space-based and airborne remote sensing of air pollutants and greenhouse gases from scattered sunlight are increasingly used for air pollutant monitoring (e.g., Frankenberg et al., 2005; Richter et al., 2004; McPeters et al., 2015; Burrows et al., 1999; Zhou et al., 2012; Nowlan et al., 2016) and for source detection and emission estimation (e.g., Mijling et al., 2013; Martin et al., 2003; Russell et al., 2012; Krueger et al., 1995). To retrieve NO_2 concentration from their spectroscopy measurements, those studies usually apply the DOAS technique, a commonly applied trace gas retrieval method, presented in more details in Chap. 2. From the obtained SCDs, they compute VCDs, using 1D-layer AMFs (see details in Chap. 1 and 2). The traditional 1D-layer AMFs assume horizontal homogeneity, which is not valid when the parameters affecting scattering and absorption along the path of the photons vary also horizontally, for example, in limb geometry near the polar vortex (Puķīte et al., 2010) or in the presence of clouds (Mayer and Kylling, 2005). Horizontal homogeneity is usually a valid assumption in coarse-resolution trace gas remote sensing from satellites, where small-scale horizontal variability is averaged over a large pixel size. It is, however, often not valid for ground-based or airborne trace gas remote sensing at high resolution in polluted environments such as cities, as evoked in the Introduction (e.g., Hendrick et al., 2014; Popp et al., 2012; Schönhardt et al., 2015; Tack et al., 2017). This is particularly true for nitrogen dioxide (NO_2), which has high spatial and temporal variability due to its short lifetime (Schaub et al., 2007). Other parameters affecting the path of the measured photons like surface reflectance and aerosol distributions may also have high spatial variability in cities.

To account for horizontal inhomogeneity, one-dimensional (1D) layer AMFs need to be extended to three-dimensional (3D) box AMFs. Notice that in previous studies (e.g., Rozanov and Rozanov, 2010) 1D-layer AMF were sometimes referred to as box AMFs. In this study, we will use the terms 1D-layer and 3D-box AMFs to clearly distinguish between them. The 3D-box AMFs can be implemented most easily in radiative transfer models that compute the paths of many photons using a Monte Carlo approach to solve the radiative transfer equation (Deutschmann et al., 2011). In this study, we present both the 1D-layer and 3D-box AMFs modules implemented in the MYSTIC solver of the libRadtran RTM (Mayer and Kylling, 2005; Emde et al., 2016). The implementation was evaluated against the results of a RTM comparison study (Wagner et al., 2007). Finally, the advantage and necessity of using 3D-box AMFs is demonstrated for a range of realistic ground-based and airborne remote sensing scenarios

3.2 Methods

3.2.1 Implementation of AMFs in MYSTIC

The libRadtran RTM (available at www.libradtran.org) can be used to calculate basic radiative quantities with different numerical solvers (Mayer and Kylling, 2005; Emde et al., 2016). One of its solvers is MYSTIC, which uses the Monte Carlo technique to trace individual photons on their way from the source (e.g. sun) to the target (e.g. measurement instrument). MYSTIC is extensively described in Chap. 2. The 1D-layer and 3D-box AMFs were implemented following the same methodology as in McArtim, which to our knowledge is the only other existing RTM capable of computing 3D-box AMFs (Deutschmann et al., 2011; Richter et al., 2013). Note that McArtim is no longer actively developed.

AMFs depend on absorption and scattering processes affecting the light path in the atmosphere. AMFs can be readily calculated from the photon paths simulated by a Monte Carlo radiative transfer model. The Monte Carlo technique traces the paths of individual photons by describing the effects of absorption, scattering and reflection as random events with specific probabilities (Mayer, 2009) (also see details in Chap. 2). To obtain a robust measure of the mean optical path, a large number of photon paths need to be traced.

SCDs, VCDs and AMFs can be computed for the whole atmosphere, for individual vertical layers, or for individual 3D boxes. For the general case of an atmospheric box i with constant concentration and optical properties, the AMF can be written as:

$$AMF_i = \frac{SCD_i}{VCD_i} = \frac{\int_{path} c_i dl}{\int_{z_i}^{z_{i+1}} c_i dz} = \frac{\int_{path} dl}{h_i} = \frac{L_i}{h_i}, \tag{3.1}$$

where $L_i = \int_{path} dl$ is the mean optical path within the box of all photons that reach the instrument and h_i is the height of the box. Since the 3D-box/1D-layer AMFs are usually simulated for a sensor at a specific location in a three-dimensional model-domain, the photons are traced backwards from the sensor towards the sun to increase computational efficiency as described in Marchuk et al. (1980) and Emde and Mayer (2007) (also see Chap. 2). In addition, the commonly used variance reduction method, known as "local estimate", is applied at each scattering event (Marshak and Davis, 2005). The method computes the probability of an individual photon to be scattered into the direction of the sun that is assigned as a weight w_n to the photon. The weights of all photons can be summed up to obtain the radiance at the sensor. When a photon is scattered, a weighted photon path-length ($w_n \cdot l_i$) is also calculated, where l_i are the path-lengths in each individual box i traversed by the photon before the scattering event. The mean optical path within a box i is then obtained by summing up the weighted photon path-lengths of all photons:

$$L_i = \frac{\sum_n^N w_n l_{i,n}}{\sum_n^N w_n}, \tag{3.2}$$

where N is the total number of photons. L_i is then divided by the height of the box/layer to obtain the 3D-box/1D-layer AMF.

3.3 Validation of the AMF modules

3.3.1 Evaluation scenarios

The implementation of the 1D-layer and 3D-box AMF module in MYSTIC was evaluated against the results of different RTMs presented in an extensive RTM comparison study (Wagner et al., 2007). The simulated scenarios are representative for ground-based Multi-Axis-DOAS (MAX-DOAS) measurements of scattered sunlight spectra for different elevation angles (see Fig. 2.1b and d for the case of zenith-sky observations). The nine models included four models using full spherical geometry, four models using spherical geometry only for a subset of interactions and one model using plane-parallel geometry. The 1D-layer AMFs computed by these models agreed very well with differences mostly below 5 %, which could mainly be attributed to the different treatments and approximations of the Earth's sphericity and to model initialization parameters (Wagner et al., 2007).

For the comparison, we computed 1D-layer and 3D-box AMFs with MYSTIC in plane-parallel geometry as well as 1D-layer AMFs in spherical geometry for all scenarios presented in Wagner et al. (2007). 3D-box AMFs have not yet been implemented with spherical geometry.

1D-layer and 3D-box AMFs were computed for five wavelengths (310 nm, 360 nm, 440 nm, 477 nm, 577 nm), seven elevation angles (1°, 2°, 3°, 6°, 10°, 20°, 90°), and three aerosol scenarios (aerosol extinction of 0.0, 0.1 and 0.5 km^{-1}). For the aerosol scenarios, an aerosol layer was prescribed between 0 and 2 km with an asymmetry parameter of 0.68 and a single scattering albedo of 1.0. No aerosols were prescribed above 2 km. For the simulations 17 vertical layers were used with a thickness of 100 m below 1000 m and a thickness of mostly 1000 m above (see Table 1 in Wagner et al., 2007). Profiles of temperature, pressure, density and ozone concentration were taken from the US standard atmosphere (United States Committee on Extension to the Standard Atmosphere, 1976). Ozone cross sections (in cm^2) were 9.59×10^{-20}, 6.19×10^{-23}, 1.36×10^{-22}, 5.60×10^{-22} and 4.87×10^{-21} at 310 nm, 360 nm, 440 nm, 477 nm and 577 nm, respectively. Other atmospheric absorbers were ignored. Further details can be found in Wagner et al. (2007). For each scenario, we traced 1 million photons, which balances statistical noise expected from a Monte Carlo approach with computation time. The computed 3D-box AMFs were integrated horizontally to obtain 1D-layer AMF that can be compared with the 1D-layer AMFs from other models. MYSTIC was mainly compared to SCIATRAN (Version 2.2, Rozanov et al. (2005)). SCIATRAN was chosen because it agrees well with the mean of the models in Wagner et al. (2007), and also because it is based on the discrete ordinate method to solve the radiative transfer equation, which is fundamentally different from a Monte Carlo solver, and finally because it offers both plane-parallel and spherical solutions. In addition, we compared MYSTIC to the mean of eight of nine RTMs in the comparison study. The PROMSAR/Italy model was not included because of its large deviation from the mean (see Wagner et al., 2007, for details).

3.3.2 Validation results

The comparison of 1D-layer AMF profiles calculated with the MYSTIC 1D modules with SCIATRAN for the 67 observation scenarios used in Wagner et al. (2007) is summarized in Fig. 3.1 in the form of a scatter plot. The horizontally integrated AMFs from MYSTIC's 3D module perfectly agree with its 1D module with plane-parallel geometry within the statistical noise of the Monte Carlo approach. When tracing 1 million photons, the difference between 1D and 3D module was smaller than 0.5 %. Therefore, only results from the 1D module were plotted against the SCIATRAN results. The agreement between MYSTIC and SCIATRAN is very good for almost all scenarios with relative differences mostly below 5 %. 97 % of the compared points are within a relative difference of 5 % for spherical geometry and 92 % for plane-parallel geometry. The mean of the relative differences for spherical geometry is 0.9 % and its standard deviation 2.0 % and for the plane-parallel geometry the mean is 0.3 % with a standard deviation of 2.7 %.

To illustrate the differences in AMF profiles between the two RTMs, we selected four scenarios with a wavelength of 577 nm, because at this wavelength we observe comparatively large differences between the two models. To illustrate a usual scenario with low difference, we also selected the same scenarios but with a 360 nm wavelength. The upper row of Fig. 3.2

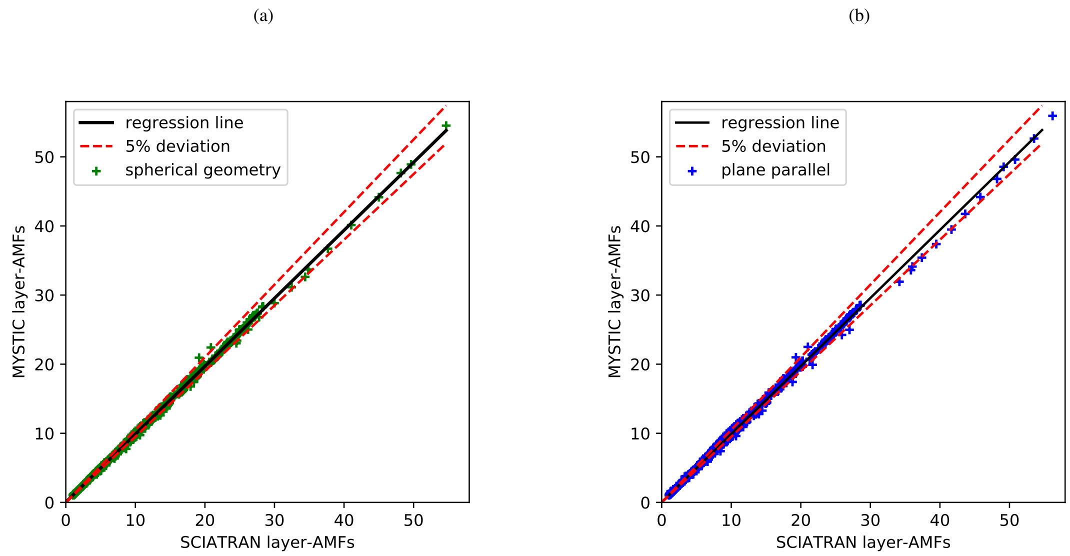

Figure 3.1 – Scatter plots of MYSTIC 1D-layer AMFs computed with spherical (a) and plane-parallel geometries (b) against 1D-layer AMFs computed with SCIATRAN spherical (a) and plane-parallel (b) for 67 MAX-DOAS scenarios with 17 layers (1139 points). The solid black lines are the respective regression fits to the points.

(scenario at 577 nm) and Fig. 3.3 (scenario at 360 nm) shows MYSTIC 1D-layer AMF profiles for the selected scenarios with a low elevation angle of 3° and a high elevation angle of 90° (zenith) without and with aerosols, respectively. For comparison, the corresponding profiles computed with SCIATRAN are also shown. The lower row presents the relative differences between MYSTIC and SCIATRAN. Since plane-parallel and spherical modes have different geometrical assumptions, we compare plane-parallel models and spherical models separately.

In the upper atmosphere, the 1D-layer AMFs decrease with altitude in all scenarios (Figs. 3.2 and 3.3), because the atmospheric density is decreasing, which lowers the amount of scattering and, correspondingly, the mean photon path length. In the lowest layers, however, the profile shapes are different for the two elevation angles with a rapid decrease with altitude in the low elevation angle scenarios and a local maximum between 2 and 5 km in the high elevation angle scenarios. This local maximum is caused by multiple scattering, which contributes to the horizontal light paths in those layers. The reduction towards the surface in the latter scenarios is due to the low surface albedo. For an elevation angle of 3°, AMFs are high close to the ground because of the long light path in the layers due to the low elevation angle. Since aerosols increase scattering, photon path lengths and correspondingly 1D-layer AMFs are low in the lowest 2 km, when an aerosol layer is present.

1D-layer AMFs computed with spherical and plane-parallel geometry show noticeable differences for long wavelengths and low aerosol extinction, especially at altitudes above 5 km where extinction coefficients are small (see upper-and lower-left part in Fig. 3.2). In plane-

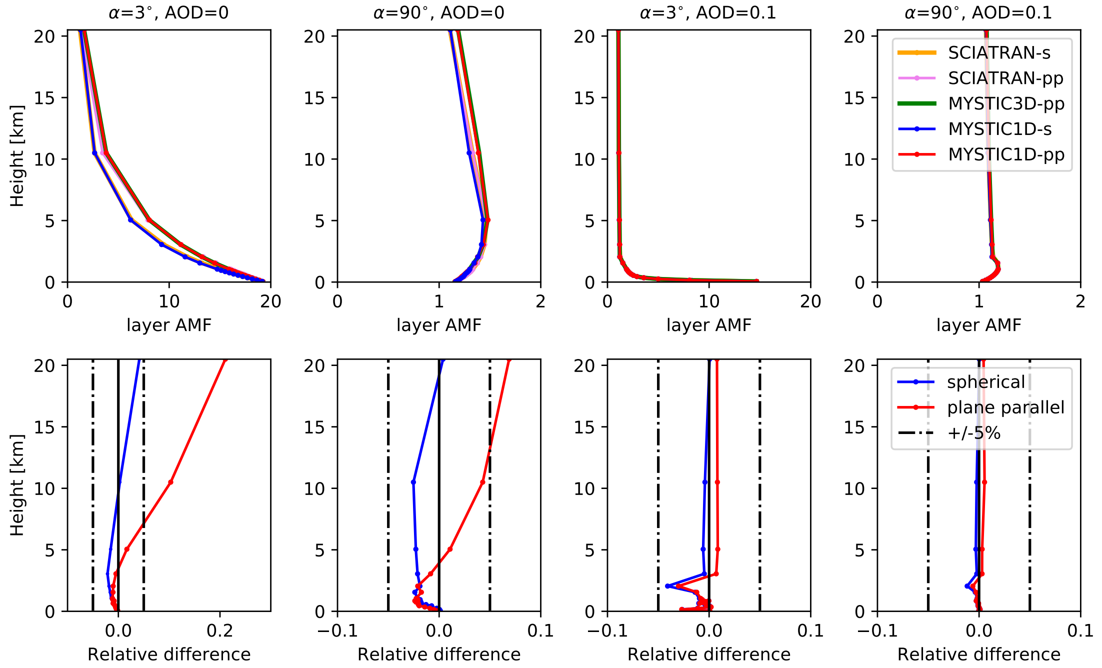

Figure 3.2 – Upper row: MAX-DOAS AMF profiles for MYSTIC 1D spherical geometry (s), 1D plane-parallel geometry (pp) and 3D plane-parallel geometry (pp) for two selected elevation angles of 3° and 90°, a SZA of 20°, with and without aerosol for radiation at 577 nm. Corresponding profiles computed with the SCIATRAN RTM are shown for comparison. Lower row: Profile of relative differences of MYSTIC and SCIATRAN results in spherical (s) and plane-parallel geometry (pp) (Wagner et al., 2007).

parallel geometry, if one of these photons is traveling horizontally, it will strongly contribute to increase the mean photon path in that specific layer. In spherical mode, the same photon would change layer because of the curved atmospheric layers, and therefore its contribution to the mean photon path will be divided between the crossed layers. Furthermore, in a curved atmosphere, the zenith angle of the photon, which was initially traveling horizontally, will increase. At low altitude, these effects are smaller, and, conversely, 1D-layer AMFs computed with spherical and plane-parallel geometry agree better (mostly < 5 %).

AMF profiles calculated with MYSTIC generally agree very well with those calculated with SCIATRAN with relative differences mostly smaller than 5 %. However, significant differences (up to 23 % relative difference) are seen between the plane-parallel solutions of the two models above 5 km for the scenarios without aerosols at 577 nm (Fig. 3.2). In contrast to the plane-parallel case, the spherical solution of MYSTIC is in good agreement with the spherical solution of SCIATRAN. The difference between SCIATRAN plane-parallel and MYSTIC plane-parallel is attributed to the different solution methods of the radiative transfer equation. A possible explanation is the following: in discrete ordinate methods, the directions of the radiation field are discretized and do not include the exact horizontal direction, for which in plane-parallel geometry the photon path-length becomes extremely large in an optically thin medium like

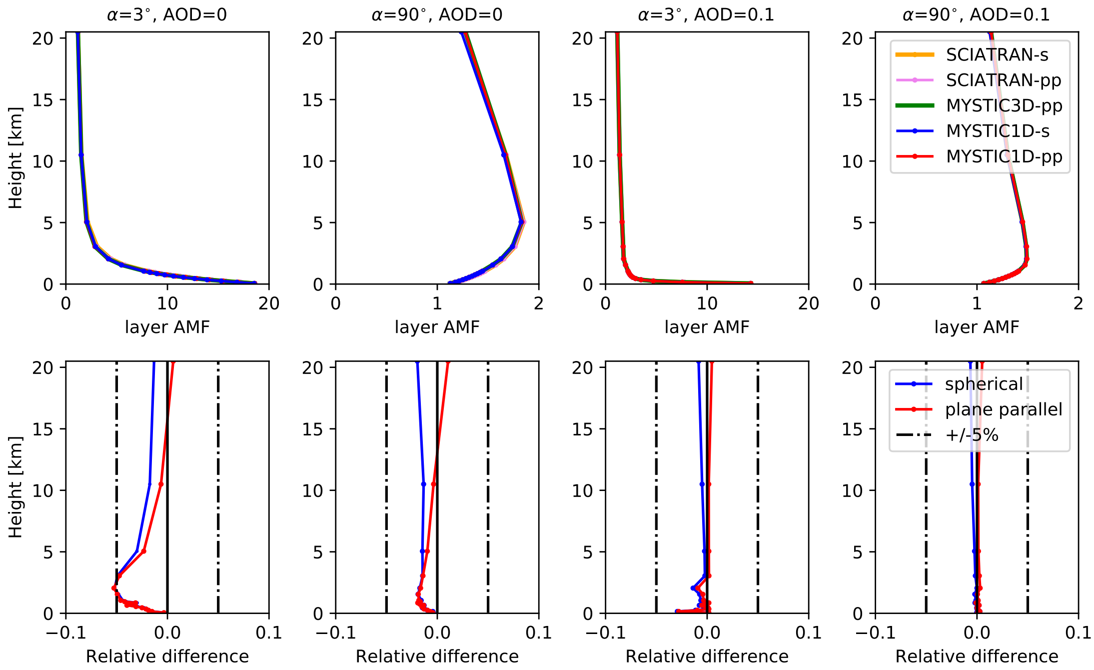

Figure 3.3 – Upper row: MAX-DOAS AMF profiles for MYSTIC 1D spherical geometry (s), 1D plane-parallel geometry (pp) and 3D plane-parallel geometry (pp) for two selected elevation angles of 3° and 90°, a SZA of 20°, with and without aerosol for radiation at 360 nm. Corresponding profiles computed with the SCIATRAN RTM are shown for comparison. Lower row: Profile of relative differences of MYSTIC and SCIATRAN results in spherical (s) and plane-parallel geometry (pp) (Wagner et al., 2007).

the higher atmosphere. In a Monte Carlo model, this horizontal direction is included, therefore the 1D-layer AMF might be larger. This hypothesis could be tested by including more streams (discrete directions) in SCIATRAN and verifying if the solution approaches the higher AMFs from the MYSTIC solution.

The simulations for the same scenarios but with 360 nm wavelength agree very well with SCIATRAN for both spherical and plane-parallel geometries (relative difference <5 %). The differences mentioned above are much smaller at this wavelength because atmospheric scattering events increase with lower wavelength and thus, prevent those very long photon paths. We also investigated a scenario with a wavelength of 440 nm, which is a typical wavelength of the window used for NO_2 fitting (see Fig. B4 in Appendix B.1), for which MYSTIC and SCIATRAN also agree very well (< 5 % relative difference), but as for simulations at 577 nm discussed above, the simulations at 440 nm show significant differences between plane-parallel and spherical geometry for layers above 5 km. These differences are, however, smaller than at 577 nm, because the optical thickness of Rayleigh scattering is higher at 440 nm.

Overall, MYSTIC agrees very well with SCIATRAN with differences mainly smaller than 5 %. An exception is the high elevation scenario without aerosols, where the plane-parallel solutions of MYSTIC and SCIATRAN differ by up to 23 % for a wavelength of 577 nm at altitudes above 5 km. It should be noted that for these cases the 1D-layer AMFs are very small and therefore the absolute differences, which are relevant for most applications, are also small. 1D-layer AMFs computed with MYSTIC also agree very well with the other models presented in Wagner et al. (2007). Differences larger than 5 % are mainly attributable to differences between plane-parallel and spherical solutions (see Appendix B.1). When comparing MYSTIC with the mean of the models, 88.3 % of the compared points are within a relative difference of 5 % for spherical geometry, 81.5 % for plane-parallel geometry, and 97.5 % for the mean of plane-parallel and spherical geometry. The mean of spherical and plane-parallel geometry agrees best because the models in Wagner et al. (2007) represents a mixture of spherical and plane-parallel solutions.

3.4 3D-box AMFs for MAX-DOAS observations

MAX-DOAS is a ground-based passive remote sensing technique allowing to retrieve vertical concentration profiles of trace gases and aerosols (Wagner et al., 2004; Frieß et al., 2006; Irie et al., 2011; Hönninger and Platt, 2002). Information about the vertical distribution is obtained by measuring spectra at a prescribed sequence of elevation angles. Observations at different elevation angles have different sensitivity to the concentration in a given vertical layer. 3D-box AMFs as computed by MYSTIC are particularly suitable to illustrate this, because 3D-box AMFs are a direct representation of the spatial distribution of the sensitivity of the measurements.

To illustrate the 3D distribution of 3D-box AMFs for a typical MAX-DOAS measurement, we simulated 3D-box AMFs at 450 nm for two scenarios with low and high aerosol optical depth, which correspond to a visibility of 50 and 10 km in the planetary boundary layer (PBL), respectively. 450 nm is a typical wavelength for light absorption by NO_2. The instrument points northwards with an azimuth angle of 180° and an elevation angle of 5°. The solar azimuth angle is 344.7° (164.7° relative azimuth angle) and the solar zenith angle is 24.6°. The MYSTIC input file is provided in Appendix B.1.

Figures 3.4a and 3.4b show the 3D-box AMFs in the plane of the line of sight of the instrument for the two scenarios. In both cases, 3D-box AMFs are highest along the line of sight and reduce with distance from the instrument. Most of the photons collected by the instrument experienced a single scattering into the line of sight of the instrument. With increased aerosol amount (visibility of 10 km), photons scattered into the line of sight far away from the instrument have a high chance of being scattered out again. As a result, the sensitivity rapidly (within a few kilometers) decreases along the line of sight with increasing distance from the instrument. Multiple scattering becomes more important in this scenario, which explains the enhanced sensitivity to layers below and above the line of sight within a distance of up to 4 km of the instrument. The decrease in AMF with distance is further illustrated for the two scenarios in Fig. 3.4c which shows the vertically integrated AMFs (in the aerosol layer) as a function of distance y to the instrument normalized with AMFs integrated horizontally in y

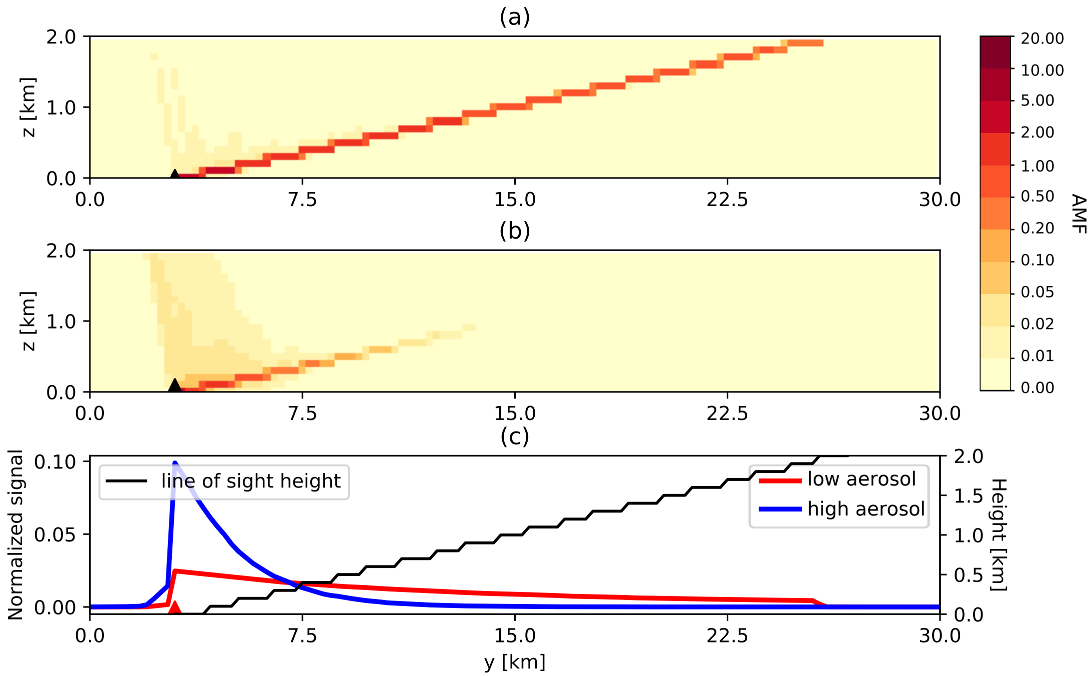

Figure 3.4 – Cross section of 3D-box AMFs for a MAX-DOAS scenario with an instrument (black triangle) at the ground (z=0 km, x=20 km, y=3 km) pointing northwards and slightly upwards at a viewing angle of 5°. The sun is at an azimuth angle of 344.7° and a zenith angle of 24.6°. The relative azimuth angle between sun and viewing direction is 164.7°. AMFs were simulated with two aerosol scenarios: a rural type aerosol representative of spring-summer conditions in the aerosol layer (0-2 km), with a visibility of 50 km (a) and a visibility of 10 km (b) and a background aerosol above 2 km. Decay of vertically integrated AMFs with distance to the instrument is visualized (c) for the same scenarios with standard (red) and high aerosols (blue) as in (a) and (b). The altitude of the line of sight as a function of distance is shown in black.

direction. The figure also shows the height of the main optical path as a function of y.

To illustrate the horizontal spread of the sensitivity of the MAX-DOAS measurements in the PBL, Fig. 3.5 shows horizontal distributions of vertically integrated 3D-box AMFs (0-2 km) for the same scenarios with low (top row) and high (bottom row) aerosols and for five different sun positions corresponding to different times of the day on 21 July in the city of Zurich. The horizontal distribution of AMFs shows high values not only along the line of sight of the instrument but also in a surrounding region, which is up to a few kilometers wide. This region is wider for larger relative azimuth angles and is inclined towards the direction of the sun. The simulations show not only that the MAX-DOAS measurements are sensitive to NO_2 along the line of sight but also that they are also influenced by neighboring regions a few kilometers away.

For the different scenarios, we evaluated which part of the signal originated from a 0.25 km wide region centered on the northward pointing line of sight (referred to as main line in the

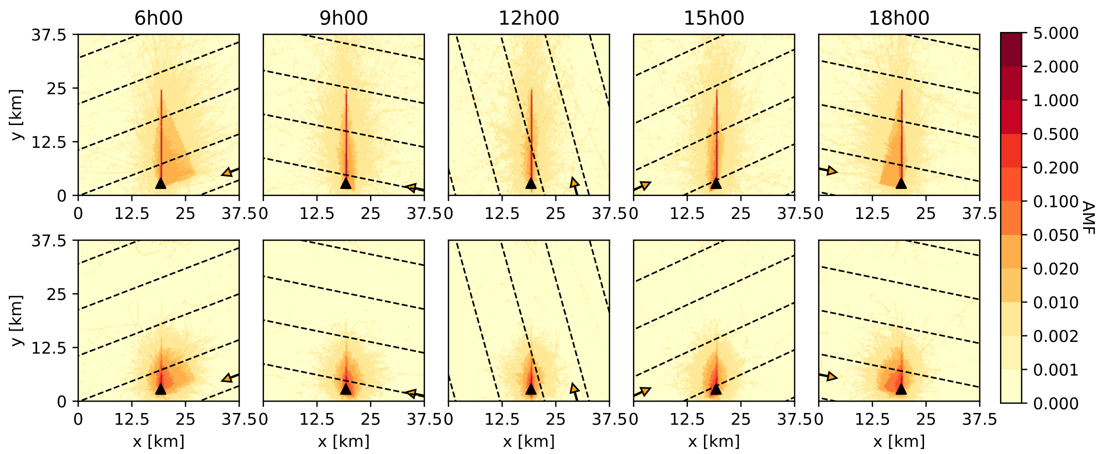

Figure 3.5 – Top: vertically integrated 3D-box AMFs in the PBL (z < 2.0 km) for an instrument at the ground pointing northwards with an instrument zenith angle of 5° for different times of the day on the 21st of June in Zurich. Solar zenith angles are 77.4°, 47.5°, 24.6°, 38.6° and 68.5° and solar azimuth angles are 249.0°, 281.5°, 344.7°, 65.2° and 101.7°. The arrows point away from the sun and the dashed lines show the direction of photons coming from the sun. AMFs were simulated with a rural-type aerosol representative of spring-summer conditions in the aerosol layer (0-2 km) with a visibility of 50 km and a background aerosol above 2 km. Bottom: same as above but for a scenario with increased aerosol (visibility of 10 km).

following) and which part crossed boxes outside this range. For the low-aerosol scenario, between 63 % and 70 % originated from the main line. Thus, up to 37 % of the signal originated from photons crossing neighboring boxes. For the high-aerosol scenario with enhanced scattering, the part of the signal originating from the main line was correspondingly lower, between 30 % and 41 %. The lower values correspond to the scenarios with higher relative azimuth angles.

Depending on the viewing direction of the instrument relative to the position of nearby emission sources, this temporally varying spatial sensitivity could introduce a diurnal cycle in the measurement even when the trace gas concentration field was constant in time. Understanding the horizontal distribution of the sensitivity to NO_2 and its variation in time is thus particularly important for the interpretation of MAX-DOAS observations in polluted regions like cities with strong NO_2 gradients, for which 3D-box AMFs can be a valuable tool.

3.5 3D-box AMFs for airborne observations

In this section, we demonstrate the effect of the spatial variability in 3D-box AMFs on airborne NO_2 imaging spectroscopy. For this purpose, we simulated a NO_2 plume emitted from a stack to generate a scenario with a distinct three-dimensional trace gas structure. An airborne spectrometer was then assumed to fly parallel to the plume axis and to sample the plume in the across-track direction (see dashed line in Figure 3.7). We illustrate the distinct 3D-

Table 3.1 – MYSTIC input parameters for the emission stack scenario.

Parameter	Value
Wavelength [nm]	460
Solar zenith angle [°]	0, 40, 20, 60
Solar azimuth angle [°]	90, 0, 180, 270
Viewing zenith angle [°]	0 to 26.6
Viewing azimuth angle [°]	90 / 270
Surface albedo	0.2
Aircraft position x [km]	2.9
Aircraft position y [km]	0-4
Aircraft position z [km]	6
Domain size [boxes]	40×40×47
Horizontal resolution [m]	100.0
Vertical resolution (0 - 7km) [m]	25

structure of the sensitivity of the measurements to NO_2 (as represented by the 3D-box AMFs) and demonstrate the limitations of using 1D-layer AMFs for such observations.

3.5.1 Synthetic observations of a NO_2 stack emission plume

The NO_2 plume was computed with the Graz Lagrangian dispersion Model (GRAL) (Oettl, 2015) for a 262.5 m tall stack located at x=1.9 km and y=1.3 km. NO_2 molecules were released at this altitude at a constant rate of 40 kg h^{-1}. NO_x chemistry was ignored for simplicity. The model domain had a size of 4 km × 4 km and extended from the surface to 21 km altitude. The simulated NO_2 was sampled on an output grid with a 100 m horizontal resolution and 20 vertical levels with 25 m resolution from 0 to 500 m. For the simulation we assumed neutral atmospheric stability and southerly wind with a speed of 5 m s^{-1} at 12 m above ground. The full vertical wind profile is generated within the model based on similarity theory. The NO_2 background from the US Standard Atmosphere (United States Committee on Extension to the Standard Atmosphere, 1976) was added to the simulated NO_2 field, that was extended to 21 km altitude (see vertical resolution profile in Appendix B.1). The resulting NO_2 VCDs are shown in Figure 3.7a. In the following, the simulated NO_2 concentration field and the corresponding NO_2 VCDs are referred to as the true NO_2 field and as the true total VCD, respectively. The true VCD will be used as a reference to demonstrate the limitations of 1D radiative transfer calculations.

Using MYSTIC, we computed the SCDs that would be observed from an airborne push-broom spectrometer flying parallel to the plume axis from south to north at an altitude of 6 km. The field of view in the across-track direction of the instrument covers the full x-direction of the model domain. The SCDs were obtained by computing 3D-box AMFs for each single observation (i.e., for each ground pixel) and multiplying these AMFs with the 3D NO_2 field from the simulation (which corresponds to the numerator in Eq. 2.5).

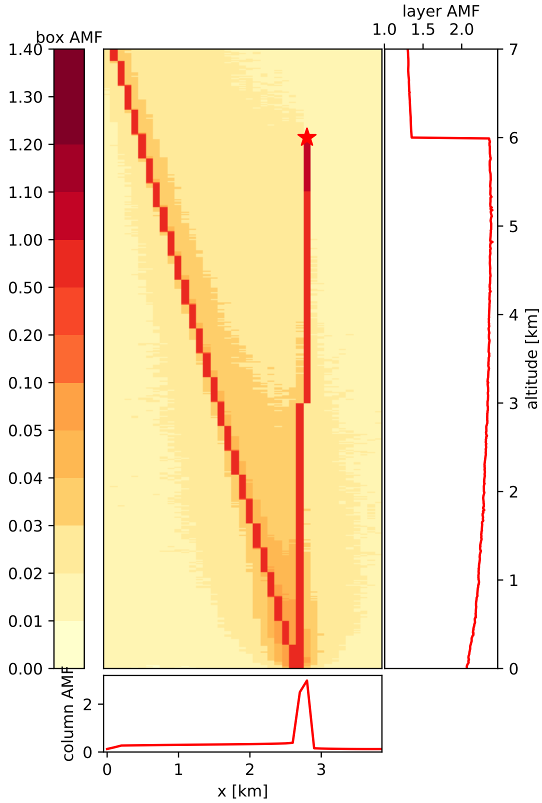

Figure 3.6 – (a) The 3D-box AMFs cross section at y=1.4 km for the aircraft scenario presented in this section. Aircraft (red star) placed at z=6 km, x=2.9 km and y=1.4 km pointing eastwards. The sun is at SAA = 90° (west) with a SZA of 20°. (b) Vertical profile of horizontally integrated AMFs (1D-layer AMFs). (c) Horizontal profile of vertically integrated AMFs (column AMFs). The default properties are a rural-type aerosol in the PBL, background aerosol above 2 km, spring-summer conditions and a visibility of 50 km.

As an example, Fig. 3.6 illustrates the 3D-box AMFs for an instrument pointing downwards at a zenith angle of 4.8° and an azimuth angle of 90°. The sun is placed in the west (SAA=90°) at a SZA of 20°, i.e., the instrument is facing the sun. The figure shows the 2D cross section of 3D-box AMFs in the principal plane of the observations, which aligns with the x-z plane in this geometry. The panels to the right and below the main figure show vertically and horizontally integrated 3D-box AMFs, i.e., column and layer AMFs, respectively. The layer AMFs are identical to 1D-layer AMFs. The 3D-box AMFs are high along the line of sight of the instrument and largest just below the aircraft. Most photons travel directly along the geometric path from the sun to the ground pixel and then to the instrument. Although 3D-box AMFs are highest along the geometric path due to the relatively bright surface, a non-negligible fraction of photons is scattered into the line of sight without reaching the surface, leading to an increase in 3D-box AMFs within a parallelogram bounded by the line of sight and the position of the sun.

The column AMFs (Fig. 3.6c) are highest close to the instrument and decrease with distance to the instrument in the x-direction due to atmospheric scattering. After the "reflection point", values continue to decrease with distance to the instrument but at a lower rate. Due to periodic boundaries this decrease continues on the right of the instrument ($x \geq 3.9$ km). Layer AMFs (i.e., 1D-layer AMFs) (right panel) are highest directly below the instrument. They change by a factor of 2 at the altitude of the aircraft because layers below are crossed (at least) twice by the photons, while layers above are only crossed once.

3D-box AMFs and corresponding SCDs were computed for four different solar zenith angles and four different relative azimuth angles between the sun and the plume axis (and flight direction). We used a default aerosol scenario with a rural-type aerosol representative for spring-summer conditions in the PBL (0-2 km) and a background aerosol above 2 km (visibility of 50 km in the PBL). The parameters used for the AMF calculation are summarized in Table 3.1. Note that with perfect knowledge of the relative NO_2 distribution, the true total VCD could be reproduced exactly from the SCDs using 3D radiative transfer calculations. The computational cost of calculating 3D-box AMFs is considerably larger than for 1D-layer AMFs. The computational time for calculating 3D-box AMFs for the scenarios here (see Table 3.1 with SZA=20°, SAA=90°, VAA=90° and VZA=2°) is around 218 s with 1 million photons using a single core of our local machine (Intel Xeon W-2175 CPU @ 2.5 GHz). The computational time for the corresponding 1D-layer AMFs is only about 4 s with 1 million photons. Note, however, that even less photons would be sufficient to obtain a similar noise level as for the 3D-box AMFs.

The SCDs computed for the scenario with the sun illuminating the scene from the west at a solar zenith angle of 40° are presented in Fig. 3.7b. The SCDs are larger than the VCDs (panel a) because the AMFs (panel c) are generally larger than 1. The SCD plume is wider and shifted towards the east compared to the VCD plume. The widening is due to both geometric effects and atmospheric scattering. Geometric effects are caused by the fact that photons following the main geometric path from the sun to the surface and to the instrument may traverse the plume either on the way from the sun to the surface or from the surface to the instrument (or both). These two pathways are separated horizontally. For high solar zenith angles (here SZA=40°) this leads to two SCD maxima close to the source as seen in Fig. 3.7b. The westerly maximum corresponds to the direct observation of the plume (photons reflected by the surface pass the plume on the direct way to the aircraft), whereas the easterly maximum corresponds to its mirror image (photons first travel through the plume before they get reflected at the surface and reflected to the aircraft). This is further illustrated in Fig. 3.8, where two of the three illustrated direct paths (i.e., three viewing zenith angles) cross the NO_2 maximum - main photon path (1) and (3) in Fig. 3.8. The main photon path for the observation angle (2) in Fig. 3.8 misses the plume maximum, which is why total SCD is lower for this observation. Atmospheric scattering leads to an additional horizontal smoothing of the plume, but in the case of a medium-high surface albedo of 0.2, the geometric effects dominate.

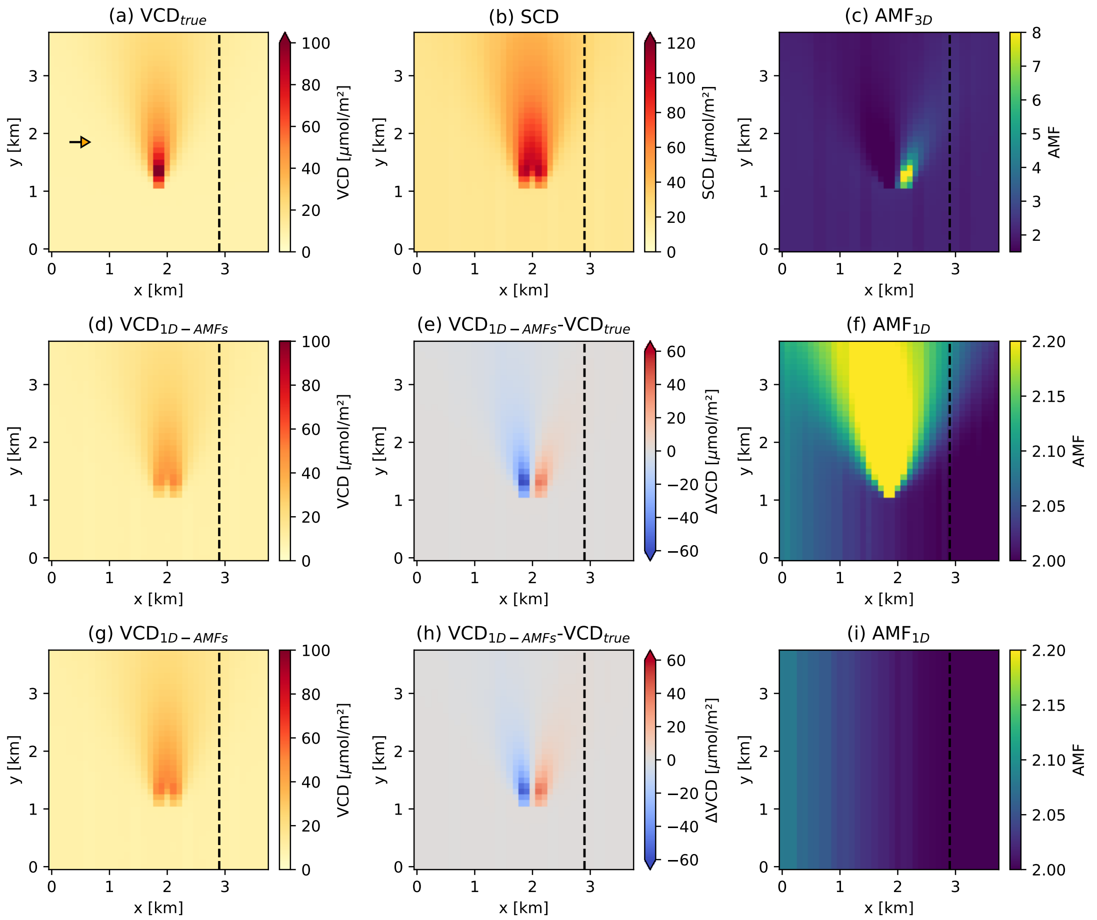

Figure 3.7 – Airborne remote sensing of an NO_2 plume emitted from a 262.5 m tall stack located at x=1.9 km and y=1.3 km. The aircraft flies at an altitude of 6 km from south to north at x = 2.9 km (dashed line) parallel to the plume axis and samples the plume in across-track direction. The sun is located in the west (small arrow in panel a) at a zenith angle of 40°. The panels show (a) simulated (true) NO_2 VCDs, (b) synthetic SCDs computed from the simulated NO_2 distribution by applying 3D-box AMFs, and (c) 3D-box AMFs computed with MYSTIC. The 2nd row shows (d) VCDs calculated from the SCDs using 1D-layer AMFs and the "true" NO_2 profile above the ground pixel pointed by the instrument, (e) the difference between calculated and true VCDs, and (f) total AMFs from the MYSTIC 1D module. The 3rd row (g)-(i) shows the same as (d)-(f) but using the background NO_2 profile to compute AMFs.

3.5.2 Limitations of VCDs calculated from 1D-layer AMFs

For each scenario, total AMFs were also computed from 1D-layer AMFs, which requires a NO_2 profile (Eq. 2.4). The most obvious approach is to use the true NO_2 profile above the ground pixel the instrument is pointing towards, which is based on the idea that the AMF is used to convert an SCD to a VCD above a ground pixel (Fig. 3.7d, e, and f). Alternatively, a NO_2 background profile from the US Standard Atmosphere (United States Committee on Extension

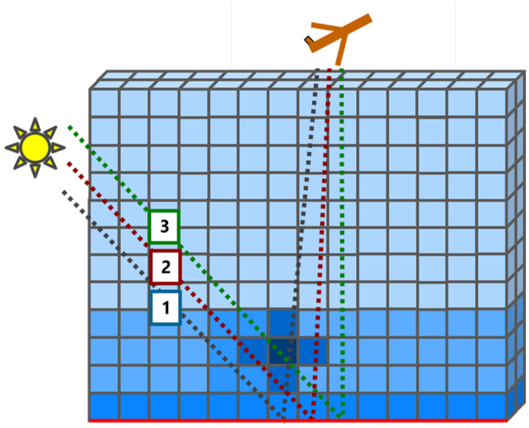

Figure 3.8 – Schematic of the across-track measurement by the aircraft measuring a NO_2 plume (dark blue corresponding to high NO_2 concentrations) with 3 main photon paths for 3 measurement geometries (1, 2, 3).

to the Standard Atmosphere, 1976) was used for each ground pixel, which assumes that no information on the spatial variability in NO_2 is available (Fig. 3.7g, h, and i).

Figure 3.7f and i show the total AMFs computed with the true and background NO_2 profile, respectively. In both cases, AMFs increase with distance from the aircraft due to the increasing viewing zenith angle. For the true NO_2 profiles, AMFs are higher inside the plume. This can be explained by the fact that the measurements are more sensitive to NO_2 inside the plume than to the background NO_2 outside because the plume is located at an altitude where the 1D-layer AMFs are higher.

Figure 3.7d and g show the VCDs obtained by dividing the true SCDs in Fig. 3.7b by the 1D-layer AMFs in Fig. 3.7f and i, respectively. Since geometric distortions and horizontal smoothing due to scattering cannot be corrected for when using a 1D radiative transfer model, all structures seen in the SCDs are essentially preserved in the VCDs including the double peak structure, the widening of the plume, and the horizontal displacement. Figures 3.7e and h show the differences of these VCDs from the true VCDs. In both cases, the location of the plume is shifted towards the aircraft relative to the true position. Within the maximum of the plume, this displacement leads to an underestimation of the true VCDs by -60.8 μmol m^{-2} when using the NO_2 profile (Fig. 3.7e) above the ground pixel and by -54.6 μmol m^{-2} when using the constant NO_2 profile (Fig. 3.7h).

The displacement of the calculated VCD plume and the magnitude of the bias depend on the position of the sun as demonstrated in Figs. 3.9 and 3.10. The shift increases with increasing SZA due to the geometric effects explained earlier. The relative azimuth angle between the viewing direction and the sun also plays a critical role. The displacement is smaller when the aircraft is flying directly away from the sun (SAA=0°) or towards the sun (SAA=180°) and the sun illuminates the scene along the plume axis, but even in these cases it is not negligible.

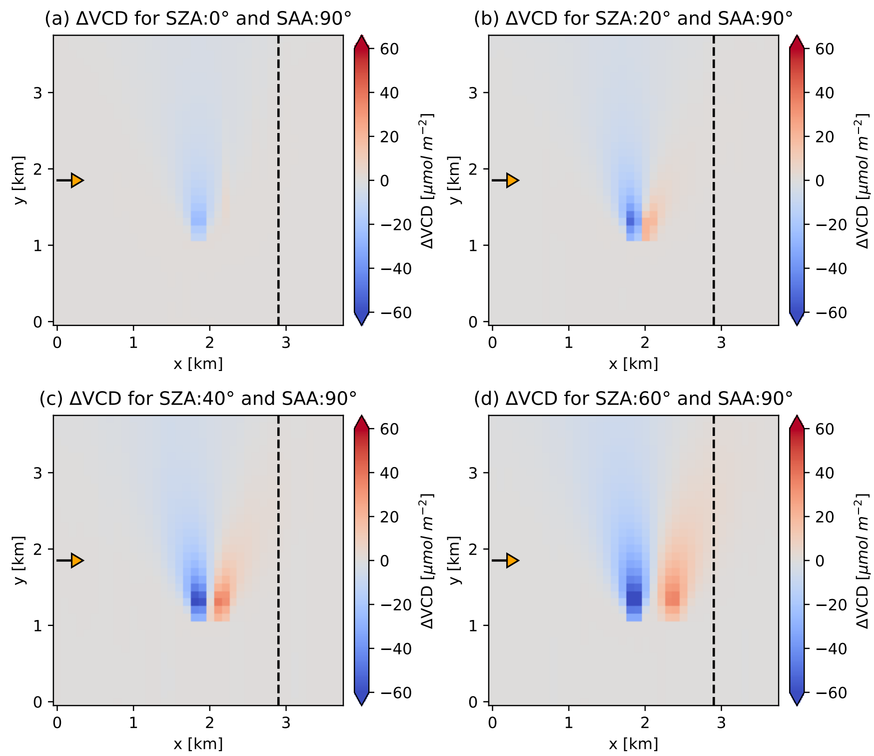

Figure 3.9 – Absolute difference between total VCD from synthetic SCD and 1D box AMF with solar zenith angles (SZA) of (a) 0° (b) 20°, (c) 40° and (d) 60° and the true total VCD.

Biases are typically larger when the spatial displacement is large.

3.5.3 Plume flux estimation

A possible application of airborne imaging spectroscopy is the estimation of NO_2 emissions from point sources. Measurements from airborne spectrometers have been used, for example, to estimate CO_2 emissions from power plants (Krings et al., 2011) or CH_4 emissions from coal mine ventilation shafts (Krings et al., 2013). The emissions can be estimated using a mass-balance approach by integrating the NO_2 VCD enhancement above the background across the plume and multiplying this integral (referred to as line density in the following) with a mean wind speed to obtain a flux. The flux is equivalent to the source strength under the assumption of steady-state conditions.

We computed line densities 300 m downstream of the source for the true VCD field and for fields computed with 1D-layer AMFs for different solar zenith and azimuth angles. The VCD cross sections are shown in Fig. 3.11. The line densities were multiplied with a wind speed of 9.1 m s^{-1}, which is the wind speed at the stack height of 262.5 m in the GRAL simulation.

Table 3.2 summarizes the computed line densities and fluxes for the different scenarios. In

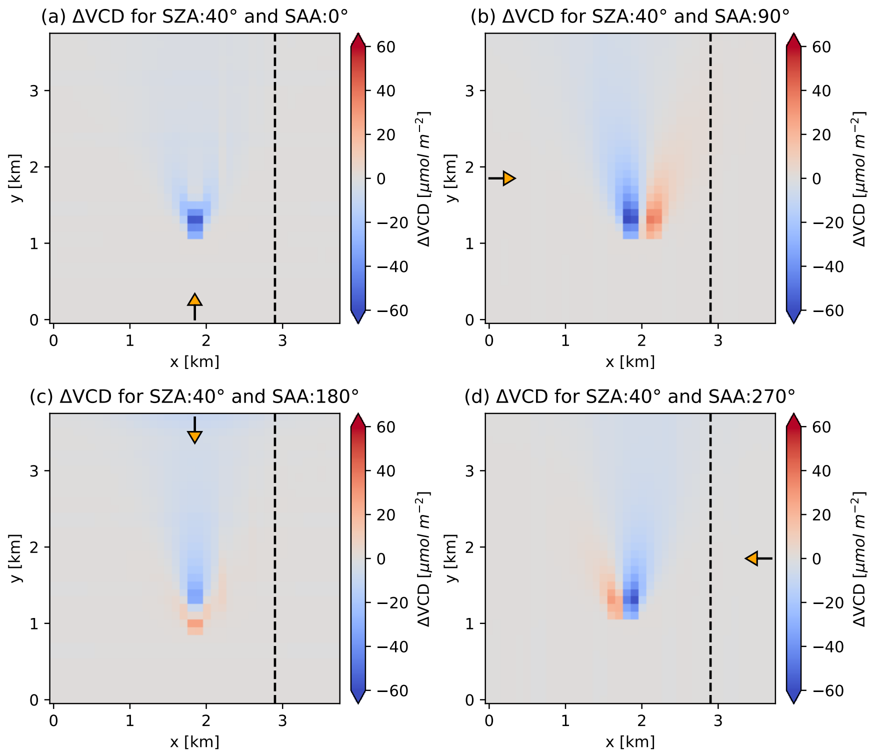

Figure 3.10 – Absolute difference between total VCD from synthetic SCD and 1D box AMF with solar azimuth angle of (a) 0°, (b) 90°, (c) 180° and (d) 270° and the true total VCD.

all scenarios, emissions were significantly underestimated by 9-37 % (relative to the true VCD) depending on the solar azimuth and zenith angle. Note that the emission estimation for the true VCD is slightly higher than the emission input for the dispersion model due to simplification of the mass balance approach, which does not account for the vertical variability in wind speeds across the plume. The bias in the plume emission estimation using 1D-layer AMFs generally increases with solar zenith angle. This bias also depends on the solar azimuth angle. The largest bias occurs, when the SAA is 0° or 180°, i.e., the instrument is flying towards and away from the sun.

3.6 Conclusions

This study demonstrates the importance of 3D radiative transfer effects for a range of trace gas remote sensing applications such as ground-based MAX-DOAS and airborne imaging spectroscopy. To study these effects, 1D-layer and 3D-box AMFs were implemented in the Monte Carlo solver MYSTIC of the libRadtran RTM. The computation of AMFs is a central component in most trace gas retrieval algorithms to convert observed SCDs into VCDs, but so far these algorithms were limited to 1D RTMs. In case of a horizontally homogeneous atmosphere and in plane-parallel geometry, the 3D-box and 1D-layer AMFs perfectly agree

Table 3.2 – Estimated NO_2 emissions from the retrieved VCD fields obtained from 1D-layer AMFs under different solar zenith angle (SZA) and solar azimuth angles (SAA).

Scenario	True VCD	Solar zenith angle (with SAA=90°)			
		0°	20°	40°	60°
Line density [$g\ m^{-2}$]	1.30	1.18	1.13	1.13	1.09
Flux [$kg\ h^{-1}$]	42.65	38.61	37.01	37.08	35.62
Relative bias [%]	-	-9.48	-13.22	-13.06	-16.49
		Solar azimuth angle (with SZA=40°)			
		0°	90°	180°	270°
Line density [$g\ m^{-2}$]		0.82	1.13	1.06	1.11
Flux [$kg\ h^{-1}$]		26.83	37.08	34.61	36.47
Relative bias [%]		-37.09	-13.06	-18.86	-14.49

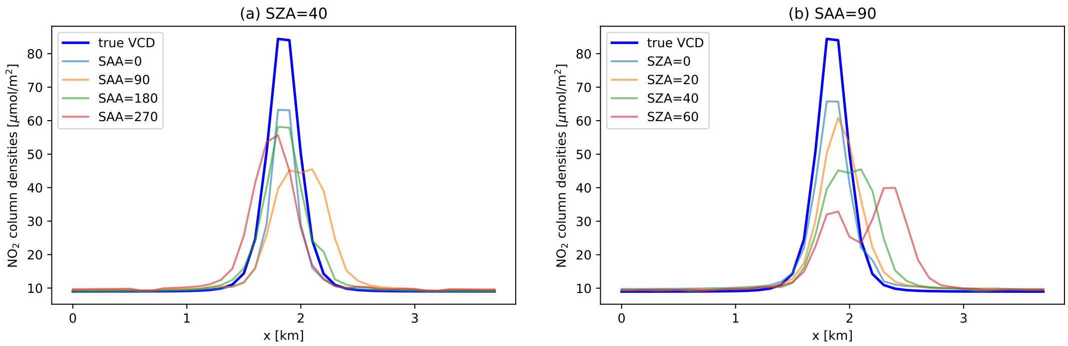

Figure 3.11 – Plume VCD cross section at y=1.6 km (0.3 km downstream of the plume) for (a) the sun at SZA=40° with different SAAs and (b) for the sun in the west with different SZAs

within the statistical noise of the Monte Carlo method. They also agree very well with 1D-layer AMFs calculated with other RTMs presented in a previous model intercomparison study by Wagner et al. (2007).

The importance of 3D effects was demonstrated for two examples. For a ground based MAX-DOAS instrument, we showed that 3D-box AMFs are highest along the line of sight of the instrument (representing photons that have mostly scattered only once), but that the contribution from outside is not negligible and depends on sun position and aerosol optical depth. The spatial distribution of the vertically integrated 3D-box AMFs depends on the sun position, which can be important for interpreting MAX-DOAS observations, especially in urban areas or, more generally, in the vicinity of pollution sources. The spatial variability of the NO_2 distribution in the context of the MAX-DOAS instrument can affect the retrieval differently at different times of the day.

As second example, trace gas retrievals were studied for an airborne imaging spectrometer using simulations of a NO_2 plume emitted by a stack. We showed that when using 1D-layer

AMFs, the NO_2 VCDs in the plume were significantly underestimated (up to 58 %), and that the position of the plume was artificially shifted towards the aircraft. Furthermore, integrals of the NO_2 enhancement in across-plume direction (line densities) were also biased, which results in an underestimation of the NO_2 emissions from the stack when using a mass-balance approach. Using 1D-layer AMFs induces systematic errors even if the NO_2 profile above the ground pixels is known accurately, because a 1D RTM fails to properly represent the complex light path, which is required if the trace gas field is not horizontally homogeneous.

Our study showed that even for simple examples, 3D effects are not negligible if the trace gas field has a high spatial variability. This finding is particularly relevant for ground-based and airborne remote sensing in cities, where considering 3D effects is likely indispensable to reduce systematic errors. This will be addressed in a follow-up study where also the potential impact of 3D radiative transfer effects on the horizontal smoothing of the retrieved trace gas fields will be studied. 3D effects are also important for tomographic inversion (e.g., Frins et al., 2006; Kazahaya et al., 2008; Casaballe et al., 2020) where the application of 3D-box AMFs will minimise errors caused by the use of pure geometric assumptions. The high spatial resolution of the next generation of satellite instruments might make it necessary to also consider 3D effects for space-based trace gas remote sensing. Especially when considering imaging spectrometers with very high spatial resolution to estimate emissions (e.g., Strandgren et al., 2020), 3D radiative transfer effects should be considered and studied. However, since 3D radiative transfer calculations are computationally expensive, efficient methods need to be developed for operational applications that provide an appropriate balance between accuracy and computational cost. To fully benefit of 3D-box AMFs, 3D radiative transfer calculations require high-resolution 3D distributions of trace gases and aerosols to calculate the total AMF. Such fields are generally difficult to obtain. In a follow-up study we plan to use 3D NO_2 fields from a building-resolving urban air quality model (Berchet et al., 2017) with a detailed representation of both near-surface and elevated (stack) emission sources to further analyze the added value of 3D-box AMFs. On the other hand, measuring different azimuth angles with a MAX-DOAS instrument could be used to constrain the 3D fields of trace gases (e.g., Dimitropoulou et al., 2019).

4 Impact of 3D radiative transfer on airborne NO_2 imaging remote sensing over cities with buildings

This chapter was adapted from a publication[1] in the Atmospheric Measurement Technique peer-reviewed journal (Schwaerzel et al., 2021). I designed and implemented the urban canopy module, designed and simulated the 3D scenarios, and wrote the article. Fabian Jakub and Claudia Emde contributed to the design and implementation of the urban canopy module. Gerrit Kuhlmann contributed to the design of the study scenarios. All coauthors contributed by reviewing the manuscript.

[1] Schwaerzel, M., Brunner, D., Jakub, F., Emde, C., Buchmann, B., Berne, A., and Kuhlmann, G.(2021). Impact of 3D radiative transfer on airborne NO_2 imaging remote sensing over cities with buildings. Atmospheric Measurement Techniques, 14(10):6469–6482.

Abstract: Airborne imaging remote sensing is increasingly used to map the spatial distribution of nitrogen dioxide (NO_2) in cities. Despite the small ground-pixel size of the sensors, the measured NO_2 distributions are much smoother than one would expect from high-resolution model simulations of NO_2 over cities. As suggested in Chap. 1 and Chap. 3, this could partly be caused by 3D radiative transfer effects due to observation geometry, adjacency effects and effects of buildings. Here, we present a case study of imaging a synthetic NO_2 distribution for a district of Zurich using the 3D MYSTIC solver of the libRadtran radiative transfer library. We computed NO_2 slant column densities (SCD) using the recently implemented 3D-box air mass factors (3D-box AMF) and a new urban canopy module to account for the effects of buildings. We found that for a single ground pixel (50 m x 50 m) more than 50% of the sensitivity is located outside of the pixel, primarily in the direction of the main optical path between sun, ground pixel, and instrument. Consequently, NO_2 SCDs are spatially smoothed, which results in an increase over roads when they are parallel to the optical path and a decrease otherwise. When buildings are included, NO_2 SCDs are reduced on average by 5% due to the reduced sensitivity to NO_2 in the shadows of the buildings. The effects of buildings also introduce a complex pattern of variability in SCDs that would show up in airborne observations as an additional noise component (about $12\,\mu\mathrm{mol\,m^{-2}}$) similar to the magnitude of typical measurement uncertainties. The smearing of the SCDs cannot be corrected using 1D-layer AMFs that assume horizontal homogeneity and thus remains in the final NO_2 map. 3D radiative transfer effects by including buildings need to be considered to compute more accurate AMFs and to reduce biases in NO_2 vertical columns obtained from high-resolution city-scale NO_2 remote sensing.

4.1 Introduction

An attractive possibility to create high-resolution maps (<100 m) of the NO_2 distribution in cities is to use an airborne imaging spectrometer. This was first demonstrated for measurements from the Airborne Prism Experiment (APEX) of a Swiss-Belgium consortium (Popp et al., 2012; Tack et al., 2017) and the Geostationary Trace gas and Aerosol Sensor Optimization (GeoTASO) spectrometer (Nowlan et al., 2016) developed in the United States. A comprehensive comparison between four airborne NO_2 imaging spectrometers flown over the city of Berlin was performed during the AROMAPEX campaign (Tack et al., 2019), which included APEX (Schaepman et al., 2015), AirMAP (Airborne imaging DOAS instrument for Measurements of Atmospheric Pollution) (Schönhardt et al., 2015), SWING (Small Whiskbroom Imager for atmospheric compositioN monitorinG) (Merlaud et al., 2013) and SBI (Spectrolite Breadboard Instrument) (de Goeij et al., 2017; Vlemmix et al., 2017).

NO_2 retrieval algorithms applied to airborne instruments have been derived from algorithms developed for satellite instruments with much lower spatial resolution (> 5 km). These algorithms rely on 1D radiative transfer simulations, which reach their limits at high resolution and in the presence of spatially variable properties of the atmosphere and the surface, as they assume horizontal homogeneity of all parameters within the optical path. As discussed in the previous chapters (Chap. 1 and Chap. 3), a strong indication for the importance of 3D radiative transfer effects is that NO_2 maps obtained from airborne imaging spectrometers over cities are spatially much smoother than one would expect from the instrument resolution and compared to maps obtained from high-resolution city-scale dispersion models, which show, for example, strong gradients in the NO_2 field along major roads (Kuhlmann et al., 2017). A likely explanation is that the measurements are not only sensitive to NO_2 in the vertical column above the observed ground pixels but also to the atmosphere surrounding the pixels, which is known as the horizontal smoothing error or the adjacency effect (Cracknell and Varotsos, 2012; Lyapustin and Kaufman, 2001; Richter, 1990). The adjacency effect has been described especially in the context of high-resolution land-surface remote sensing, but it has also been discussed in the context of atmospheric measurements (e.g., Richter, 1990; Minomura et al., 2001; de Graaf et al., 2016). Evidence for 3D radiation effects due to the presence of clouds in the vicinity of an observed ground pixel has recently been reported for CO_2 observations from the OCO-2 satellite (Massie et al., 2017). Such effects are expected to become increasingly important with the increasing resolution of satellite observations (Schwaerzel et al., 2020). An additional complexity over cities to be accounted for is the effects of buildings on the photon paths due to multiple reflections and shielding of the main optical path.

The aim of this study is to quantify, for the first time, the impact of these 3D radiative transfer (RT) effects in the presence of spatially variable surface properties and NO_2 concentrations over cities on NO_2 retrievals from high-resolution airborne imaging spectrometers. The study builds on the work by Schwaerzel et al. (2020) presented in Chap. 3, where we highlighted the importance of 3D RT effects on trace gas remote sensing for ground-based and airborne instruments. In this study, we also use the MYSTIC RT solver introduced in the previous chapters (Chap. 2 and Chap. 3). The obtained 3D-box AMFs describe the sensitivity of an instrument to a trace gas (here NO_2) in each grid box (Schwaerzel et al., 2020). To account for the effect of buildings, we additionally implemented a new urban canopy feature that represents the full 3D building structure of a city with assigned optical properties of the different surfaces. 3D radiative transfer calculations in the urban canopy are not new, but so far focused only on applications not related to trace gas observations such as the computation of radiation budgets and broadband landscape imaging (Gastellu-Etchegorry et al., 2015). The present study is the first to use such a model to investigate 3D effects on trace gas retrievals over a city. In order to isolate different effects on 3D-box AMFs and on the spatial smoothing of the information retrieved from an airborne instrument, we use a comparatively simple setup with 3D buildings representative of a district in the city of Zurich with uniform optical properties of roofs, walls and streets. The model, however, is able to describe the optical properties of each single surface separately.

4.2 Methods

4.2.1 The MYSTIC radiative transfer solver

To compute the AMFs we use the MYSTIC RT solver. MYSTIC is operated as a RT solver of the libRadtran package (Mayer and Kylling, 2005; Emde et al., 2016) and its 1D-layer AMF and 3D-box AMF modules were extensively described in the previous chapters (Chap. 2 and Chap. 3).

Urban canopy implementation

The urban canopy was implemented in libRadtran as a triangle mesh, where each triangle can be assigned different optical and physical properties. Information on vertex positions and optical properties are read from an input file that has to be generated from a 3D building data set prior to the simulation. Using a ray tracing algorithm newly integrated into the model, MYSTIC detects if and where a photon hits a triangle. The interaction of the photon with the surface (absorption or reflection) is then simulated using preexisting MYSTIC functions.

To create a triangular mesh for each building, a Python script was written that converts buildings stored in an ESRI shapefile into triangles. A building consists of one or several flat roofs and several vertical walls. To create triangles for the roof, we connect the polygon centroid to each polygon corner. Wall triangles are created by splitting each wall diagonally into two triangles. Each triangle surface carries information about its albedo and skin temperature. The skin temperatures are used for thermal simulations, a feature that is not used in this publication. The triangular mesh is stored in a NetCDF file readable by MYSTIC. An example file layout is shown in Appendix C. The file contains the variable `vertices` (shape: $N_v \times 3$, type: double), which is a list of x, y and z coordinates. A mesh of N_t triangles is built from these vertices using the `triangles` variable (shape: $N_t \times 3$, type: int) by storing the indices of the 3 vertices that create the triangles. The variable `materials_of_triangles` (shape: N_t, type: int) is used to assign each triangle the index of a material type. The material types are defined using the variables `material_type` (shape: N_m, type: string), `material_albedo` (shape: N_m, type: double) and `temperature_of_triangle` (shape: N_m, type: double) to assign a name, albedo and temperature to each material.

In MYSTIC, each photon is traced step-wise along its optical path from one interaction to the other. To interact with the urban canopy, a ray tracing code searches for hits with one of the triangles during each step. We use the Star-3D library (https://gitlab.com/meso-star/star-3d) (Villefranque et al., 2019), which is a convenient wrapper for Intel® Embree (www.embree.org) to facilitate efficient ray / triangle intersection tests using a bounding volume hierarchy (BVH).

In the case that a ray hits a surface, a Lambertian reflection happens and a new direction is attributed to the photon, which will continue its path until its next interaction. Absorption on surfaces is accounted for by reducing a photon weight by $1 - albedo$. Currently, the

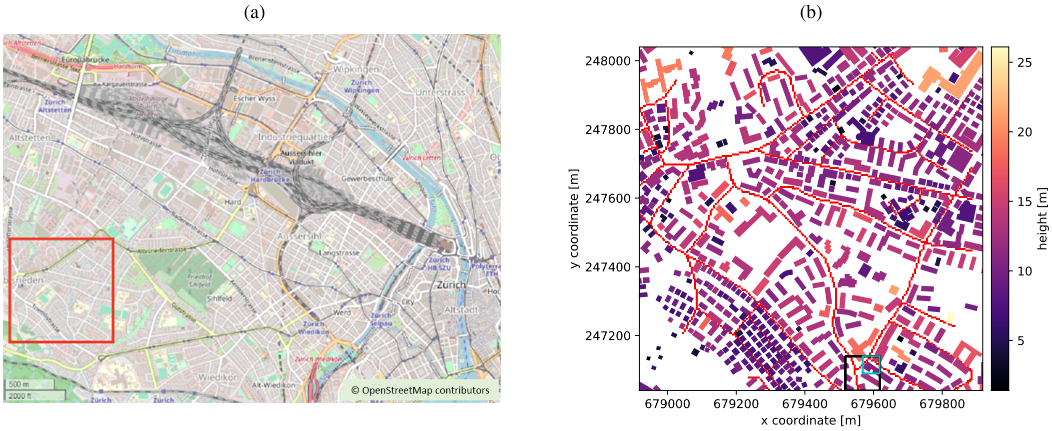

Figure 4.1 – (a) Map of Zurich with the location of the study area in red. Map informations were obtained from OpenStreetMap (© OpenStreetMap contributors 2021. Distributed under the Open Data Commons Open Database License (ODbL) v1.0.) (b) Building heights and major roads in the study area with the lower left pixel at x = 678918 m and y = 247040 m in the Swiss LV03 coordinate system. The black square represents the location of the sub-domain and the cyan square the location of a single pixel observation both used in Section 4.3.3.

urban canopy module only supports Lambertian reflections but an extension, e.g., to specular reflections would be straightforward. For an even more realistic description of the surface reflectance for real applications, BRDF functions would be a well suited method.

4.2.2 Study case in Zurich

To study radiative transfer effects on airborne measurements for a realistic scene, we selected a 1 km x 1 km region in Zurich, Switzerland (see Fig. 4.1a). The low-rise buildings (10-15 m) with simple geometries are rather typical for Swiss cities. The scene includes roads of different widths and orientations and two open areas without buildings.

Buildings

We used 3D building data from a shape file obtained from the Swiss Federal Office of Topography (swisstopo). Each building is defined as a polygon with x and y-coordinate for the edges and the centroid (Swiss LV03 coordinates system) with a single height. As described above, the data was converted to a triangular mesh and saved to a netCDF file. For simplicity, we either applied albedos of 0.1 for walls (identical to the used ground albedo) and 0.2 for roofs or used the same albedo of 0.1 for all surfaces (albedos chosen after Mussetti et al., 2020). Figure 4.1b shows the buildings colored by their heights in the selected model domain.

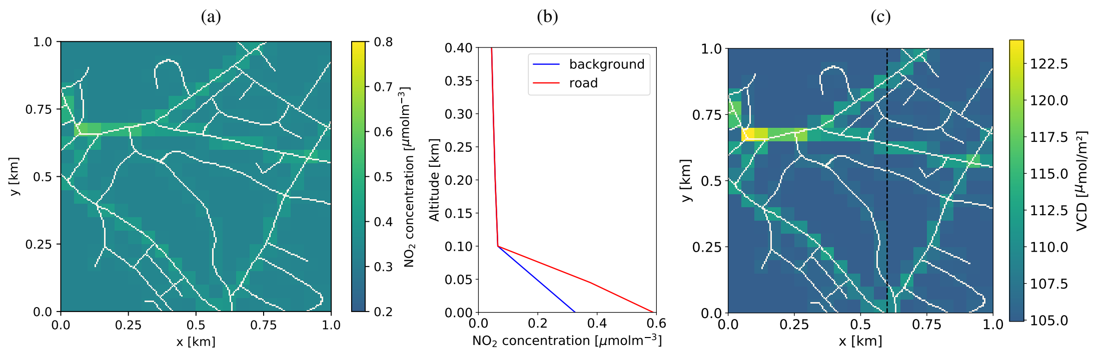

Figure 4.2 – (a) NO_2 ground concentration map. (b) NO_2 vertical profile at a background location (blue line) and over a road at x = 5 m, y = 55 m (red line). (c) Field of vertically integrated NO_2 column densities (VCD) with aircraft flight track overlaid as dashed black line.

Synthetic NO_2 field

We created a simple but quite realistic 3D NO_2 concentration field based on the traffic emission inventory of the city of Zurich (see Table 1 in Berchet et al., 2017). For this purpose, the road emissions available as line sources were rasterized at 5 m x 5 m spatial resolution and normalized by the maximum value in the rasterized field. The normalized field was then multiplied with a NO_2 concentration of 110 $\mu g\, m^{-3}$, which is a typical high concentration measured next to busy streets in Zurich (Bär, 2016). A background NO_2 concentration of 15 $\mu g m^{-3}$ was added using a typical low value observed in Zurich (Bär, 2016) (see Appendix C for details). The maximum concentration is thus 125 $\mu g\, m^{-3}$ or 2.7 $\mu mol\, m^{-3}$. Finally, we smoothed the concentration field with a Gaussian filter with a standard deviation of 5 m to mimic the effect of turbulent dispersion. The synthetic field of the NO_2 near surface concentrations is shown in Fig. 4.2a binned on a 50 m x 50 m grid, which is the typical resolution of trace gas measurements from an airborne instrument like APEX.

The vertical distribution was modelled as a linear decrease from the surface value to the background value of 0.65 $\mu mol\, m^{-3}$ at 100 m. Above 100 m, all profiles decrease exponentially with altitude with an e-folding vertical length scale of 720 m, which was obtained by fitting a function to a measured vertical profile (see Appendix C). Figure 4.2b shows a NO_2 background profile (blue) and a NO_2 profile over the road (red). Figure 4.2c shows the total VCDs over the selected region in Zurich calculated from the 3D NO_2 concentration field. For more details on the generation of the 3D NO_2 field, please refer to Appendix C.

MYSTIC simulations

Our scenario corresponds to an airborne imaging spectrometer flying across the model domain from south to north (y-direction) slightly to the east of the center (x=600 m) at an altitude of 6 km, which represents the flight altitude of an airborne spectrometer (dashed black line in

Fig. 4.2c). The viewing zenith angle was varied in discrete steps to cover the whole domain in across-flight direction (i.e. in east-west direction). For simplicity, the sun was placed at an azimuth angle (SAA) of either 90° (i.e. west) or 0° (i.e. south). The solar zenith angle (SZA) was set to 60°, which corresponds to values in the morning or afternoon in summer over Zurich. Simulations with a SZA of 30°, which correspond to typical summer noon measurements over Zurich are shown in Appendix C.

The simulations were conducted for a standard atmosphere and for a wavelength of 490 nm, which is the center of the NO_2 fitting window used for the APEX instrument (Kuhlmann et al., 2016). NO_2 absorption features at shorter wavelengths typically used in satellite retrievals are less suitable for APEX due to the high instrument noise at those wavelengths. Note that 3D effects would be stronger at shorter wavelengths due to enhanced Rayleigh scattering. Aerosols were only included in the simulations as a case study to analyse the footprint of the spectrometer (see Sect. 4.2.3). Table C.1 in Appendix C provides an overview of the MYSTIC input parameters used in the simulations.

To resolve the spatial variability of surfaces and elevations within each 50 m x 50 m ground pixel, we specified an instrument opening zenith angle corresponding to the 50 m pixel size in x-direction and moved the aircraft in 10 discrete steps of 5 m along the y-direction. The 10 different 3D-box AMF fields computed in this way were then averaged to a single field per pixel. The 3D-box AMFs were then used together with the synthetic NO_2 field to compute total SCDs that would be observed from an airborne instrument (see numerator in Eq. 2.5). Then, the total AMFs were calculated dividing the total SCDs by the total VCDs. In the same way we also computed SCDs ignoring buildings and SCDs based on 1D-layer AMFs (Eq. 2.4). Differences between the three types of SCDs can be attributed to 3D and building effects. Since in real applications VCDs would be computed from SCDs, we also use the SCD field calculated with 3D-box AMFs including buildings as the "true" SCD measured by the airborne spectrometer and calculate the VCD field using total AMF calculated from 1D-layer AMFs and 3D-box AMFs without considering buildings to show the errors caused by these simplifications.

4.2.3 Footprint of an airborne spectrometer

To study the sensitivity of a single measurement to the surrounding of the ground pixel, we simulated the horizontal distribution of 3D-box AMFs close to the ground for a single observation scenario. The simulations were conducted without aerosols and for a typical urban aerosol scenario with an aerosol optical depth (AOD) of 0.1. For the scenario, the sensor was placed at x = 675 m and y = 75 m pointing at a ground pixel with the lower left corner located at x = 650 m and y = 50 m. The corresponding VZA was 0.72° in the center of the pixel and the VAA was 270° (instrument pointing eastwards) (for details see also table C.1 in the Appendix C).

To obtain a map of the close-to-ground NO_2 sensitivity of a single ground pixel measured by an airborne imaging spectrometer during a flight overpass, we simulated AMFs with a 5 m x

5 m horizontal resolution and a 5 m vertical resolution in the lowest 45 m above ground for 10 equally-spaced instrument opening zenith angles corresponding to the 50 m pixel size in x-direction and moved the aircraft in 10 discrete steps of 5 m along the y-direction. We averaged the obtained 100 AMFs fields, integrated them vertically for the first 45 m and scaled the result by the sum of all pixels to finally obtain a 2D map of the fraction of the sensitivity within one 5 m x 5 m grid cell. In the following, this will be called the NO_2 footprint of an airborne spectrometer.

4.3 Results

In this section we first show the instrument incoming radiance calculated with MYSTIC over the selected study area. Second, we analyze the 3D-box AMFs for a single NO_2 observation both in the vertical and in the horizontal and compare results with and without buildings. Finally, we compare total AMFs for the complete image obtained from an airborne instrument flying over the study domain as illustrated in Fig. 4.2c between the solution obtained with the 3D and the 1D RTM to illustrate the importance of 3D radiative transfer effects on the SCD measurements.

4.3.1 Incoming radiance

An airborne imaging spectrometer measures radiance from back-scattered and reflected solar irradiance. Figure 4.3 shows the instrument incoming radiance at 490 nm for the selected region with the urban canopy. Note that for this example the instrument was placed in the center of the domain at an altitude of 6 km observing the scene with a very wide opening angle of about 10° to cover the full 1 km x 1 km domain. The sun is located in the west with a SZA of 60°. The surface reflectance was set to 0.10, while the reflectance of roofs and walls was set to 0.20 in this example.

Since building surfaces have higher reflectance in this example, the bright building roofs clearly stand out. Some bright walls illuminated by the sun can be seen in the east of the domain. Shadows are also clearly visible in the east of the buildings with taller buildings producing longer shadows. This radiance field is closely related to the close-to-ground NO_2 sensitivity. NO_2 over a bright surface can more easily be detected than NO_2 over a dark surface. In case of a pixel covered by both bright and dark surfaces, the retrieved signal will be more strongly affected by NO_2 above the bright parts.

4.3.2 3D-box air mass factors for a single observation

Vertical distribution along the main optical path

3D-box AMFs have a distinct 3D distribution for each ground pixel. Figure 4.4a shows an example of the 3D-box AMFs projected onto a 2D (x-z) plane by integrating in y-direction for

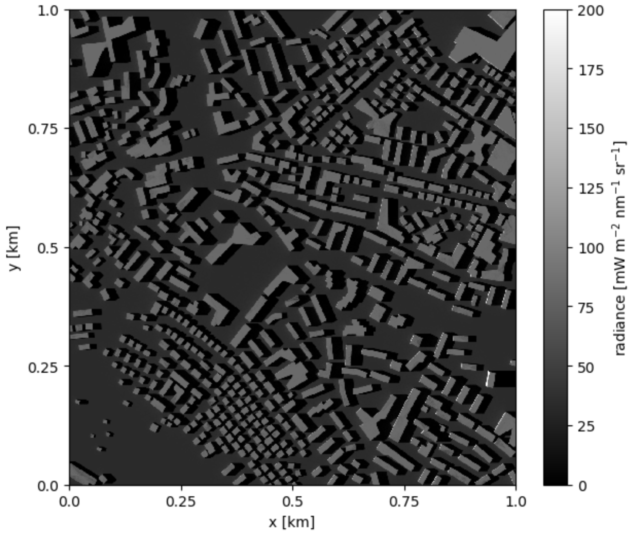

Figure 4.3 – Radiance seen by a downward viewing instrument placed in the center of the 1 km x 1 km region at an altitude of 6 km. SZA and SAA are 60° and 90°, respectively.

an instrument pointing almost in nadir direction at the ground pixel centered at x=675 m and y=75 m (cyan square in Fig. 4.1b). Since the pixel is partly covered by buildings, 3D-box AMFs close to the ground (0-10 m) are smaller than those above roof level. Note that in this and all the following simulations all surfaces have a constant albedo of 0.1. Most photons follow the geometric path from the sun to a reflection on the ground or the roof and to the instrument as indicated by the high 3D-box AMFs along this path. Figure 4.4b shows the 1D-layer AMFs obtained by integrating the 3D-box AMFs in x- and y-direction. The decrease close to the ground due to the buildings is clearly visible. Figure 4.4c shows column AMFs along the x-axis, i.e. 3D-box AMFs integrated in y- and z-direction. AMFs in the column directly below the instrument are highest, because the collected photons cross at least one of the column boxes when they are scattered into the direction of the instrument. The column AMFs decrease in the x-direction with distance to the instrument due to atmospheric absorption and scattering.

Since 3D-box AMFs inform about the sensitivity to NO_2, we can conclude that the measurement is mainly sensitive to NO_2 along the geometrical optical path. It is not very sensitive to adjacent pixels and also not to NO_2 at the surface because of the blocking of the photon path by buildings. The total AMF for the observation presented in this example computed with Eq. 2.5 is 1.98. The VCD above the ground pixel is 121 $\mu mol\ m^{-2}$ and the SCD computed as VCD times total AMF is 239 $\mu mol\ m^{-2}$.

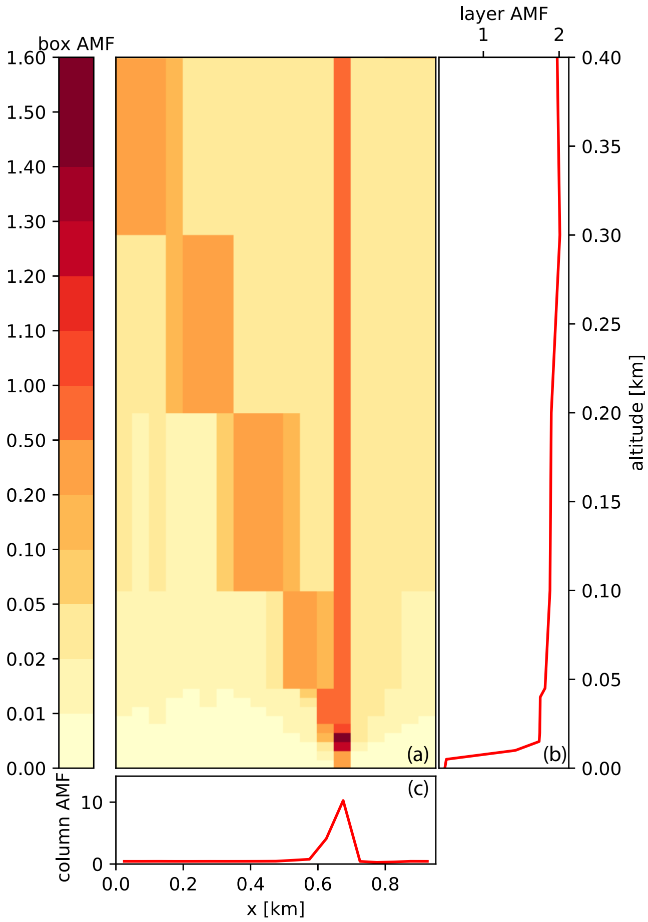

Figure 4.4 – (a) Integrated 3D-box AMFs in y-direction for a ground pixel at x=650 m and y=50 m (lower left corner) for an instrument placed at x=600 m, y=75 m and z=6000 m. The sun is at SAA = 90° (west) with a SZA of 60°. (b) Vertical profile of horizontally integrated AMFs (1D-layer AMFs) and (c) Horizontal profile of vertically integrated AMFs (column AMFs).

Horizontal footprint

To further illustrate the horizontal sensitivity of an airborne spectrometer to layers close to the ground, Fig. 4.5 shows the near-surface footprint defined as the vertically integrated 3D-box AMFs from 0-45 m above ground (see Sect. 4.2.3). The same scene was simulated as in the previous paragraph but with a higher horizontal resolution of 5 m x 5 m to illustrate the spatial pattern of the sensitivity in greater detail. The figure is normalized to show the fraction of the sensitivity represented by each 5 m x 5 m pixel.

Figure 4.5a shows the footprint for a flat surface without buildings without including aerosols. An important part of the sensitivity (51.4%) is located outside the ground pixel. The instrument will thus not only 'see' near-surface NO_2 above the ground pixel but also NO_2 outside. A major part of the sensitivity is located in the direction of the sun along the main optical path. The

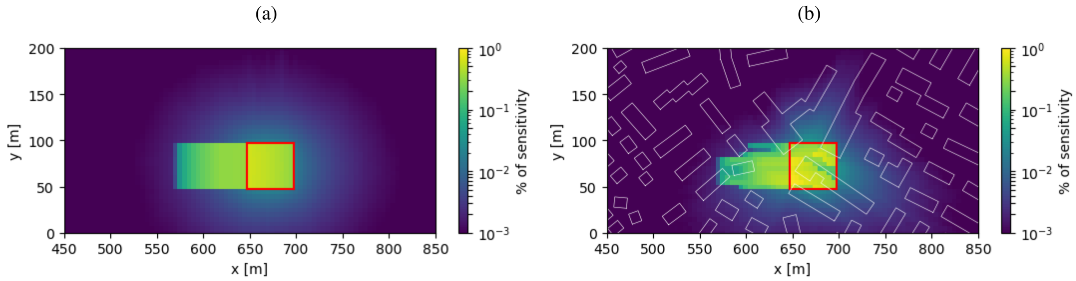

Figure 4.5 – (a) Footprint without buildings. 51.4% of the signal is located outside the ground pixel (i.e. outside the red frame). (b) Footprint with buildings. 52.6% of the instrument sensitivity is located outside the ground pixel. Building contours in white.

main optical path is dominated by photons that are either reflected from the ground pixel surface or scattered in the atmosphere above the ground pixel one single time upward into the direction of the instrument. A much smaller fraction is located outside this main path and is caused by photons experiencing at least one more scattering (or reflection) event before being scattered (or reflected) into the main optical path.

Figure 4.5b presents the same situation but with buildings added to the simulation. Buildings affect the sensitivity both within and outside the ground pixel. The footprint is reduced in the shadows of buildings but may be enhanced over the sunlit sections of streets due to multiple reflections, as seen near the upper right and lower left corners of the ground pixel. In this example, the part of the sensitivity located outside the ground pixel is 52.6%, comparable to the simulation without buildings.

Figure C.7 in the Appendix C shows the footprint for the aerosol scenario. The aerosol scattering increases the sensitivity contribution from outside the ground pixel to 55% for both the scenario without and with buildings. The contribution from outside the main optical path is increased to 25% and 32% without and with buildings, respectively, compared to 18% and 24%, when not including aerosols.

The main effect of the 3D optical path of the photons is thus to smear out the sensitivity of a measurement into the direction of the main optical path, which is determined by the viewing and illumination geometry. The presence of buildings further modifies the sensitivity by adding a complex pattern of enhancements and reductions due to the shielding effects of buildings and multiple reflections in street canyons.

4.3.3 Impact of 3D radiative transfer on NO_2 imaging over a city

In the previous section we have shown how 3D radiative transfer effects and buildings smear out and modify the sensitivity of a single observation. Here we demonstrate how a complete image of NO_2 slant columns is affected by these effects. Note that for simplicity in the following

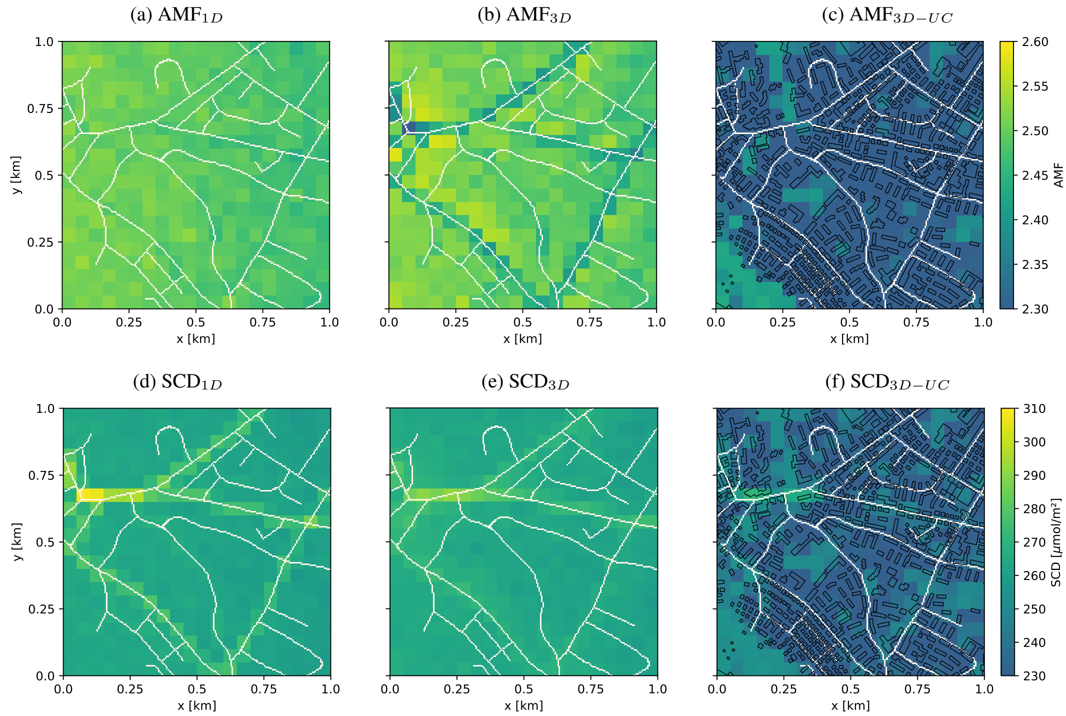

Figure 4.6 – AMFs for a simulation with SAA of 90° with 1D-layer AMFs simulation (a), 3D-box AMFs without (b) and with (c) buildings. The respective SCDs are shown in the lower row (d,e,f). Roads are drawn in white and building contours in black for the simulation with buildings.

simulations, the ground and building reflectance was set to 0.1.

Effects of 3D radiative transfer and buildings on slant column densities

Figure 4.6 compares total AMFs computed from 1D-layer AMFs (Eq. 2.4) with total AMFs computed from 3D-box AMFs (Eq. 2.5) without and with the urban canopy. The corresponding SCDs are presented in the lower row of the figure, which are related to the total AMFs by a division with VCDs shown in Fig. 4.2c (see Eq. 3.1 and Eq. 2.5). In the following we refer to the SCDs calculated from 1D-layer AMFs as SCD$_{1D}$ and to the SCDs calculated from 3D-box AMFs without and with the urban canopy as SCD$_{3D}$ and SCD$_{3D-UC}$, respectively.

AMFs derived from 1D-layer AMFs (Fig. 4.6a) are almost horizontally homogeneous. They vary only slightly with the instrument viewing zenith angle and the NO_2 distribution. The contribution of the a priori NO_2 profile is only significant, when high values collocate with high 1D-layer AMFs values, but as our a priori NO_2 profiles only differ in the lower 100 m, the effect is smaller than the noise of the Monte Carlo simulations ($\sigma_{\mathrm{AMF}} = 0.014$ and $\sigma_{\mathrm{SCD}} = 1.46\,\mu\mathrm{mol\,m}^{-2}$). The corresponding SCDs (Fig. 4.6d), computed as the sum of the product of

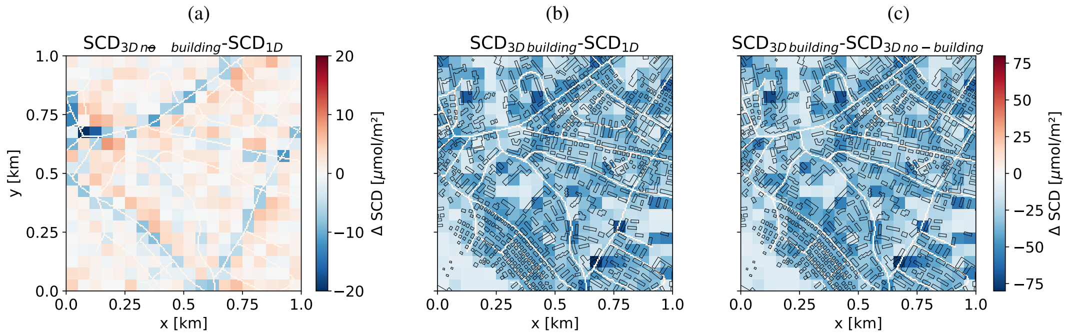

Figure 4.7 – (a) Difference plot between SCDs calculates with 3D-box AMFs and the SCDs calculated with 1D-layer AMFs. (b) Difference plot between SCDs calculated with 3D-box AMFs including the urban canopy and SCDs calculated with 1D-layer AMFs. (c) Difference plot between SCDs calculated with 3D-box AMFs with and without including the urban canopy.

the 1D-layer AMFs with the 1D NO_2 profile (see Eq. 2.4) in Fig. 4.2b show the same pattern as the VCDs with sharply elevated values above roads and a homogeneous background aside. The SCDs are higher than the VCDs because the AMFs are larger than 1.

AMFs calculated with 3D-box AMFs but without buildings (Fig. 4.6b) are lower over the roads and slightly larger just aside the roads, because the 3D-optical path crosses neighbouring columns with decreased or increased concentrations, respectively. This results in a spatial smearing of SCDs (Fig. 4.6e) mainly in the direction of the main optical path from the sun in the west, to the ground pixel and to the instrument in the east of the center. Far from the roads, the SCDs are homogeneous and more or less identical to the 1D solution. The difference SCD_{3D} minus SCD_{1D} is presented in Fig. 4.7. The smearing effect in the 3D solution is visible as negative differences over the roads and positive differences aside especially on the eastern side of the roads opposite to the sun. As a result, the individual roads show up much less prominently in the SCD_{3D} except for roads parallel to the optical path. The reason for this pattern is illustrated in Fig. 4.8, where the main 3D optical path of the photons collected when viewing directly at the road (red path 1 in Fig. 4.8) misses some of the enhanced NO_2 concentrations in the elevated levels above the road. In contrast, these enhanced NO_2 values are 'seen' by photons collected when viewing to the east of the road (green path 2 in Fig. 4.8). In the 1D solution, the SCDs are only affected by NO_2 in the vertical column directly above the observed ground pixel.

The mean difference between SCD_{1D} and SCD_{3D} is around 1 $\mu mol\,m^{-2}$ (relative difference of 0.02 %), which suggests that the signal is smeared, but the total amount of measured NO_2 is almost conserved. A small difference is to be expected because of statistical noise from the Monte Carlo method (about 1.3 $\mu mol\,m^{-2}$ for 50000 photons).

AMFs calculated with the 3D-box AMFs module including the urban canopy (Fig. 4.6c) also show lower values over roads compared to AMFs calculated with 1D-layer AMFs. In addition,

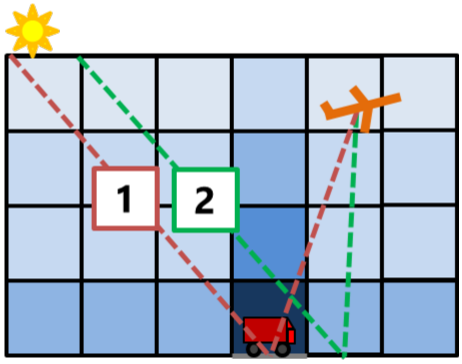

Figure 4.8 – Sketch of two main optical paths for an airborne spectrometer pointing at (1) a road in grey and (2) at a pixel aside the road.

they also show lower values over areas with buildings. As a consequence, the SCDs shown in Fig. 4.6f are lower over regions with many buildings. On average, SCD_{3D-UC} are 12% lower than SCDs without buildings. The standard deviation of the difference between SCD_{3D-UC} and SCD_{3D} is 12.3 µmol m^{-2} for the whole domain. Not including the urban canopy would therefore underestimate VCDs by 12% and would add a source of noise in the image of about 5% for this particular scenario with rather low buildings. In areas with background NO_2 and no buildings (e.g., lower left region) SCD_{1D}, SCD_{3D} and SCD_{3D-UC} closely agree (Fig. 4.7c).

The results presented above were obtained for the special situation where viewing and illumination directions were along the same east-west direction. In this case, the smearing effects are most prominent along this axis but relatively small in perpendicular direction. Here, we also analyze the situation where the sun is in the south and thus viewing and illumination directions are perpendicular to each other. As shown in Fig. 4.9, the results are generally similar but building shadows and correspondingly reduced SCDs are now found to the north instead of the east of the buildings. Furthermore, the SCDs tend to be lower because the main optical path and the corresponding smearing is both N-S (sun to ground pixel) and E-W-oriented (ground pixel to the instrument). The mean difference between SCD_{3D-UC} and SCD_{3D} is 12% and the standard deviation is 13%.

3D effects at higher spatial resolution

To investigate the reduced SCDs over buildings observed in the former paragraphs, we analyse the spatial distribution of SCDs within the 50 m x 50 m pixel in more details. For this purpose, we ran additional simulations at higher spatial resolution (5 m x 5 m) for a 100 m x 100 m sub-domain located at x=600 m and y=0 m (lower-left corner of the sub-domain) of the original domain. SCDs were calculated from 3D-box AMFs with and without buildings (Fig. 4.10a and b).

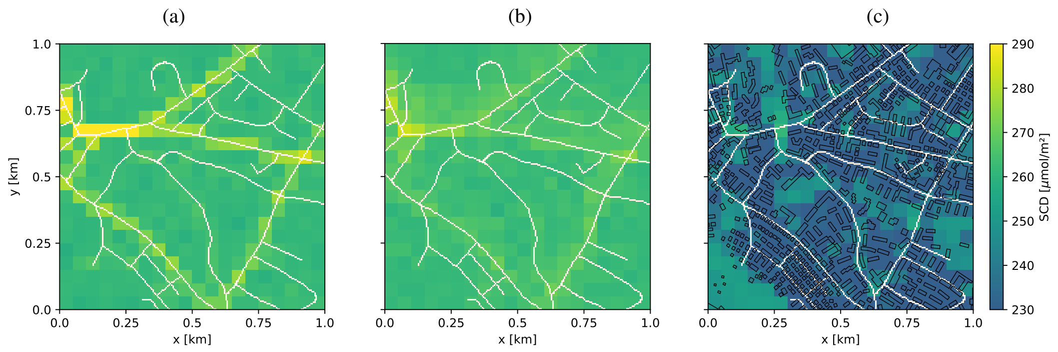

Figure 4.9 – SCDs for simulations with a SAA of 0° with 1D-layer AMFs (a), 3D-box AMFs simulation without (b) and with (c) buildings. The roads are drawn in white and the building contours in black for the simulation with buildings.

At this resolution, we can better resolve the spatial distribution of NO_2 and SCDs remain high above roads. Since we can also resolve individual buildings and their shadows, the simulations makes it possible to investigate how buildings reduce SCDs.

At 5 m resolution, we distinguish four types of ground pixels. (1) The ground pixel is on the surface and the geometric path to the sun and the instrument is not obscured by buildings. In this case, the 3D-box AMFs are only affected by buildings through multiple scattering either increasing the AMF when buildings reflect photons towards the ground pixel or reducing the AMF when buildings block photons from reaching the ground pixel. In our example, the effect results in a small but hardly visible reduction of AMFs (see Fig. 4.10c).

(2) The reflecting point of the geometric path is located on top of a building. The case is similar to the first case, but 3D-box AMFs are smaller, because photons cannot reach the ground. Since we assume that a priori VCDs are fixed regardless of the presence of a building, SCDs are reduced above buildings. However, the effect is very small because only about 3 % of the total VCD is below a 10 m building.

(3) In the third case, the ground pixel is located on the sunlit side of a building, but the direct path to the instrument is blocked by the buildings. Since the VZAs of the simulated instrument are very small, we do not find these cases in our example with rather small buildings.

(4) In the final case, the ground pixel is located in the shadow of the buildings blocking the direct path towards the sun. In this case, photons can only reach the instrument after multiple scattering or simple atmospheric scattering directly into the direction of the instrument, which drastically reduces the 3D-box AMFs near the surface. As a result, SCDs are significantly lower in the shadows of buildings (Fig. 4.10b). For example, SCDs are about 35% lower when increased ground NO_2 concentrations (e.g., road) are located in the shadow of a building.

We can therefore conclude that the reduction of SCDs over buildings (Fig. 4.7c) is mainly

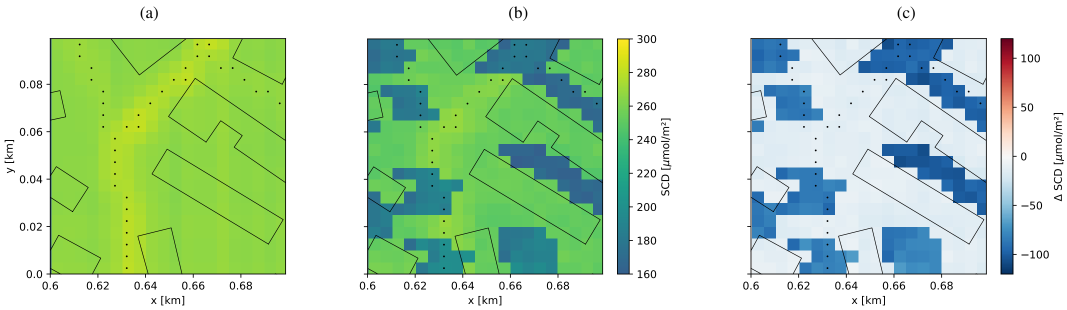

Figure 4.10 – SCDs over a small sub-domain computed from high-resolution 3D-box AMFs simulated without (a) and with (b) buildings and the difference between both (c). In the simulation the sun was located in the west at a SZA of 60°. The albedo of roofs, walls and streets was set to 0.1. Roads are included as black dots and building contours as black lines.

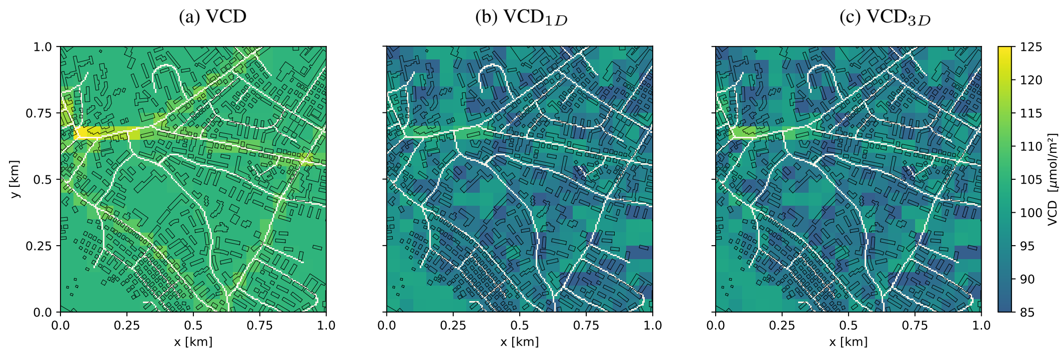

Figure 4.11 – (a) True VCD field and VCDs computed from SCDs using 3D-box AMFs and buildings assuming (b) 1D-layer AMFs and (c) 3D-box AMFs without buildings. The scenario uses a SAA of 90°.

caused by the building shielding effect (case 4), while building height has a minor effect on the SCDs (case 2) in our study case with rather small buildings.

The retrieval of vertical column densities

In imaging remote sensing, NO_2 VCDs are retrieved from SCDs using AMFs. Here SCD$_{3D-UC}$ are considered as the "true" SCDs measured by an airborne imaging spectrometer and VCDs were calculated using either 1D-layer AMFs or 3D-box AMFs without buildings (Fig. 4.11). The VCDs computed with 1D-layer AMFs fails to correct for the spatial smoothing induced by the complex 3D optical path of the photons (Fig. 4.11b). In additions, the effects of buildings are not corrected resulting in additional noise introduced by shielding effect of the buildings and significantly lower VCDs with a field average of 90.1 μmol m^{-2} compared to the 108.4 μmol m^{-2} of the true VCDs. When VCDs are computed using 3D-box AMFs without buildings, the spatial smearing is corrected but the noise component and lower VCDs (mean: 91.4 μmol m^{-2}) would remain in the retrieved VCDs.

4.3.4 Application to real observations

The codes developed for this study can also be applied to real observations, for example, to the campaigns conducted with APEX imaging spectrometer. A major challenge is to obtain the required input data. 3D building data are available for many cities, but albedos for ground, roof and walls are generally not available. In addition, to compute the total AMFs, realistic 3D NO_2 fields from a building-resolving dispersion model are required, which requires high-resolution emission inventories and additional model development, because most building-resolving models are not optimized for providing realistic vertical distributions of trace gases or cannot not be applied to a full city at high resolution (Berchet et al., 2017).

To minimize 3D effects when using 1D-layer AMFs, it would be recommendable to obtain the airborne spectrometer measurement around local noon when the SZA is lowest and avoid large viewing zenith angles. However, around noon turbulent atmospheric mixing will be strong and the NO_2 distributions would be smoothed as well.

The computation of 3D-box AMFs with buildings is computationally quite expensive, but still manageable for current airborne campaigns. For example, the computation of the 3D-box AMF field for a single APEX pixel (e.g. on Fig. 4.6f) takes about 280 s on a single core of our Linux machine (Intel(R) Xeon(R) W-2175 CPU @ 2.50GHz). Processing a full campaign consisting of about 100'000 pixels takes about 23 days using all 14 cores on the system. However, simulating AMFs for an APEX campaign would not require simulation for a 1 km x 1 km domain. Nonetheless, computing 3D-box AMFs is significantly more expensive than computing 1D-layer AMFs and reducing computation time, for example, by finding suitable parametrizations using machine learning, would make it possible to calculate the 3D-box AMFs on smaller hardware, for larger campaigns or to run simulations with more details and at higher spatial resolution.

4.4 Conclusions

Airborne imaging spectrometers are increasingly used for high-resolution mapping of NO_2 concentrations in cities. The NO_2 maps obtained in this way were usually found to be rather smooth and seemingly inconsistent with the much more rapidly varying near-surface NO_2 concentration fields seen, for example, in city-scale dispersion model simulations. The observed difference may partly be explained by atmospheric mixing more strongly affecting total columns than near-surface concentrations, but could also be caused by complex 3D radiative transfer effects in cities. To study the latter point, we implemented an urban canopy module into the 3D MYSTIC solver of the libRadtran radiative transfer model. We set up a case study for a 1 km x 1 km domain in Zurich, for which 3D-box AMFs and NO_2 slant column densities were computed for a realistic field of NO_2 concentrations.

Our case study shows that the footprint of a single observation is only partly located over the observed ground pixel and that there is a 'tail' in the direction of the main optical path. In the presented simulations with a SZA of 60° and a 50 m x 50 m resolution, about 50% of the sensitivity is located outside the ground pixel for a nearly-nadir viewing instrument. Only a small but not negligible amount of photons are from outside the main optical path, with 19% for a simulation without aerosols and without buildings and 24% for a simulation without aerosols and with buildings. The effect becomes more important when aerosols are included with 25% and 32% of the sensitivity located outside the main optical path for scenarios without and with buildings, respectively. The footprint fine structure is further modified with the presence of buildings, but the general shape is conserved.

The 3D radiative transfer simulations show that 3D effects introduce significant spatial smearing of high NO_2 concentrations as for example over roads, which 1D-layer AMFs do not include. This results in increasing SCDs when roads are parallel to the main optical path and decreasing SCDs otherwise. When buildings are included, NO_2 SCDs are generally lower due to the shielding effect of buildings. The buildings also introduce a variability in the SCD field with a standard deviation of 12.9 $\mu mol\, m^{-2}$ (5.5%) that would show up as additional noise component of airborne imagers. The magnitude is however slightly smaller than the current NO_2 SCD uncertainty (about 20 $\mu mol\, m^{-2}$ for the APEX instrument), but could be noticeable for instruments dedicated to NO_2 mapping that have lower SCD uncertainties. We also applied 1D-layer and 3D-box AMFs without building to SCDs computed with 3D-box AMFs with buildings showing that 3D radiative transfer simulations are required to correct the smearing effect and that buildings are required to avoid an underestimation of the VCDs.

Generalizing our results to others cities is challenging, because many relevant parameters such as building shapes, surface reflectances and a priori NO_2 distribution vary strongly between different cities. In our case study, we used a surface reflectance of 0.1, which is a realistic value for Zurich but not necessarily for other cities. In general, a higher surface reflectance of the observed ground pixel implies less atmospheric scattering and a higher sensitivity of the instrument to the main optical path and higher albedo of neighbouring pixels increases the sensitivity to this neighbouring pixel. In this study, the simulations were conducted at 490 nm, which corresponds to the center of the fitting window used for NO_2 retrieval from the APEX airborne spectrometer. At shorter wavelength, used by other instruments, scattering increases, which decreases the instrument sensitivity to the main optical path. The footprint simulated with a wavelength of 420 nm (without buildings) shows the increase in scattering and the sensitivity to neighbouring pixels, as 56% of the sensitivity is located outside of the ground pixel.

In conclusion, our case study demonstrates that 3D effects explain the smooth NO_2 field observed by airborne imaging spectrometers, at least partly. Atmospheric mixing can still result in additional smoothing that has not been studied here. Furthermore, buildings reduce

SCDs due to light shielding effect of buildings and add an additional noise component that is difficult to generalize due to the complexity and the heterogeneity of the buildings. The smearing in sun direction can result in features in the maps that are difficult to interpret when the sun position is not known. 3D radiative transfer effects therefore need to be considered when studying NO_2 maps obtained from airborne imagers and might become relevant with future NO_2 satellite instruments that measure NO_2 at spatial resolutions down to 2 km.

Acknowledgment – We want to acknowledge the Swiss Federal Office of Topography (swisstopo) for providing the 3D building data and the city of Zurich for providing the traffic emission inventories.

5 APEX airborne spectrometer NO_2 VCDs and near-surface concentrations obtained with 3D-box AMFs

I implemented the described radiative transfer modules into the Empa APEX NO_2 retrieval algorithm, designed the study with inputs from Gerrit Kuhlmann, and ran the simulations. The APEX data and the GRAMM-GRAL simulations that will be described in this chapter, were provided by Gerrit Kuhlmann.

5.1 Introduction

In the previous chapters (Chapters 3 and 4), we highlighted the effects of 3D radiative transfer on airborne spectroscopy trace gas retrievals. We demonstrated that the complex 3D photon paths affect the instrument sensitivity, in particular in regions where atmospheric and ground optical properties are horizontally inhomogeneous (e.g., cities). With synthetic but realistic examples, we demonstrated that these effects have to be accounted for in high-resolution trace gas remote sensing over cities to avoid additional noise and smearing of the retrieved nitrogen dioxide (NO_2) maps. So far, these effects have not been demonstrated for real remote sensing measurements. In this chapter, we apply the developed methods to real Airborne Prism EXperiment (APEX) airborne spectrometer data collected during three measurement campaigns in Zurich in 2010, 2013 and 2016. We demonstrate that the developed 3D radiative transfer calculations (including complex surface properties) can be implemented in a trace gas retrieval routine and applied to a real dataset. This implementation requires multiple input data and geometrical transformation of the data. We intend to demonstrate that considering 3D radiative transfer improves the quality of the retrieved NO_2 maps compared to NO_2 retrieved with the traditional 1D-layer air mass factor (AMF) calculations. High-resolution NO_2 column (i.e., VCD) maps can be useful to study the spatial variability of the air pollutant in cities, but near surface concentrations are necessary to assess the exposure of the population to the air pollutant. Therefore we also compute near-surface NO_2 concentrations from the APEX data and evaluate the quality of the product, retrieved with the new radiative transfer (RT) modules, by comparing it to in situ NO_2 measurements at air pollution monitoring sites.

This study is divided into three main parts: First, we present the implementation of 3D-box AMFs in the Empa APEX NO_2 retrieval algorithm. Second, we show a case study in a sub-region of an APEX stripe from a campaign in 2013 in Zurich and third, we calculate the near-surface NO_2 concentrations at air pollution monitoring sites in Zurich.

First, we implement 3D-box AMFs and urban canopy modules of the MYSTIC RT solver (see Schwaerzel et al., 2020, 2021) in the Empa APEX NO_2 retrieval algorithm (Popp et al., 2012; Kuhlmann et al., 2022). We present the data pre-processing steps required for a successful RT simulation for an APEX airborne spectrometer dataset.

Second, we evaluate the effects of 3D-box AMFs on SCDs for the APEX spectrometer in Kreis 2 district in Zurich. This region was selected because the near surface NO_2 distribution is expected to be particularly complex with the simultaneous presence of highways, a plume from the Uetliberg highway tunnel exit, industrial facilities, residential areas, a heterogeneity of low and heavy traffic roads, and some background areas (e.g., forest). We simulate SCDs potentially measured by the airborne spectrometer combining 1D-layer AMFs or 3D-box AMFs with a simulated 3D NO_2 distribution from the GRAMM-GRAL city-scale dispersion model. We qualitatively compare the obtained SCD maps with the differential SCD (δSCD) product from the stripe 1 of the 2013 APEX campaign over Zurich. δSCD is the APEX retrieved quantity after undergoing the DOAS analysis and corresponds to a difference of the retrieved

SCD to the SCD retrieved in a remote area (e.g., forest). We also retrieve the VCD field from the APEX measurement over the same study domain using 1D-layer AMFs and 3D-box AMFs including the buildings module for the total AMF calculation. Therewith we demonstrate that 3D-box AMFs can be used to map NO_2 columns from an airborne spectrometer. To compute the total AMF, a 3D NO_2 field from the building-resolving GRAMM-GRAL model, described later, is also required. We also compare the VCDs obtained with the 1D-layer AMFs with VCDs obtained with the 3D-box AMFs.

Finally, we compute the APEX VCDs at the location of air pollution monitoring stations with the 1D-layer and 3D-box AMFs modules and a required 3D NO_2 distribution simulated with the GRAMM-GRAL dispersion model run over a larger domain centered in Zurich. In addition, we retrieve the near-surface NO_2 concentrations at the location of the monitoring stations for 4 different APEX campaigns in Zurich. We then compare the obtained near-surface NO_2 concentrations with ground concentrations measured at the air pollution monitoring stations at the time of the flight.

5.2 Data and methods

Two APEX flights were conducted in Zurich on 26 June 2010 (one in the morning and one in the afternoon), one flight on 30 August 2013 and one on 7 July 2016. During the APEX flights, NO_2 was measured at several operational air pollution monitoring stations maintained by the city of Zurich, the canton of Zurich, and by Empa, the Swiss Federal Laboratories for Materials Science and Technology. Figure 5.1 shows a map with 14 APEX stripes and the 7 air pollution monitoring stations. Table D.1 in the Appendix D presents an overview of the data availability of the monitoring stations for the individual APEX stripes and Tab. D.3 the APEX stripe times in details. In this section we will present the used data and describe the required data processing steps.

5.2.1 Data and data pre-processing

MYSTIC input data

MYSTIC requires diverse input data for the AMF calculation (see a MYSTIC input file example in Appendix A). These data were obtained from the APEX products as well as from a building dataset of the Swiss Federal Office of Topography (swisstopo). Before simulating the AMF, part of the input data requires processing to align the APEX measurement grid with the MYSTIC simulation grid.

MYSTIC aerosol setting

For the following simulations, aerosol scattering is considered assuming an aerosol optical depth (AOD) of 0.1 for a default aerosol profile from the libRadtran package (aerosol profiles

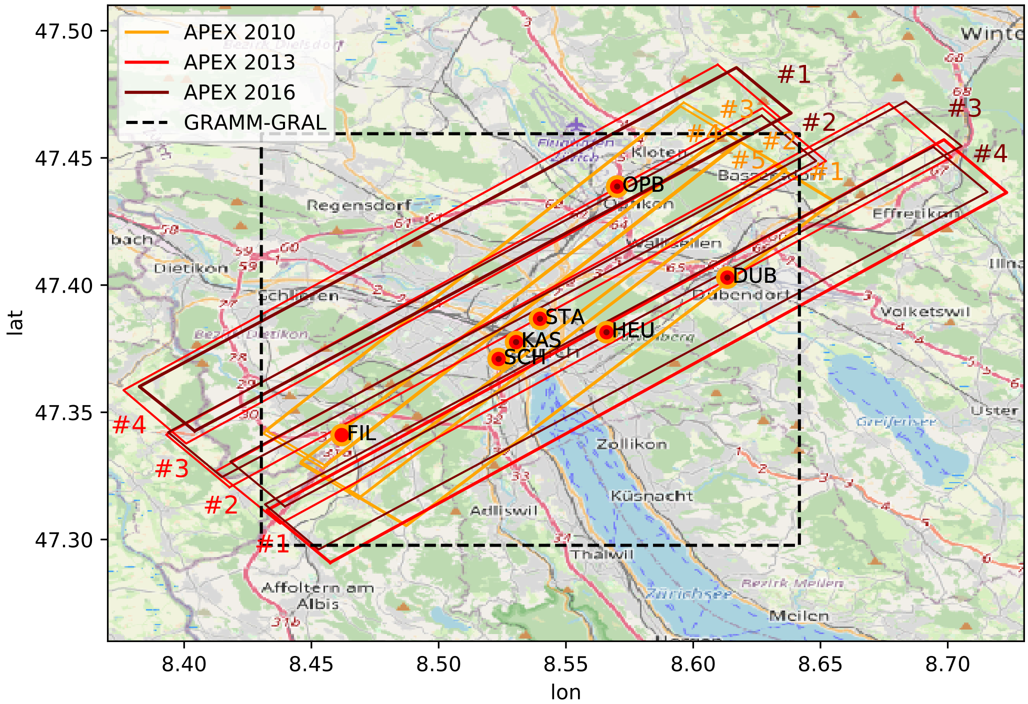

Figure 5.1 – Map of Zurich with APEX flight stripes and locations of monitoring stations. Map informations were obtained from OpenStreetMap (© OpenStreetMap contributors 2022. Distributed under the Open Data Commons Open Database License (ODbL) v1.0.). The 2010, 2013 and 2016 flight stripes are shown in orange, red and brown, respectively. The extent of the GRAMM-GRAL NO_2 field is shown as a dashed black square. The APEX stripes numbers and the available ground measurement stations with colored numbers and circles, describing the year of measurement. More details about the measurement stations are available in Tab. D.1 in Appendix D.1

set after Shettle (1989)). Based on Aqua/MODIS AOD observations for the campaign days, an AOD of 0.1 is a reasonable setting for aerosols in the city of Zurich.

MYSTIC domain as a reference

For each observed APEX pixel, a MYSTIC domain is defined for the AMF calculation. For the MYSTIC grid definition, we use a regular horizontal grid (9 x 9 grid cells) that is oriented in the east-west (x) and north-south (y) directions with a defined origin (x=0 and y=0) in the lower left corner of the domain. The resolution of the MYSTIC grid cells is defined based on the APEX pixel size (see blue MYSTIC grid in Fig. 5.2a). In Chap. 4, we showed that the APEX footprint in the lowest 45 m is mostly within 100 m horizontal distance from the ground pixel for a SZA of 60°. Applied to the used APEX stripes, the chosen 9 x 9 grid cells of the MYSTIC domain (i.e., 450 m wide domain for 9 APEX pixels of 50 m) are sufficient to capture the horizontal

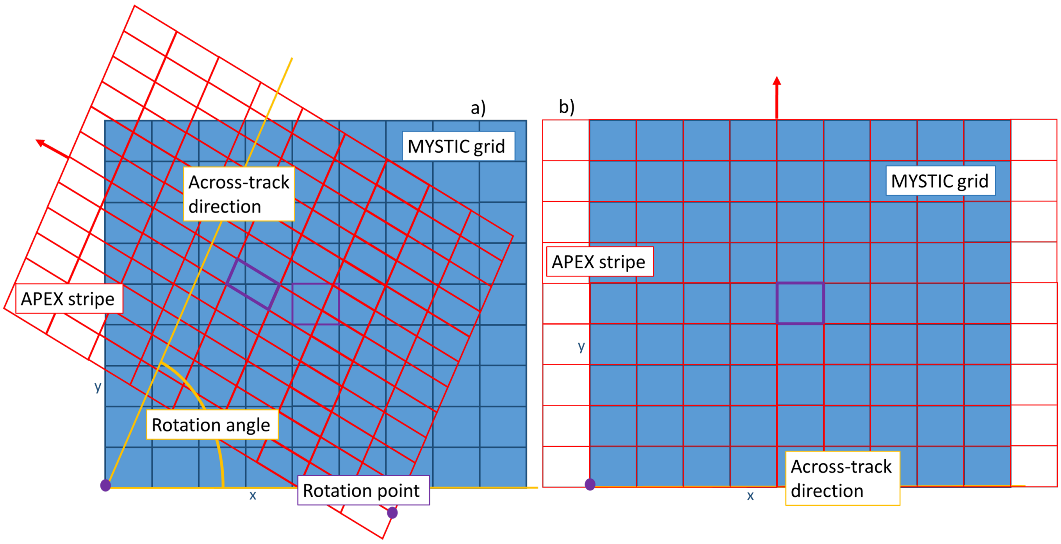

Figure 5.2 – (a) Sketch of the rotation angle with the APEX stripe (red), the MYSTIC grid (blue), the rotation angle (orange), the APEX ground pixel (violet grid cell), and the rotation origin point (violet dot). The rotation angle is given by the angle between the APEX across track direction (orange) and the MYSTIC x-direction (orange). (b) Sketch of the rotated and shifted APEX stripe (red) and the MYSTIC grid (blue)

variations in the NO_2 distribution in the lowest 140 m in the AMF calculation. This grid does usually not match the orientation of the APEX stripe and we therefore need to rotate the APEX spatial information to a grid aligned with the x- and y-directions (see schematic in Fig. 5.2). The rotation angle is given by the angle between the APEX across-track direction and the MYSTIC x-direction (orange rotation angle in Fig. 5.2a). For each APEX pixel, the APEX stripe is rotated around a rotation center located 4.5 pixels lower and 4.5 left of the center of the observed pixel regarding direction of the APEX stripe (violet rotation point in Fig. 5.2a).

The rotated APEX stripe is then shifted horizontally (i.e., translated) until the APEX origin (225 m south and 225 m east from the observed pixel center, i.e., 4.5 grid cells) matches the MYSTIC origin (0 m, 0 m) (see final overlapping grids in Fig. 5.2b). This shift will be referred to as the horizontal shift in the following.

Rotation and shift of the MYSTIC input parameters

The sensor position, the solar azimuth angle, and the instrument azimuth angle, obtained from the APEX product, are rotated by the rotation angle and shifted by the horizontal shift defined in the previous paragraph. The *mc_panorama_view* MYSTIC parameter is used to set two instrument opening angles (ϕ and θ) for the photons entering the instrument optics. This opening angle is defined to collect all photons reflected at diverse locations in the rectangular APEX ground pixel. The MYSTIC vertical resolution is defined to match the vertical resolution of the GRAMM-GRAL model output, which will be described in the following.

Buildings data processing

Each building is defined as a polygon with x and y-coordinates of the edges and the centroid (Swiss LV03 coordinates system) with a single building height. As described in Chapter 4, the data was converted to a triangular mesh and saved to a netCDF file. The triangle vertices were rotated with the defined rotation angle to match the MYSTIC domain definition and shifted by the previously defined horizontal shift. The roof and the ground reflectance are set to the value from the APEX reflectance product at 490 nm averaged over the ground pixel. 490 nm is the center of the NO_2 fitting window used for the APEX instrument (Kuhlmann et al., 2016). The reflectance of the walls is assumed to be 0.1, which we assume to be a realistic assumption for Zurich on average.

GRAMM-GRAL simulations

The Graz Mesoscale Model - Graz Lagrangian Model (GRAMM-GRAL) modelling system is being developed at the Graz University of Technology since 1999. The modelling system combines a mesoscale meteorology model (GRAMM) and a micro-scale Lagrangian particle dispersion model (GRAL). First, the GRAMM model calculates the flow fields accounting for topography, vertical wind profiles and a turbulence class in the input parameters. Second, the GRAL model uses the GRAMM mesoscale flow field to compute a high resolution flow field considering buildings before tracking particles released into the model domain at the location of sources proportional to the intensity of each source. The released particles are counted in the defined counting grid. By scaling the particles amount with the emissions from an emission inventory, the trace gas concentration is obtained for every grid cell (Oettl, 2016, 2017).

The GRAMM-GRAL simulations are run for the Zurich region and the surrounding regions covered by the APEX stripes. The 3D building data in the city of Zurich was obtained from a vectorial building inventory provided by the municipality of Zurich. Buildings outside the city were obtained from a shape file provided by Swisstopo (see Chap. 4) (Berchet et al., 2017). The GRAMM-GRAL modelling system accounts for buildings and topography for the computation of the flow fields. In the GRAMM-GRAL simulations for the following studies, the topography was ignored, as the GRAMM-GRAL output showed erroneous NO_X fields when the topography was used. The GRAMM-GRAL model writes out the mean NO_X concentrations for 10 m thick vertical layers up to 1 km. We then convert the GRAMM-GRAL NO_X output field to a NO_2 field using the NO/NO_2 empirical equation from Düring et al. (2011). The GRAMM-GRAL 10 m x 10 m resolution NO_2 field is then mapped on the APEX grid by averaging the GRAMM-GRAL NO_2 concentrations of grid cells located in the APEX-pixels. Finally, we add a background NO_2 profile from the US Standard Atmosphere (United States Committee on Extension to the Standard Atmosphere, 1976) to the 3D NO_2 distribution.

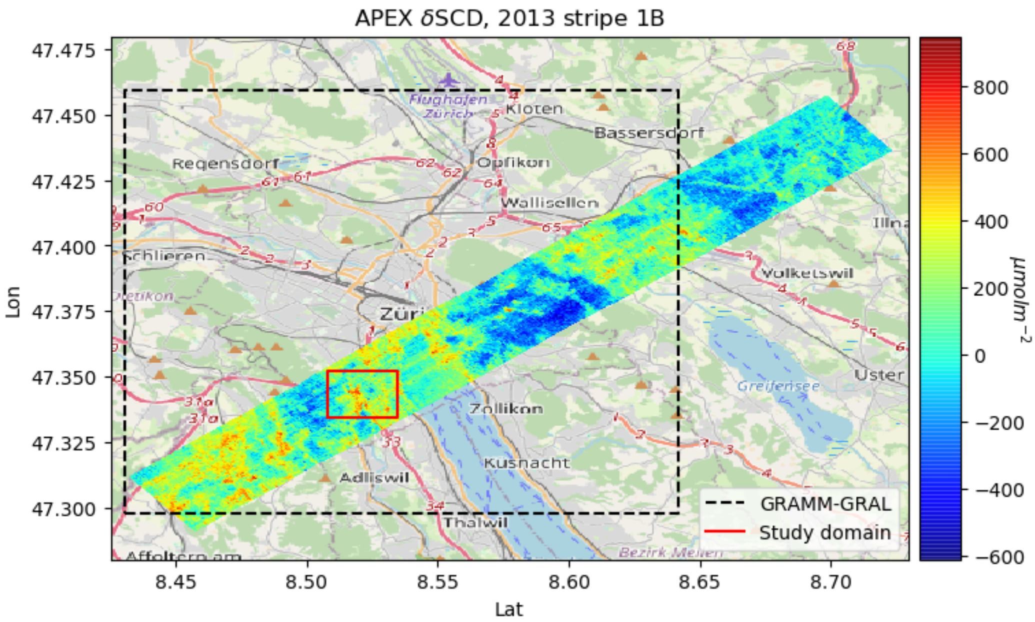

Figure 5.3 – Location of the Kreis 2 study area (red) mapped on the δSCD APEX product from stripe B01 from the 2013 campaign. The extent of the GRAL domain is plotted in blue. Map informations were obtained from OpenStreetMap (© OpenStreetMap contributors 2022. Distributed under the Open Data Commons Open Database License (ODbL) v1.0.)

5.2.2 Study case over Kreis 2 in Zurich

The 2 km x 2 km study domain is located in Kreis 2 in Zurich (lower left domain corner at lon = 8.5070 and lat = 47.3345) (see red domain mapped in Fig. 5.3). APEX data is available for this region on 30 August 2013 between 11:24 and 11:30 UTC for the APEX stripe 1. A highway crosses the domain from North to South and in the center of the domain, a highway branch goes to the West, before entering the Uetliberg tunnel (see detailed map in Fig. 5.5a). The western side of the domain is dominated by forest.

GRAMM-GRAL simulations for Kreis 2 in Zurich

To compute total AMFs and simulate SCDs measured by an airborne spectrometer, a simulated 3D NO_2 concentration distribution is required. As introduced previously, we use the GRAMM-GRAL dispersion model. Here the model was run over Zurich (see dashed line in Fig. 5.3). The model was driven by a wind speed of 1.50 m/s, a direction of 7°, and a stability class 1 (i.e., Pasquill-Gifford (P-G) stability category A), which corresponds to extremely unstable conditions. The stability class was defined based on wind speed and solar radiation following the recommendations of the GRAL model (see GRAL recommendations at https://github.com/GralDispersionModel/GRALRecommendations, last access: 24 March 2022). The wind situation was chosen according to wind measurements at the Zurich airport in Kloten (located about 12 km NNE of the study domain center) at the time of the APEX flight.

APEX δSCDs and simulated SCDs in Kreis 2 in Zurich

First, we want to qualitatively compare the APEX δSCDs with SCDs calculated combining 3D-box or 1D-layer AMFs with a NO_2 distribution obtained from the GRAMM-GRAL simulation. The APEX δSCD is defined as:

$$\delta SCD = SCD - VCD_r \cdot AMF_r = SCD - SCD_r, \tag{5.1}$$

where VCD_r, AMF_r, and SCD_r are the VCD, AMF, and SCD at a background pixel located far from NO_2 emissions. As a further analysis, we investigate the difference between the SCDs calculated with the 3D-box AMFs and SCDs computed with 1D-layer AMF.

Total AMFs and APEX VCDs

To retrieve VCDs from the available APEX δSCD product, we use the following formula:

$$VCD = \frac{\delta SCD + VCD_r \cdot AMF_r}{AMF}, \tag{5.2}$$

where VCD_r and AMF_r are the VCD and the AMF at the reference background pixel, respectively. Here, we assume a VCD_r = 100 $\mu mol m^{-2}$ and an AMF_r = 1.2. The AMF (i.e., total AMF) is obtained according to the Eq. 2.4 and Eq. 2.5 in Chap. 2.

For clarity in the following paragraphs, we will refer to total AMFs calculated with 3D-box AMF and 1D-layer AMF modules as AMF_{3D} and AMF_{1D}, respectively. Similarly, we will refer to SCDs and VCDs calculated with 3D-box AMF and 1D-layer AMF modules as SCD_{3D}, VCD_{3D}, SCD_{1D} and VCD_{1D}, respectively.

5.2.3 Near surface concentrations in Zurich

Ground NO_2 monitoring stations

In this study, we use NO_2 concentrations measured at air pollution monitoring sites maintained by the Zurich city environment authority, UGZ, the regional monitoring network for eastern Switzerland, OSTLUFT, and the Swiss national air pollution monitoring network, NABEL. The station air inlet is, according to standards, located at about 4 m above ground level, and the measured NO_2 concentrations are averaged hourly in our case.

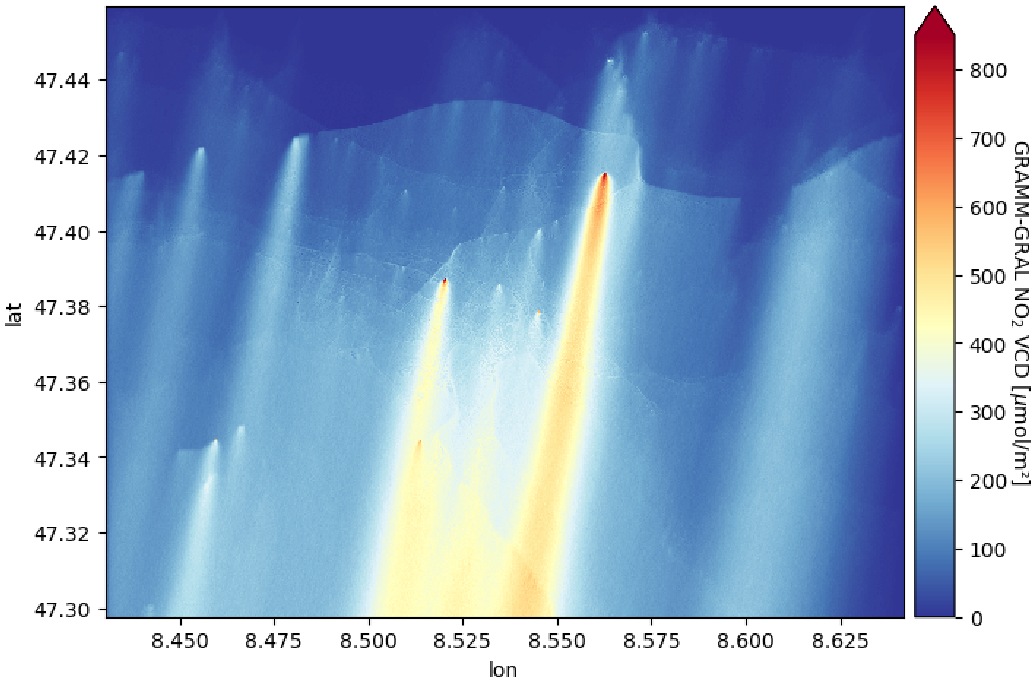

Figure 5.4 – VCDs from the 3D NO_2 concentration distribution computed with the GRAMM-GRAL model on 7 June 2013.

GRAMM-GRAL simulation over a large Zurich domain

The NO_2 distribution was simulated with the GRAMM-GRAL model described previously for a 16 km x 18 km domain centered in Zurich (lower left corner at lon = 8.4303, lat = 47.2977). The model was run without topography and for a wind situation measured at the weather station at the Zurich Airport in Kloten, at the times of the APEX stripes (see an example of GRAMM-GRAL VCDs for the 2013 APEX stripes in Fig. 5.4).

APEX VCDs and near surface concentrations

First, we simulated the total AMFs (AMF_{1D} and AMF_{3D}) according to Eq. 2.4 and Eq. 2.5 for pixels located at a ground air pollution monitoring stations. Second, we simulate the APEX VCDs for the same pixels with Eq. 5.2. Finally, we calculate the near-surface NO_2 concentrations (NSC), using the following equation:

$$NSC = \frac{f}{L_0} \frac{SCD}{AMF}, \tag{5.3}$$

where L_0 is the height of the lowest model layer and f is the ratio of VCD in the lowest layer to the total VCD above the observed ground pixel given as:

$$f = \frac{VCD_{0,init}}{VCD_{init}}. \tag{5.4}$$

Near-surface NO_2 concentrations depend on the simulated NO_2 profile above the observed pixel, which depends on the NO_X emissions from the emission inventories, wind speed and vertical atmospheric mixing, and NO_X advection from surroundings areas.

5.3 Results

5.3.1 APEX study in Kreis 2 in Zurich

APEX δSCDs and simulated SCDs

We present δSCDs retrieved from an APEX airborne spectrometer stripe on 30 August 2013 for a region (Kreis 2) in the city of Zurich and qualitatively compare them with SCDs simulated for the airborne spectrometer using the newly developed radiative transfer modules. The SCDs were simulated using the traditional 1D-layer AMFs and the 3D-box AMFs including buildings.

Figure 5.5a and b show the location of the study area and the δSCDs retrieved from the APEX measurement, respectively. The δSCDs are difficult to interpret as they strongly depend on the ground reflectance, but the spatial pattern of the highway (Autobahn A3) (see location in pink in Fig. 5.5a) is visible with increased values (see Fig. 5.5b). Other individual roads or plumes are hardly observable, as they appear smeared.

To simulate the SCDs with the 3D-box AMF and 1D-layer AMF modules (respectively SCD_{3D} and SCD_{1D}), a distribution of NO_2 is required and was simulated with the GRAMM-GRAL model (see VCDs from the GRAMM-GRAL 3D NO_2 concentration distribution in Fig. 5.5d). SCD_{3D} and SCD_{1D} (see respective Figs. 5.5c and e) were simulated based on the numerators in Eq. 2.5 and Eq. 2.4 similarly to SCDs simulated in Chap. 4 (e.g., SCDs in Figs. 4.6d, e, and f). Finally, we plot the relative difference between SCD_{1D} and SCD_{3D} in Fig. 5.5f.

SCD_{1D} values are higher than SCD_{3D} over emission plumes and roads (e.g., strong emission at the highway junction at 47.345°N and 8.520°E). The high values from the GRAMM-GRAL simulations are slightly smeared using 3D-box AMFs (see Fig. 5.5c), which is consistent with the findings from the previous chapters (Chap. 3 and 4). Furthermore, SCDs in regions with buildings show higher values with the 1D-layer AMFs. 1D-layer AMFs do not include buildings, but the simulated NO_2, used for the total AMF calculation, includes buildings. In fact, the GRAL model accounts for the presence of buildings in the high-resolution wind field simulations. The 5 m x 5 m NO_2 GRAMM-GRAL output field is averaged to the 50 m x 50 m APEX pixel. By doing so, the amount of NO_2 contained in an APEX grid cell reflects the reality. Higher SCD_{1D} over buildings is consistent with the conclusions in Chap. 4, where we showed that including

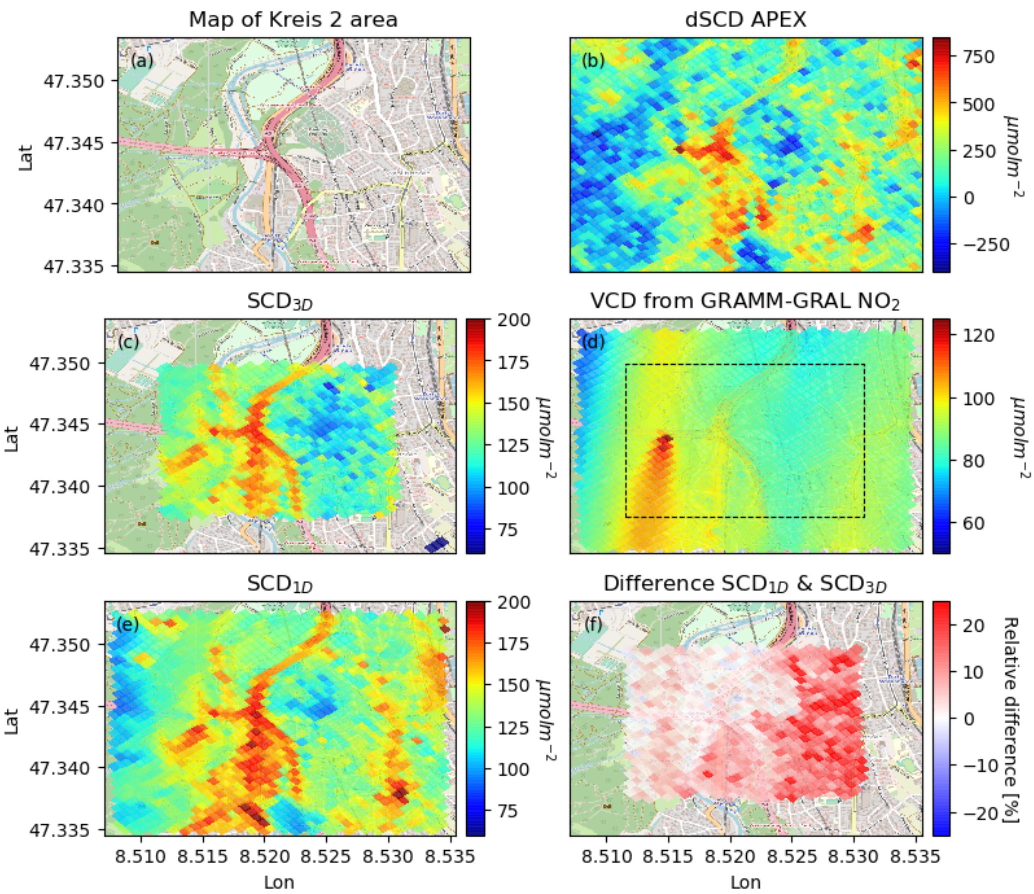

Figure 5.5 – (a) Map of study location: Kreis 2 in Zurich, (b) APEX δSCDs, SCDs calculated with (c) 3D-box AMFs with buildings and (e) 1D-layer AMFs combined with NO_2 distributions from GRAMM-GRAL simulations, (d) VCDs from the GRAMM-GRAL 3D NO_2 distribution and the extent of the SCD_{3D} domain as a black dashed square, and (f) difference between SCD_{1D} and SCD_{3D}. During this APEX stripe, the sun was in the S with a SZA = 38.5°. Map informations were obtained from OpenStreetMap (© OpenStreetMap contributors 2022. Distributed under the Open Data Commons Open Database License (ODbL) v1.0.)

buildings leads to a decrease in the instrument sensitivity to close-to-ground NO_2. Notice that the APEX reflectance product, which we used to represent the reflectance of roofs and ground-level surfaces might already carry information about building shadows and could potentially lead to an overcompensation of buildings effects when used together with the 3D-box AMFs module with buildings.

Finally, if the calculated SCDs are qualitatively compared to δSCDs from the APEX stripe (i.e., Figs. 5.5c or e compared to Fig. 5.5b), the spatially smeared pattern of high SCDs (e.g., over roads) of the δSCDs seems to be better represented with SCD_{3D}. A quantitative comparison between the measured δSCDs and the calculated SCDs remains very challenging for several reasons. First, the uncertainty in the δSCDs is relatively large (around 20 μmol/m^2). In addition, the GRAMM-GRAL simulations used as NO_2 distributions are not perfectly suited yet to compute very realistic SCDs. For example, the topography was ignored in these simulations, as the model showed some instability when including topography. The western side of the domain is mountainous and slightly NE of the domain center, a hill is present. The GRAL flow field does not account for wind channeling due to these topographic features and the simulated NO_2 field used in the SCD simulations is therewith affected. Another potential bias is introduced by the emission inventory, which is based on annually averaged emissions. NO_2 emissions at noon-time of a weekday are expected to be higher than the annual averaged emissions, as the traffic and the industrial activities are intense during day time.

Total AMFs and APEX VCDs

In Figs. 5.6b and d, we show the total AMFs for the selected domain calculated with 3D-box AMFs including buildings and with the 1D-layer AMFs, respectively (i.e., AMF_{3D} and AMF_{1D}). Figures 5.6a and c illustrate the APEX VCDs obtained from the δSCDs and the AMF_{3D} and AMF_{1D}, respectively (i.e., VCD_{3D} and VCD_{1D}). Figure 5.6e illustrates the relative difference between VCD_{1D} and VCD_{3D}. Finally, we present the VCDs calculated from the GRAMM-GRAL 3D NO_2 distribution in Fig. 5.6f.

First, the AMF_{3D} and VCD_{3D} domains are 200 m shorter in each direction. The input data was cropped to the study domain and the MYSTIC 450 m-wide domain can only compute 3D-box AMF where the input data are present. Therefore 3D-box AMF were not computed for pixels close to the study domain boundaries.

The obtained VCDs are noisy (see Figs. 5.6a and c), which is manly induced by random uncertainties in the APEX δSCD product (see APEX δSCD in Fig. 5.5b). The noise in the APEX δSCD product can potentially come from the measurement, the calibration, or from the DOAS retrieval.

Similarly to the previous studies, we notice that AMF_{1D} are highest over high NO_2 concentration (e.g., directly over the highway), whereas AMF_{3D} seem to be smeared horizontally. The AMF_{3D} seems to decrease the sensitivity (smear the signal) of the instrument and hence increase NO_2 VCDs over high concentrations (i.e., correct for the smeared SCDs)(see highway junction at 47.345°N and 8.520°E in Fig. 5.6a). This has been extensively discussed in the previous section and in Chaps. 3 and 4.

With this example, we demonstrate that we successfully implemented the 3D-box AMF RT module into the Empa APEX NO_2 retrieval algorithm and that we are now able to retrieve VCD_{3D} from airborne spectrometer measurements. Regarding the number and the complexity of the required input data, the VCD_{3D} map shows reasonable features.

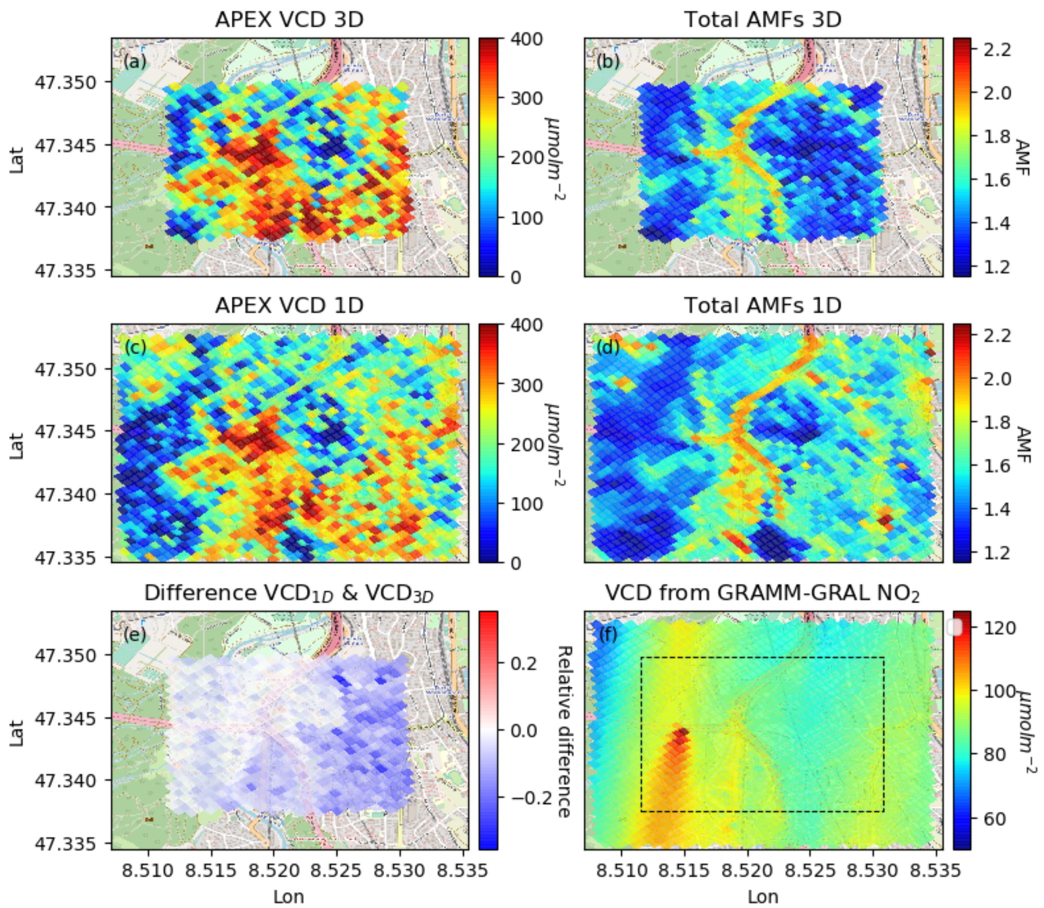

Figure 5.6 – (a) APEX VCDs calculated with AMF$_{3D}$, (b) AMF$_{3D}$ obtained with 3D-box AMFs and GRAMM-GRAL 3D NO_2 distribution, (c) APEX VCD calculated with AMF$_{1D}$, (d) AMF$_{3D}$ obtained with 3D-box AMFs and GRAMM-GRAL 3D NO_2 distribution, (e) Relative difference between VCD$_{1D}$ and VCD$_{3D}$ and (f) VCDs from the GRAMM-GRAL NO_2 distribution and the extent of the VCD$_{3D}$ domain as a dashed black square. Map informations were obtained from OpenStreetMap (© OpenStreetMap contributors 2022. Distributed under the Open Data Commons Open Database License (ODbL) v1.0.)

5.3.2 Near surface concentrations in Zurich

The APEX near-surface NO_2 concentrations obtained with 3D-box AMFs at the location of monitoring stations are presented in Fig. 5.7 for the APEX 2010 morning flight. Similar figures for the APEX 2010 afternoon, the 2013, and the 2016 flights are presented in Appendix D.2.

A direct comparison between APEX near-surface NO_2 concentrations and NO_2 concentration measured at air pollution monitoring stations is very challenging. For example, for the 2010 morning campaign (Fig. 5.7), we observe a certain correlation (r = 0.74 for near-surface NO_2 concentrations calculated with 3D-box AMFs and 8 compared points) between the two

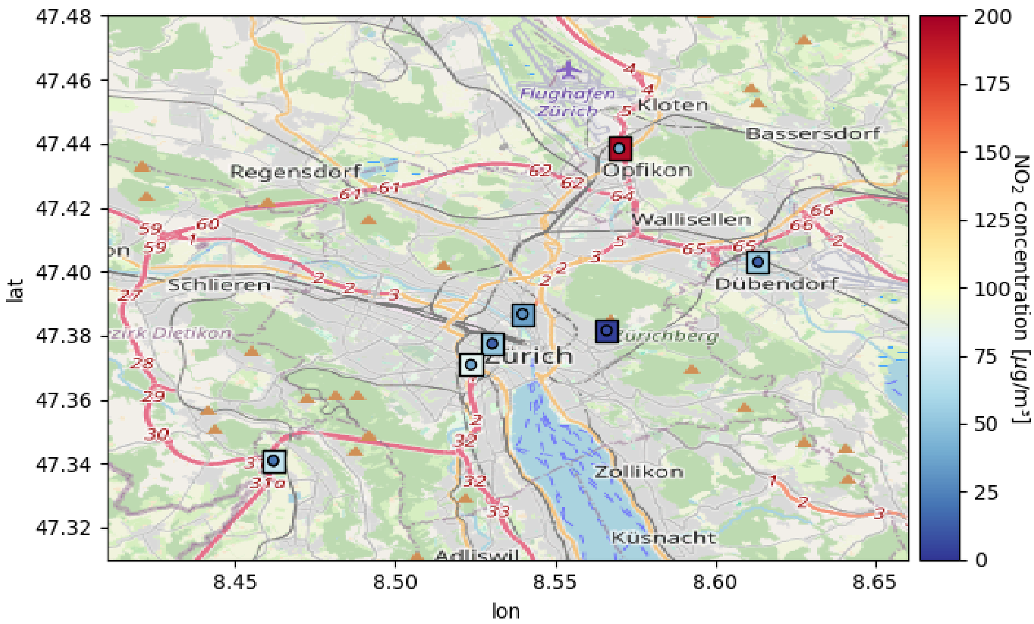

Figure 5.7 – Near surface concentrations from APEX (APEX 2010 morning campaign), retrieved with the 3D-box AMFs (square) and ground measurement concentrations at the location of ground air pollution monitoring stations (circle). Map informations were obtained from OpenStreetMap (© OpenStreetMap contributors 2022. Distributed under the Open Data Commons Open Database License (ODbL) v1.0.)

quantities, as they seem to be lower in remote areas and both show increased values close to NO_2 sources. Near heavy traffic (e.g., the Opfikon station located NE of the map center), the two quantities seem to differ significantly. Differences between the two quantities can be explained by many factors that are challenging to disentangle. First, the uncertainty in the APEX δSCD product is relatively large (around 20 μmol/m^2) and most certainly dominating the total uncertainty in the VCD and near-surface NO_2 concentration products (see APEX uncertainty section 3.3.2 in Kuhlmann et al., 2022). Second, the APEX near-surface NO_2 concentration product depends on the simulated NO_2 distribution (i.e., its relative distribution), we obtained with the GRAMM-GRAL model. This distribution is strongly influenced by the wind speed and direction, by the atmospheric mixing, and by the topography (ignored in these simulations). Other sources of errors as the uncertainty in the emission inventories might also influence the a priori 3D NO_2 distribution. Third, the AMF calculation depends on input parameters obtained from the APEX product (e.g., the reflectance) that also contribute to the total uncertainty. Additionally, the assumption for the buildings wall reflectances might not be representative for the entire city. Those described uncertainties would need to be assessed and studied in more details for a more in-depth comparison. Furthermore, the APEX near-surface NO_2 concentrations represent an averaged NO_2 concentration for the ground pixel, whereas the monitoring stations gives an hourly averaged NO_2 concentration at one

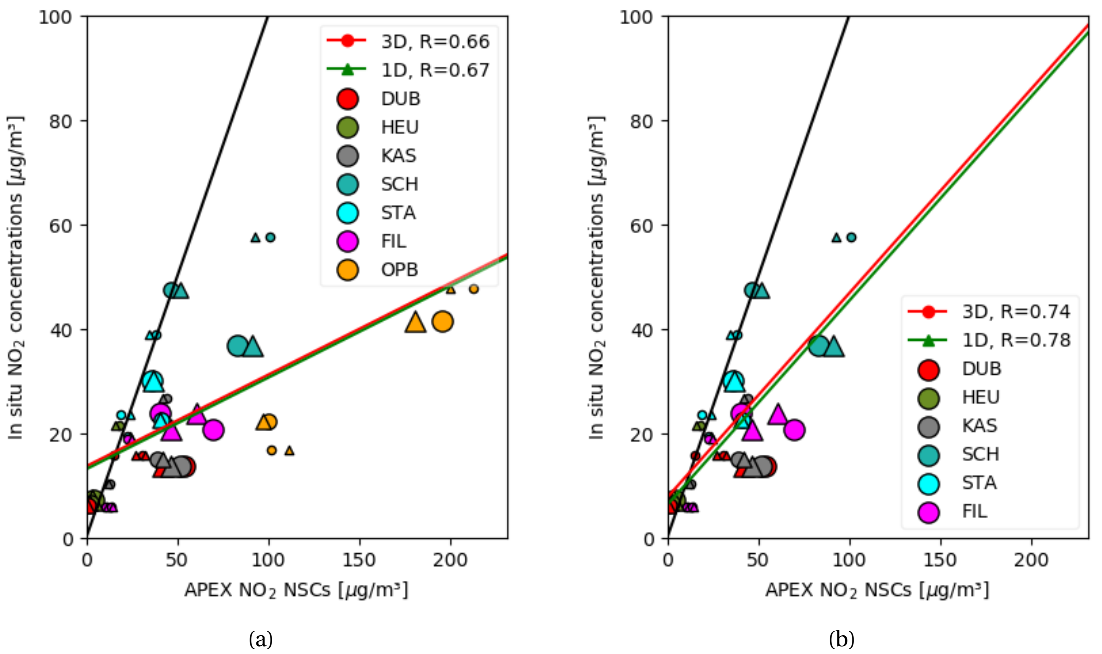

Figure 5.8 – Scatter plot between APEX NO_2 near surface concentrations retrieved with 1D-layer AMFs (triangles) and 3D-box AMFs (circles) and surface in-situ NO_2 concentrations for (a) all stations and (b) excluding OPB. The small, medium, and large symbols size represents the 2010, 2013, and 2016 campaign, respectively. The 1:1 line is plotted in black and the fitted line to the (a) 28 and (b) 24 comparison points in red and green for 3D and 1D AMFs, respectively.

specific location. The latter is sensitive to NO_2 advected by the wind during the averaging hour. The concentration footprint of this point measurement would be located upwind. For example, if the monitoring station is located close, but upwind to a strong source, it could miss the high concentration as the footprint would be locate in the opposite direction, whereas the strong source could be potentially captured by the APEX measurement.

The comparison between all APEX near-surface NO_2 concentrations and the ground NO_2 concentrations measured by ground measurement stations during the different flights is shown as a scatter plot in Fig. 5.8a. The APEX near-surface NO_2 concentrations are in moderate agreement with in-situ measurements at ground air pollution monitoring stations as they co-fluctuate with a correlation coefficients $r = 0.66$ for 3D and $r = 0.67$ for 1D (slope and offset of the fitted lines are 0.18 and 13.64 for 3D and 0.19 and 13.09 for 1D, respectively). When excluding the OPB measurement station (see Fig. 5.8b), a measurement that seems to be considerably different to the APEX near-surface NO_2 concentration, the quantities are in reasonably good agreement as they co-fluctuate with a correlation coefficients $r = 0.74$ for 3D and $r = 0.78$ for 1D (the slope and offset of the fitted lines are 0.39 and 7.68 for 3D and 0.43 and 6.23 for 1D, respectively). For this monitoring station in Opfikon, the differences may be attributed to multiple factors. First, the measurement station is located on the eastern side of the highway 51 and at the time of the measurement(s), the wind was from NNE. The footprint of the hourly-averaged concentration measured at the monitoring station could be partly located aside the high way, whereas the APEX pixel covers the highway. Second, the assumption of horizontal homogeneity of optical properties in a box in the 3D-box AMF calculation is likely broken, as we expect the surface reflectances and the 3D NO_2 distribution to be highly inhomogeneous in a 50 m x 50 m pixel over a highway. Third, the APEX column measurement potentially overlaps with the axis of the take-off runway 16 from the Zurich Airport, where emissions from planes could affect the APEX measurement. Other sources of uncertainties such as the NO_2 field from the GRAMM-GRAL model could also contribute to explain the observed differences between the two quantities as discussed in the previous paragraph.

Considering the complexity of such retrievals and the numerous uncertainties affecting the total uncertainty we can conclude that it is possible to retrieve VCDs and near-surface NO_2 concentrations from APEX measurements. In the considered examples, a strong impact of 3D and buildings on the retrieved products (e.g., VCDs and near-surface NO_2 concentrations) was not observed. The errors discussed above seem to be larger than the 3D RT effects and building effects as the near-surface NO_2 concentrations calculated with 3D-box AMFs shows similar correlation coefficient as the near-surface NO_2 concentrations calculated with 1D-layer AMFs. To start disentangling the sources of errors, instruments dedicated to NO_2 remote sensing, with lower uncertainty in the δSCD product and better a priori NO_2 distributions, are required. A study with such an instrument, e.g., the Spectrolite Breadboard Instrument (SBI) (de Goeij et al., 2017; Vlemmix et al., 2017) would be a relevant follow-up of the research presented in this chapter.

5.4 Conclusions

In Chap. 3 and Chap. 4 we demonstrated that 3D radiative effects can affect airborne spectroscopy trace gas retrievals. With the help of numerous synthetic, but realistic examples, we studied the effect of 3D-photon path and the presence of buildings on the instrument sensitivity and, therefore, on the retrieved trace gas concentration. In this chapter, to support the conclusions of these studies, we implemented the developed radiative transfer modules in the Empa APEX NO_2 retrieval algorithm.

In a first case study located in the Kreis 2 region in Zurich, we simulated SCDs, the APEX instrument would measure, using the APEX flight data and qualitatively compared them to the APEX δSCD product. The two quantities correlate partially ($r > 0.64$) with low values in the background and increased values over NO_2 sources (i.e., roads). Since the SCD values strongly depend on the surface reflectance, it is challenging to draw general conclusion from these maps. The SCD_{3D} and SCD_{1D} show similar patterns but with pronounced differences close to sources, which we discussed in the previous chapters as the horizontal smearing (see Chap. 3 and 4). We then computed the APEX VCDs for the same APEX stripe and demonstrated that the developed RT features can be applied to retrieve trace gases from airborne spectroscopy.

Finally we computed the APEX near-surface NO_2 concentrations and compared them to NO_2 concentrations measured at ground air pollution monitoring stations operating at the time of the APEX flights. We show that the APEX near-surface NO_2 concentrations are in reasonably good agreement with in-situ measurements at ground air pollution monitoring stations as the correlation coefficients of the compared points are relatively high with r = 0.74 for near-surface NO_2 concentrations calculated with 3D-box AMFs and r = 0.78 for near-surface NO_2 concentrations calculated with 1D-layer AMFs, when excluding one station (OPB) where substantial differences were observed. The comparison between the near-surface NO_2 concentrations and in situ measurements is challenging and no improvement in near-surface NO_2 concentrations calculated with 3D-box AMFs compared to near-surface NO_2 concentrations calculated with 1D-layer AMFs was observed. The quality of the APEX δSCD product strongly limits the retrieval quality. Additionally, uncertainty in the numerous required input data can limit the performance of such a retrieval.

The APEX instrument was not primarily designed to retrieve trace concentrations and the retrieved δSCDs are relatively noisy. We would be interested in applying the developed radiative transfer modules to airborne spectrometers designed for trace gas retrievals with better quality in the retrieved trace gas columns. We expect the 3D radiative transfer and buildings to become more relevant for those measurements as it was demonstrated for synthetic case studies in previous studies by Schwaerzel et al. (2020, 2021). In the future, the quality of the required RT input data can be improved, as e.g., the simulated NO_2 field from the GRAMM-GRAL model. The model could be run with topography, which would locally improve the assumed NO_2 distribution. In the study, we used a single constant aerosol setting for the AMF calculation, which could be improved, with e.g., aerosol profile measurements during the airborne spectrometer flights or with aerosol simulations with the GRAMM-GRAL model. However, the latter point would imply a complex conversion from the reported PM10 concentration to aerosol optical properties. Additionally, most of the APEX campaigns were conducted in the late morning or in the afternoon, times when the atmospheric turbulent mixing from convection has already began and when the spatial variability in NO_2 is expected to be smoothed out. We would recommend early morning flight with the consideration that 3D RT effects might be particularly relevant (high solar zenith angle). A very interesting follow-up study would be to compare the VCD_{3D} maps to NO_2 VCDs obtained with other mapping techniques.

Acknowledgment – We want to thank Andreas Hueni and colleagues from the Department of Geography at the University of Zurich for preparing and processing the APEX raw data. We also want to thank Christoph Hüglin and Jörg Sintermann for the ground measurement data, we accessed at the OSTLUFT website (https://www.ostluft.ch/index.php?id=52, last access 14 January 2022). We thank the city of Zurich for providing the NO_X emission inventory, needed for the GRAMM-GRAL simulations. Finally, we want to acknowledge the Swiss Federal Office of Topography (swisstopo) for providing the 3D building data.

6 Conclusions

Airborne imaging spectrometers are increasingly used for high-resolution mapping of NO_2 concentrations in cities. The NO_2 maps obtained in this way are usually rather smooth and seemingly inconsistent with the much more strongly varying near-surface NO_2 concentration fields observed in city-scale dispersion model simulations, for example. The differences may partly be explained by atmospheric mixing more strongly affecting total columns than the near-surface concentrations, but could also be caused by complex 3D radiative transfer effects in cities. Traditional trace gas retrievals (i.e., their RT calculations) assume horizontal homogeneity of ground and atmospheric absorbing and scattering properties, which might not be valid over cities, where trace gas distribution and ground optical properties are highly inhomogeneous. The impact of these 3D RT effects on the retrieved trace gas concentrations needs to be studied. In this PhD thesis, I studied the importance of 3D radiative transfer effects for a range of trace gas remote sensing applications such as ground-based MAX-DOAS and airborne imaging spectroscopy.

To study these effects, 1D-layer AMFs and 3D-box AMFs modules were implemented in MYSTIC, a Monte Carlo solver of the libRadtran RTM. The computation of AMFs is a central component in most trace gas retrieval algorithms to convert observed SCDs into VCDs, but so far these algorithms were limited to 1D RT simulations. The MYSTIC 1D-layer and 3D-box AMFs modules agree very well with 1D-layer AMFs calculated with other RTMs presented in a previous model intercomparison study by Wagner et al. (2007). Furthermore, I implemented an urban canopy module (i.e., complex surfaces such as buildings) into MYSTIC. Finally, I implemented the developed 3D RT modules in the Empa APEX NO_2 retrieval algorithm.

In a first application with a ground based MAX-DOAS instrument, I showed that 3D-box AMFs are highest along the line of sight of the instrument (representing photons that have mostly scattered only once), but that the contribution from outside is not negligible and depends on sun position, the instrument measurement geometry and aerosol optical depth. The spatial distribution of the vertically integrated 3D-box AMFs in the boundary layer (i.e., the close to ground sensitivity of the instrument) depends on the sun position, which is important for interpreting MAX-DOAS observations, especially in urban areas or, more generally, in the vicinity of pollution sources. As a result, the spatial variability of the NO_2 distribution in the context of the MAX-DOAS instrument can affect the retrieval differently at different times of the day.

As a second application, airborne spectrometer trace gas retrievals were studied using simulations of a NO_2 plume emitted by a stack (e.g., from a refinery). I showed that when using 1D-layer AMFs, the NO_2 VCDs in the plume are significantly underestimated and that the position of the plume is artificially shifted towards the aircraft. Furthermore, integrals of the NO_2 enhancement in across-plume direction (line densities) are also biased, which results in an underestimation of the NO_2 emissions from the stack when using a mass-balance approach. Using 1D-layer AMFs induces systematic errors even if the NO_2 profile above the ground pixels is known accurately, because a 1D RTM fails to properly represent the complex light path, which is required if the trace gas field is not horizontally homogeneous.

As a third application, I set up a case study for an airborne spectrometer flying over a 1 km x 1 km domain in Zurich, for which 3D-box AMFs and NO_2 slant column densities were computed for a realistic field of NO_2 concentrations. In this case study I showed that the footprint of a single observation is only partly located over the observed ground pixel and that if the sun is not located in the zenith, a sensitivity 'tail' in the direction of the main optical path is observed. Furthermore, an important part of the sensitivity is located outside the ground pixel for a nearly-nadir viewing instrument. A smaller part of the sensitivity is located outside the main optical path because of atmospheric scattering, but this part increases with aerosols and buildings. The spatial structure of the sensitivity is modified by the presence of buildings, but the sensitivity is still well represented by the main optical path, at least for small buildings. The 3D radiative transfer simulations show that 3D effects introduce significant spatial smearing of high NO_2 concentrations (e.g., over roads). When buildings are included, NO_2 SCDs are generally lower due to the light shielding effect of buildings. The buildings also introduce an additional noise component to measure NO_2 from airborne imagers. However, the magnitude is slightly smaller than the current δSCD uncertainty (about 20 $\mu mol\, m^{-2}$ for the APEX instrument), but could be noticeable for instruments dedicated to NO_2 mapping that have lower SCD uncertainties.

Finally, I applied the developed RT models to real APEX measurements. I showed NO_2 VCD maps retrieved from an APEX measurement campaign over Zurich. I demonstrate that despite the complexity and the number of required input data, 3D-box AMFs including buildings can be used to retrieve APEX airborne spectroscopy NO_2 VCDs. Finally, I retrieved APEX near-surface NO_2 concentrations for 4 different measurement campaigns over Zurich at the locations of 7 ground air pollution monitoring stations. I compared the APEX near-surface NO_2 concentrations with NO_2 concentrations measured at the air pollution monitoring stations at the time of the flights. The two quantities showed positive correlation coefficients (e.g., $r = 0.66$ for near-surface NO_2 concentrations calculated with 3D-box AMFs), but the APEX near-surface NO_2 concentrations seem to be positively biased, which needs to be further investigated. The APEX instrument was not primarily designed to retrieve trace concentration and the retrieved δSCDs are relatively noisy. Due to the many sources of uncertainty, I was unable to demonstrate that 3D RT was significantly beneficial for the estimation of near-surface NO_2. I would appreciate to apply the developed RT modules to airborne spectrometers designed for trace gas retrievals with better quality in the retrieved trace gas columns (e.g., the SBI instrument) and to retrieval VCDs and near-surface NO_2 concentrations using better suited a priori NO_2 distributions. I expect the effects of 3D radiative transfer and buildings to become more relevant for those measurements as it was demonstrated for the synthetic studies.

In conclusion, our synthetic case studies demonstrate the importance of 3D radiative transfer effect and the effect of buildings on trace gas remote sensing from ground and airborne spectrometers. 3D light path induces a horizontal smearing of the retrieved NO_2, which can not be corrected with retrievals using the traditional 1D-layer AMFs. The studies also showed that building shading effects induce underestimation and add a noise component in NO_2 columns retrieved from airborne spectrometers. I showed that the developed RT modules can be applied to real airborne spectroscopy data, but that the effects described in the synthetic studies were not observed, because of the high uncertainty in the APEX δSCD product and other required input data. Therefore, instruments dedicated to trace gas retrievals with lower noise in the data are required. Generally more studies disentangling the impact of the different parameters affecting the NO_2 retrieval are necessary (i.e., assessing the total uncertainty in the VCDs and near-surface NO_2 concentrations). Since 3D radiative transfer calculations are computationally expensive, efficient methods need to be developed for operational applications that provide an appropriate balance between accuracy and computational cost.

The implementation of the 3D box-AMF module in the MYSTIC solver of the libRadtran radiative transfer model is essential for retrieving and analyzing NO_2 remote sensing data over cities. These changes in the libRadtran RTM (i.e., its MYSTIC RT solver) will improve the quality of the ground-based and airborne spectroscopy retrieval product by reducing systematic errors and by allowing a better spatial allocation of the measurements. These implementations will be of general interest for the remote sensing community working increasingly with high-resolution observations over cities and other complex environments (e.g., Tack et al., 2017). In addition, 3D RT has recently been used to study the impact of clouds on trace gas concentration retrievals (Emde et al., 2022; Yu et al., 2021; Kylling et al., 2021). Furthermore, an improvement in airborne spectroscopy retrievals can provide better maps and validate other mapping techniques such as urban-scale pollutant dispersion models. Applying 3D RT with buildings to NO_2 retrievals for MAX-DOAS instruments could potentially allow this measurement technique to measure NO_2 in urban canyons. 3D effects are also important for tomographic inversion (e.g., Frins et al., 2006; Kazahaya et al., 2008; Casaballe et al., 2020) where the application of 3D-box AMFs will minimise errors caused by the use of pure geometric assumptions. The developed modules could be applied to trace gas retrievals from satellites, high-altitude platforms or instruments placed on drones.

The 3D radiative transfer effects can affect the retrievals of other trace gases such as SO_2 or BrO more significantly, as these trace gases are retrieved at lower wavelength, where more atmospheric scattering is expected. The instrument footprint is expected to be larger at those wavelengths and the instruments are expected to be more sensitive to regions aside the main optical path. Likewise, retrievals over polluted cities with high aerosol loads that increase atmospheric scattering can benefit from 3D radiative transfer.

On the long term, improved trace gas retrievals described in the work could be applied to future trace gas measurement from instruments with increased spatial resolution to obtain high-resolution NO_2 maps. More generally, maps obtained in this way can support authorities to validate emission inventories or support urban planning. They can help identifying pollution hot spots and contribute to design efficient measures to reduce the exposure of the population to air pollution and improve human health.

7 Outlook

These following general and technical points and suggestions have arisen during the completion of this project. Ideally, a follow-up study should consider the suggested points to further improve the developed concepts.

High resolution imaging remote sensing can be a valuable addition to air pollution and emission monitoring for city and state authorities. On one hand to monitor air pollution and assess the population exposure and on the other hand to verify the reported emissions in the emission inventories. But, air pollution maps from airborne measurement campaigns might not be an ideal solution, as they only present a snap-shot in time. Ideally, long-term continuous trace gas monitoring could be considered by local authorities, with the development of e.g., High-Altitude Pseudo-Satellite, for which 3D RT would be a critical component.

3D radiative transfer calculations in the urban canopy could also be applied to MAX-DOAS measurements to include measurement near the surface and include the relevant close-to-ground concentrations. A better knowledge of the instrument spatial sensitivity could also improve the understanding of the spatial distribution of the measured NO_2 for this type of measurements.

The implementation of the urban canopy into the MYSTIC solver of the libRadtran radiative transfer model might be improved as follows. For now, the reflection of a photon on the triangular grid is implemented as a Lambertian reflection, which might not be accurate in modern city-centers, with glass or metallic surface, where the reflection might be better simulated with a specular reflection. Ideally, reflection should be treated with a bidirectional reflectance distribution function (BRDF) to best represent real surfaces. BRDF is implemented in MYSTIC for some RT quantities, but the required input data would be extremely complicated to obtain for a remote sensing application in cities.

In this work the topography withing the MYSTIC domain was not considered in individual AMF calculations. The natural topography in cities such as Zurich in Switzerland might modify the sensitivity distribution of the instrument. This latter point was not addressed, but would be technically straight forward to implement in the developed urban canopy module. Therefore, it is highly recommended to conduct an AMF sensitivity study for complex natural topography.

Furthermore, the generation of the triangular mesh, from the building shapes could be improved, to better account for courtyards and complex building shapes. A specific sensitivity study would help evaluating the need in improving the function creating the triangular mesh. The reflectance of building walls was assumed to be 0.1 in this study, which might not be realistic for the whole city of Zurich or other cities. For this latter point, a sensitivity study on the reflectance properties of buildings and their impact on AMF calculation is needed.

One critical obstacle in the AMF calculation for trace gas retrieval is the assumed a priori distribution of the studied trace gas. In this thesis, I use the GRAMM-GRAL city-scale dispersion model without topography (but with buildings) to overcome this obstacle. In the future, the model will be run with the full topography, which will hopefully improve the retrieval. I would also be eager to compare the used distribution with real measurements of NO_2. An APEX campaign over Munich, where ground measurement and profile measurement were simultaneously conducted, was recently summarized in Kuhlmann et al. (2022). This study showed vertical distribution of NO_2 obtained from MAX-DOAS instrument and suggested that a comparison with GRAMM-GRAL NO_2 distributions would be highly interesting. Furthermore, the scientific community could highly benefit from NO_2 vertical profiles measurements conducted with an in situ instrument, e.g., placed on a drone for typical high polluted and background regions in a city. More information about the vertical distribution of NO_2 would also improve the near surface concentration product retrieved from airborne spectrometers.

A Appendix to chapter 2

MYSTIC input file example

```
uvspec_path     PATH_TO_UVSPEC_EXE
data_files_path PATH_TO_INPUT_DATA_LIBRADTRAN
atmosphere_file PATH_TO_ATMOSPHERE_COMPOSITION
source solar    PATH_TO_SOLAR_SOURCE
work_dir        PATH_TO_WORK_DIR
wc_file 3D      PATH_TO_CLOUD_GRID
mc_triangular_surface_file PATH_TO_TRIANGLE_NC_FILE
mc_sensorposition 1041.500000 483.500000 5749.000000
mc_boxairmass 3D
wavelength 460.0
albedo 0.050815
rte_solver mystic
sza 25.276394
phi0 -61.956053
mc_vroom off
quiet
aerosol_default
aerosol_modify tau set 0.1
mc_backward
atm_z_grid 0.0000 0.5870 0.5970 0.6070 ...
mc_panorama_view 72.5185 73.0265 9.0577 9.5717
mc_panorama distr_photons_over_pixel
mc_photons 100000
```

B Appendix to chapter 3

B.1 Additional figures

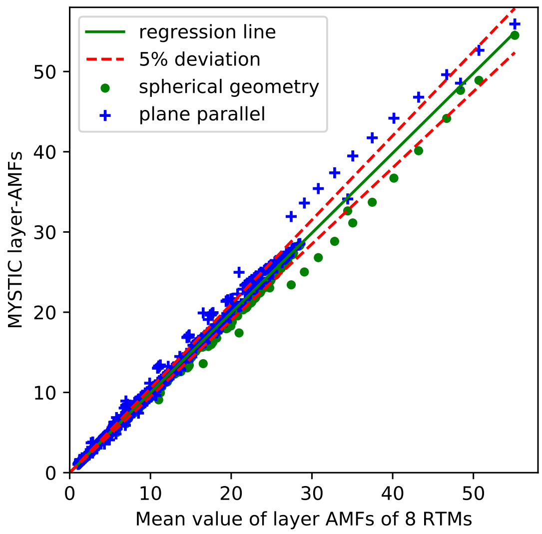

Figure B.1 – Scatter plot of MYSTIC layer AMFs computed with spherical (green dots) and plane parallel geometries (blue dots) against the model mean from Wagner et al. (2007) for 67 scenarios with 17 layers (1139 points). The solid green line is the regression fit to all points of both spherical and plane parallel geometries.

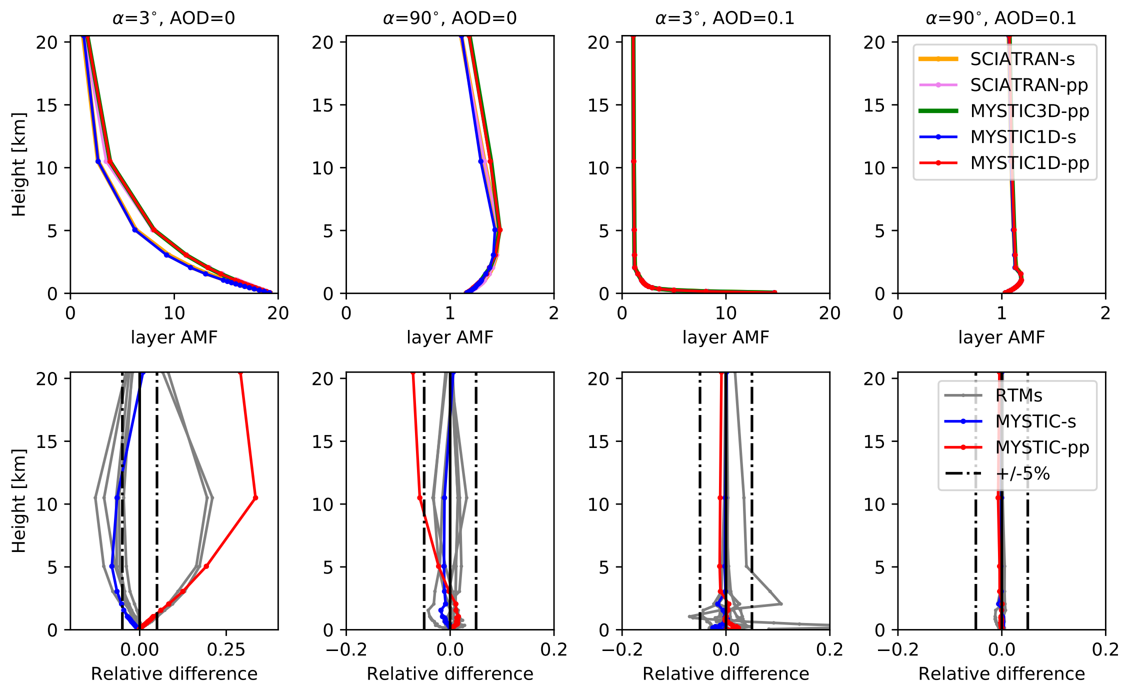

Figure B.2 – Upper row: AMF profiles for MYSTIC 1D spherical geometry (blue), 1D plane parallel geometry (red) and 3D plane parallel geometry (green) for two selected elevation angles of 3° and 90°, a SZA of 20°, with and without aerosol for radiation at 577 nm. Corresponding profiles computed with the SCIATRAN RTM are shown for comparison. Lower row: Profile of relative differences of MYSTIC results in spherical (blue) and plane parallel geometry (red) from the mean AMF profile of Wagner et al. (2007). The relative differences of the individual RMTs used in Wagner et al. (2007) are also shown for comparison.

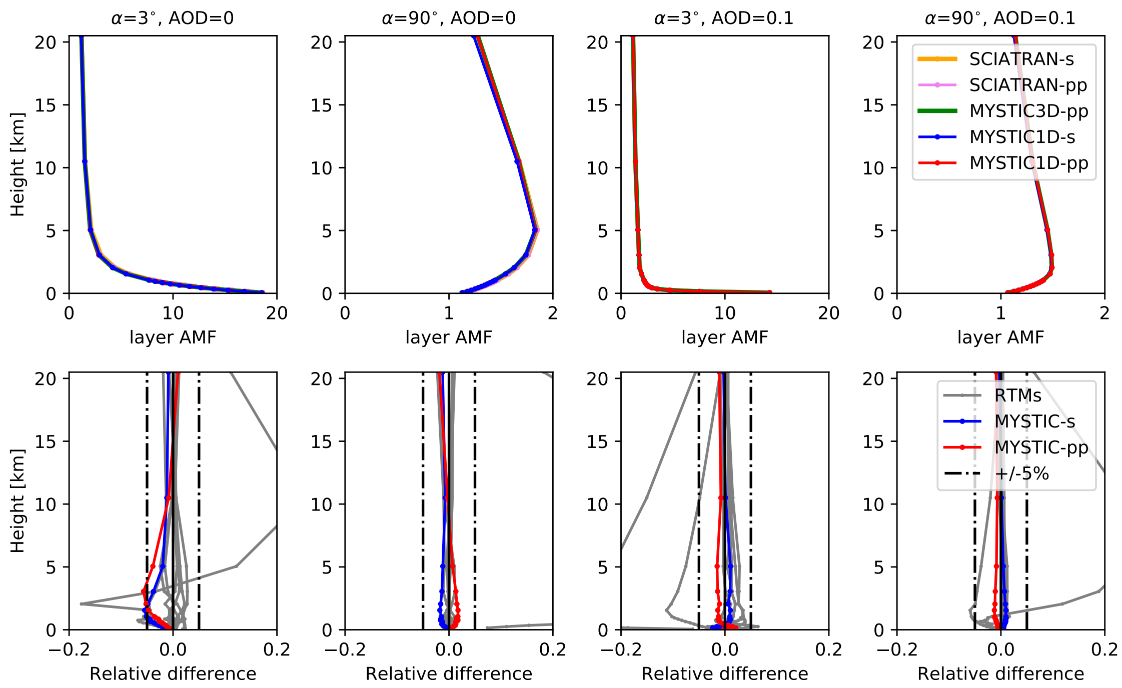

Figure B.3 – Upper row: AMF profiles for MYSTIC 1D spherical geometry (blue), 1D plane parallel geometry (red) and 3D plane parallel geometry (green) for two selected elevation angles of 3° and 90°, a SZA of 20°, with and without aerosol for radiation at 360 nm. Corresponding profiles computed with the SCIATRAN RTM are shown for comparison. Lower row: Profile of relative differences of MYSTIC results in spherical (blue) and plane parallel geometry (red) from the mean AMF profile of Wagner et al. (2007). The relative differences of the individual RMTs used in Wagner et al. (2007) are also shown for comparison.

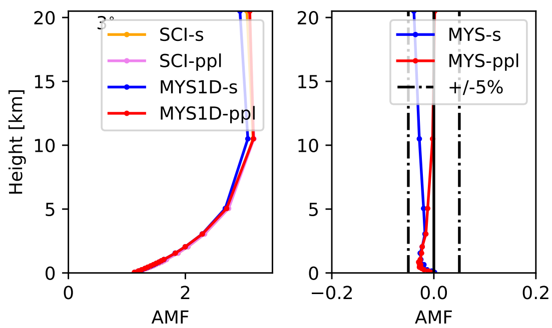

Figure B.4 – Left: AMF profiles for 440 nm for MYSTIC 1D - plane parallel geometry (red), MYSTIC 1D - spherical geometry (blue) SCIATRAN - plane parallel geometry (pink) and SCIATRAN - spherical geometry (orange) for an instrument viewing angle of 90° (zenith view), a solar zenith angle of 70° and without aerosol. Right: AMF relative difference profile for a relative difference of MYSTIC spherical (blue) and plane parallel (red) to SCIATRAN spherical and plane parallel, respectively.

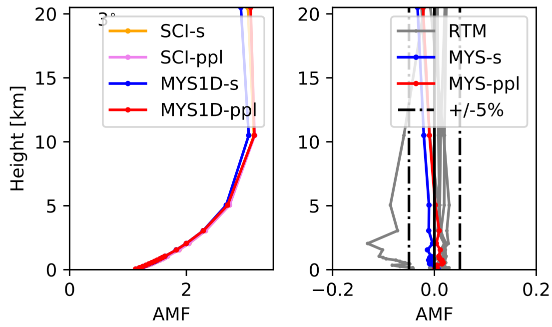

Figure B.5 – Left: AMF profiles for 440 nm for MYSTIC 1D - plane parallel geometry (red), MYSTIC 1D - spherical geometry (blue) SCIATRAN - plane parallel geometry (pink) and SCIATRAN - spherical geometry (orange) for an instrument viewing angle of 90° (zenith view), a solar zenith angle of 70° and without aerosol. Right: AMF relative difference profile for a relative difference of the individual models to the models mean from the models from Wagner et al. (2007).

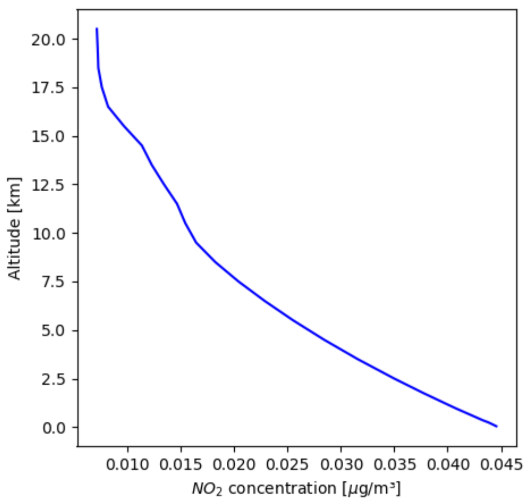

Figure B.6 – NO_2 background profile interpolated from the US standard atmosphere (United States Committee on Extension to the Standard Atmosphere, 1976).

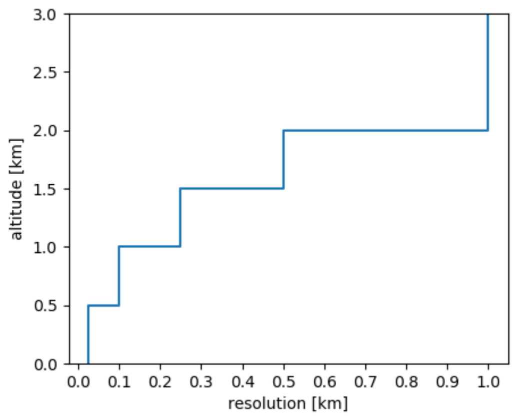

Figure B.7 – MYSTIC vertical resolution for layers between 0 and 3 km. Between 3 and 21 km the vertical resolution is 1 km

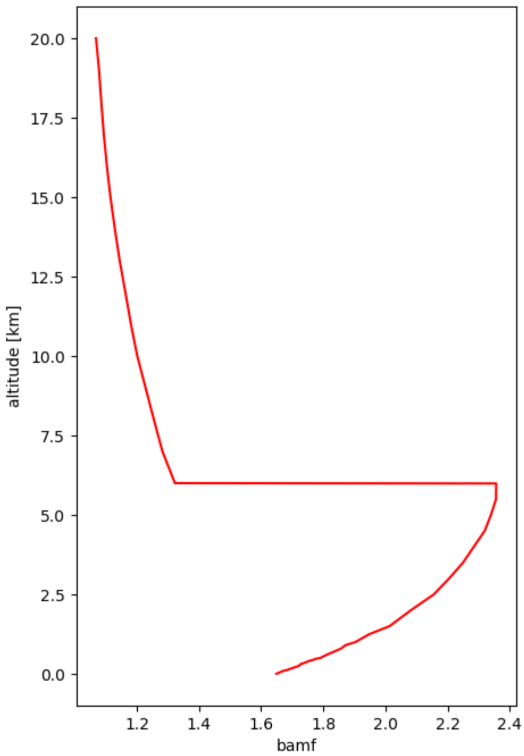

Figure B.8 – Horizontally integrated box AMFs for the airborne measurement scenario

C Appendix to chapter 4

C.1 Additional information

Example of a MYSTIC NetCDF input file for the urban canopy

```
netcdf triangle_example {
    dimensions:
            Nvert = 6 ;
            Ndim = 3 ;
            Ntriangles = 5 ;
            Ncorner = 3 ;
            N_materials = 4 ;

    variables:
            double vertices(Nvert, Ndim) ;
                    vertices:_FillValue = NaN ;
            int64 triangles(Ntriangles, Ncorner) ;
            int64 material_of_triangle(Ntriangles) ;
            double material_albedo(N_materials) ;
                    material_albedo:_FillValue = NaN ;
            string material_type(N_materials) ;
            double temperature_of_triangle(Ntriangles) ;
                    temperature_of_triangle:_FillValue = NaN ;
    data:

     vertices =
            5.56999999994878, -6.07999999998719, 8.2,
            5.56999999994878, -6.07999999998719, 0,
            -3.09999999997672, 4.48000000001048, 8.2,
            -3.09999999997672, 4.48000000001048, 0,
```

```
        6.40000000002328, 12.320000000007, 8.2,
        6.40000000002328, 12.320000000007, 0;

    triangles =
        0, 2, 5,
        0, 2, 1,
        1, 2, 3,
        2, 4, 5,
        2, 4, 3,

    material_of_triangle = 0, 1, 1, 0, 1;

    material_albedo = 0.1, 0.1;

    material_type = "roof", "wall";

    temperature_of_triangle = 273.15, 273.15, 273.15, 273.15, 273.15;
}
```

The MYSTIC NetCDF input file for the urban canopy contains a temperature for each triangle, which is not used in the radiative transfer calculations for this study, but needs to be set for avoiding an error message from the MYSTIC model.

MYSTIC inputs

Table C.1 – MYSTIC inputs for AMFs simulations.

Parameter	Value
Number of photons	50000 or 500000
Wavelength [nm]	490
Solar zenith angle [°]	60 or 30
Solar azimuth angle [°]	0, 90
Viewing zenith angle [°]	0.24 - 5.47
Viewing azimuth angle [°]	90, 270
Surface albedo	0.1 or 0.2
Aircraft position x [m]	600
Aircraft position y [m]	2.5 - 997.5
Aircraft position z [m]	6000
Simulation domain [boxes]	20×20×41
Horizontal resolution [m]	5 or 50
Vertical resolution (0 - 45m) [m]	5
Vertical resolution (50 - 1000m) [m]	100
Vertical resolution (1000 - 1500m) [m]	250
Vertical resolution (2000 - 21000m) [m]	1000
Aerosol absorption and scattering	off

3D NO_2 concentration field

To obtain a realistic synthetic 3D NO_2 concentration field, we proceeded as following:

- We summed emissions from cars, busses, trucks and motorbikes from the 2015 road emission inventories from the city of Zurich.
- We rasterized the emission field to a 5 m x 5 m resolution grid and divided each grid cell by the maximum grid cell value.
- We multiplied the obtained 2D field with a concentration of 110 $\mu g\ m^{-3}$ and added a background of 15 $\mu g\ m^{-3}$, which are respectively typical high and background values found at measurement stations close to the road and on a background site (e.g. https://www.stadt-zuerich.ch/gud/de/index/umwelt_energie/luftqualitaet/messdaten/verlauf-24-stunden.html, last access: 26 July 2021). Finally, we smoothed the concentration field with a Gaussian filter with a standard deviation of 5 m to mimic the effect of turbulent dispersion.
- From the obtained ground concentration map we created 3D concentrations applying the following function to every ground pixel. Between h_0 = 0 m and h_1 = 100 m a linear concentration decrease with altitude was applied with the level corresponding concentrations c_0 = ground concentration (grid cell concentration) and c_1 = 1/5 of the

ground concentration over a background pixel. From h_1 upwards, an exponential decay function (A exp(t z) + y0) with A = 1.6, t = -1.39 and y0 = 0.09 parameters was applied. These parameters were defined by fitting a function to a measured NO_2 profile from the MuNIC campaign in 2016 (Kuhlmann et al., 2022).

- Finally the VCD calculated using the created 3D NO_2 concentration field was compared with NO_2 VCDs from the MuNIC measurement campaign in 2016 (Kuhlmann et al., 2022).

C.2 Additional figures

SCDs for a solar zenith angle of 30°

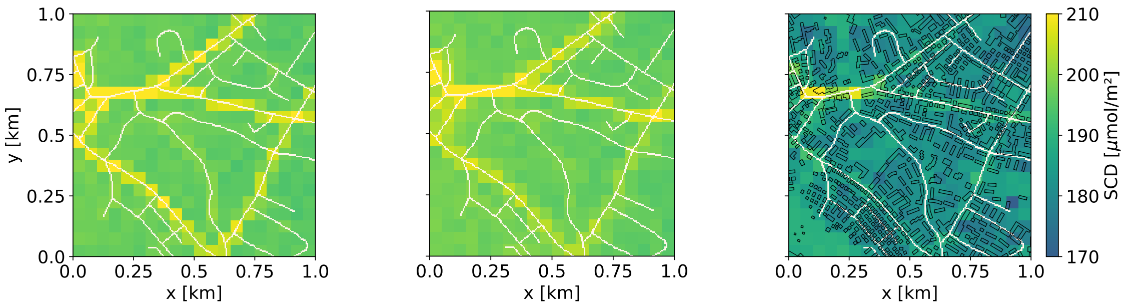

(a) SCD_{1D} (b) SCD_{3D} (c) SCD_{3D-UC}

Figure C.1 – SCDs for a simulation with SZA of 30° with (a) 1D-layer AMFs simulation, 3D-box AMFs (b) without and (c) with buildings. The roads are drawn in white and the building contours in black for the simulation with buildings.

SCDs difference plot for a solar zenith angle of 30°

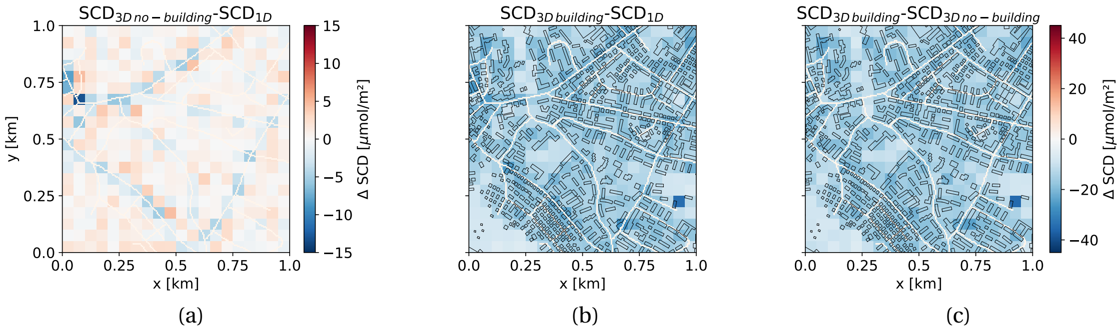

Figure C.2 – Difference plots for SCDs calculated with a solar zenith angle of 30°. (a) Difference plot between SCDs calculates with 3D-box AMFs and the SCDs calculated with 1D-layer AMFs. (b) Difference plot between SCDs calculated with 3D-box AMFs including buildings and SCDs calculated with 1D-layer AMFs. (c) Difference plot between SCDs calculated with 3D-box AMFs with and without buildings.

Increased roof albedo for the high resolution scenario

Here we show the impact of an increased albedo on the building roofs. We changed the albedo of the roofs from 0.1 to 0.2.

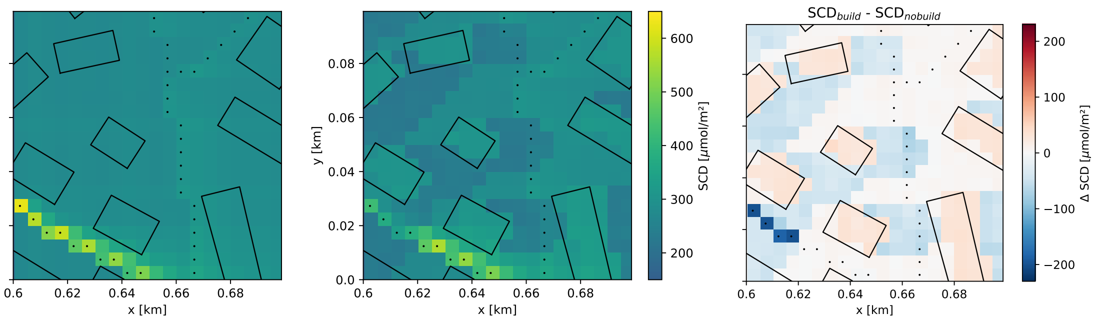

Figure C.3 – SCDs for a SAA of 90° for 3D-box AMFs simulation (a) without and (b) with buildings and (c) the difference between both. The roof albedo was changed to 0.2. The roads are drawn with dots and the building contours in black

We observe the increase in AMFs and therefore SCDs above the buildings because more photons are scattered on the roof with a higher albedo, compared to the lower ground albedo.

SCDs for a solar azimuth angle of 270°

We also computed SCDs with the 3D-box AMFs module for a SAA=270° (see Figure C.4). Similarly to observations made in the main text, SCD are smeared mostly in the direction of the main optical path (E-W-direction).

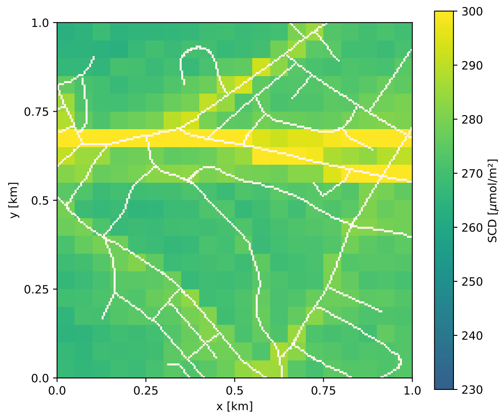

Figure C.4 – SCD without buildings and a SAA of 270°

SCDs for simulations at 420 nm

We also computed SCDs with the 1D-layer and 3D-box AMFs module at a wavelength of 420 nm. The mean value of the field is decreased by approximately 12% for the 1D and 3D simulations with and without buildings compared to simulations at 490 nm.

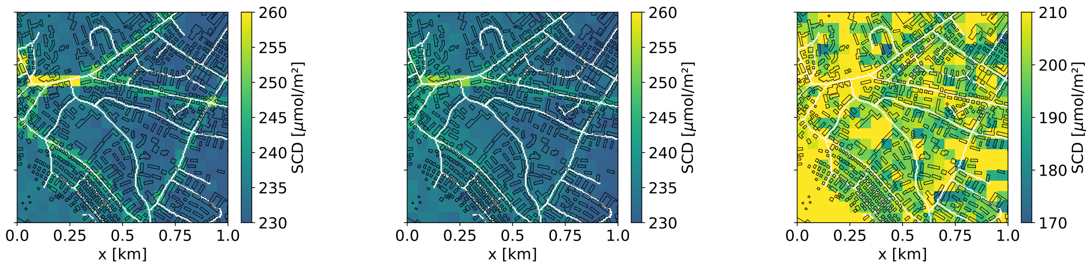

(a) SCD_{1D} (b) VCD_{3D} (c) VCD_{3D-UC}

Figure C.5 – SCD from (a) 1D-layer AMFs and 3D-box (b) without and (c) with buildings at 420 nm

Retrieving VCDs from SCDs

Figure C.6 shows VCDs retrieved from the assumed "true" SCD_{3D} using (a) 1D-layer AMFs and (b) 3D-box AMFs. Here 1D-layer AMFs used to retrieve VCDs fails to correct for the spatially smeared SCD field.

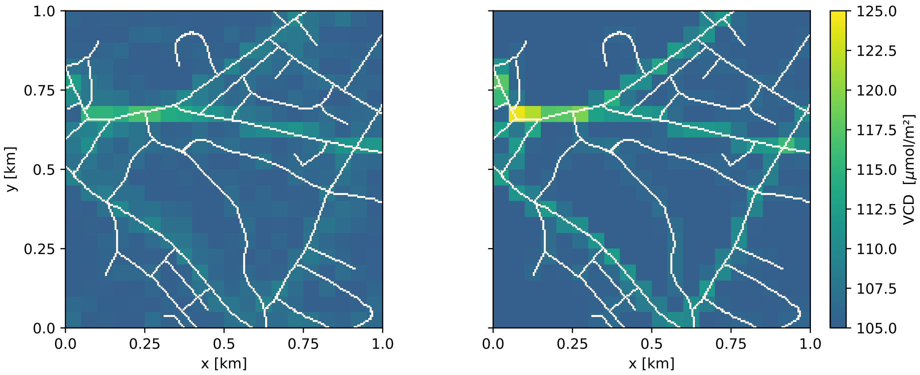

(a) VCD_{1D} (b) VCD_{3D}

Figure C.6 – VCDs retrieved with (a) 1D-layer AMFs and (b) 3D-box AMFs without buildings.

Footprints

Footprints with aerosols

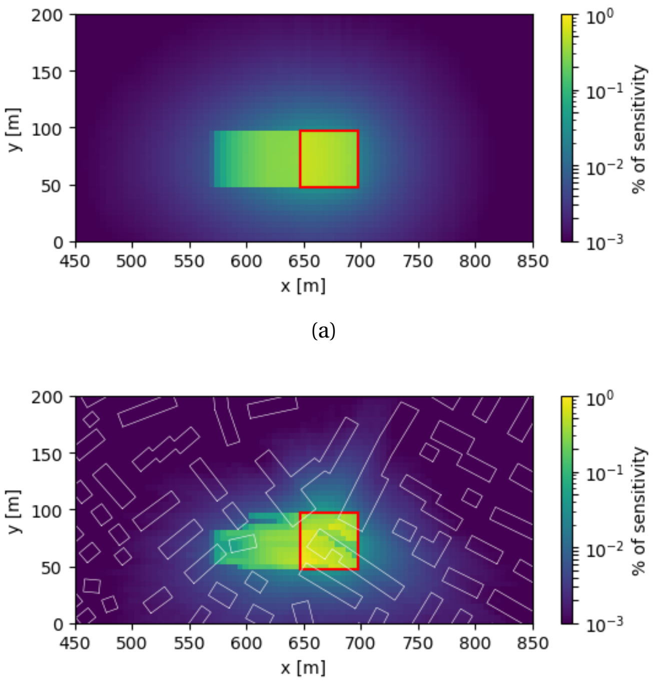

(a)

(b)

Figure C.7 – (a) Footprint without buildings and with aerosols. 55.2% of the signal is located outside the ground pixel (i.e. outside the red frame). (b) Footprint with buildings and aerosols. 55.2% of the instrument sensitivity is located outside the ground pixel. Building contours are drawn in white.

Footprints for a solar zenith angle of 20° and 40°

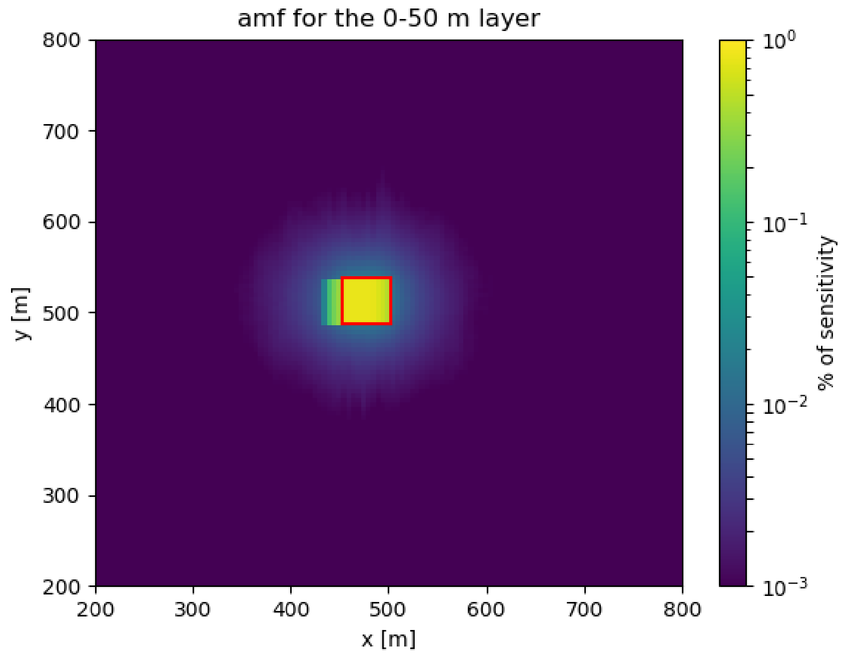

(a)

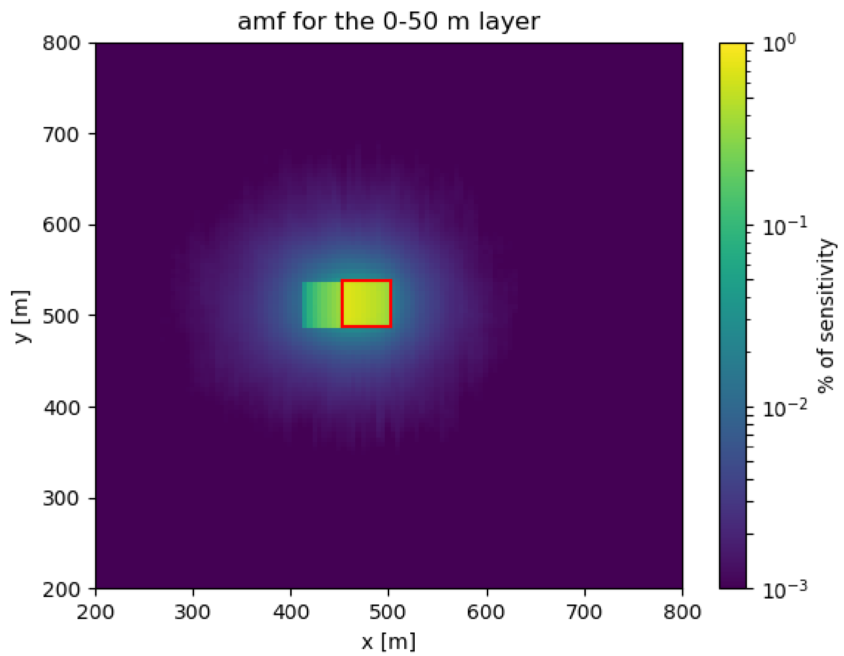

(b)

Figure C.8 – Effect of SZA on APEX footprint. Simulation with SZA = (a) 20° and (b) 40°. Respectively 27.4% and 45.2% of the sensitivity is located outside the ground pixel (red square).

C.3 Computational time

Simulations with buildings

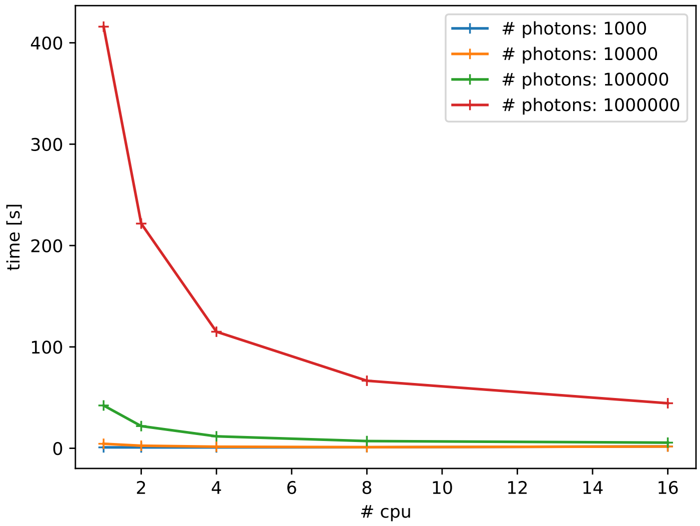

(a)

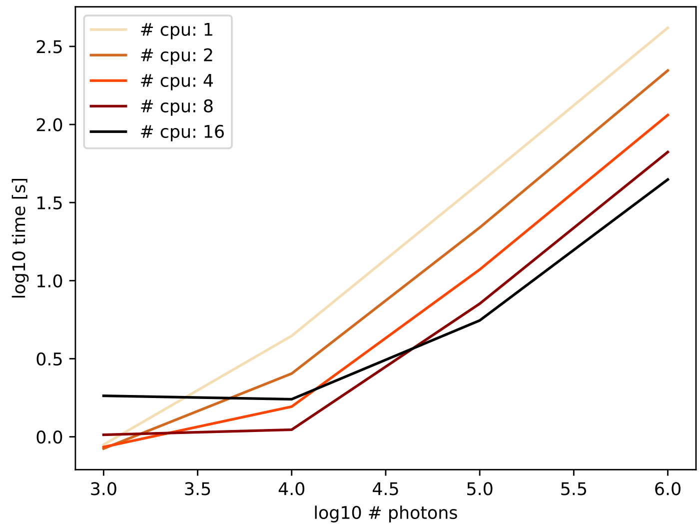

Figure C.9 – Computational time for simulations with buildings depending on (a) amount of used CPUs and (b) amount of photons used for a single simulation.

Simulations without buildings

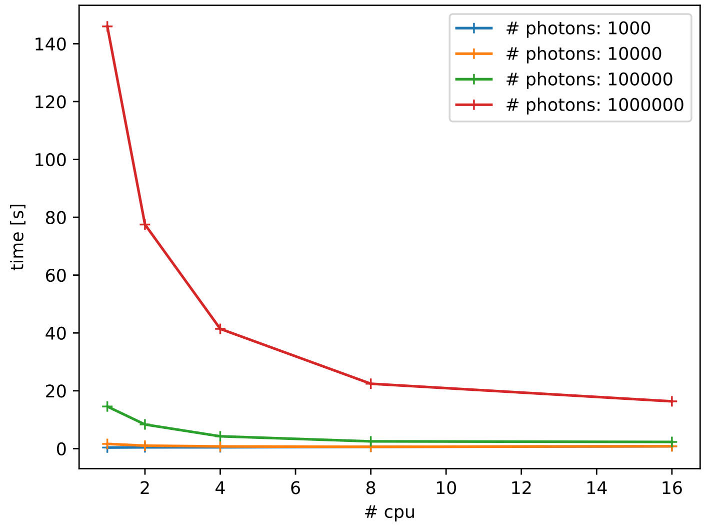

(a)

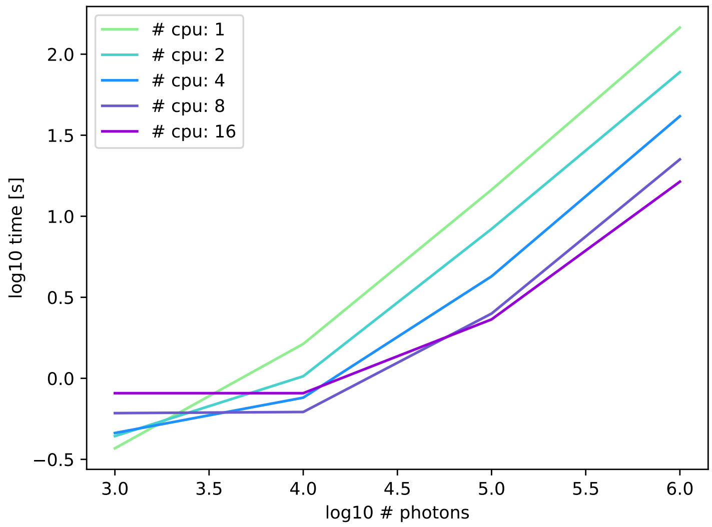

(b)

Figure C.10 – Computational time for simulations without buildings depending on (a) amount of CPUs used and (b) photon amount used for a single simulation.

D Appendix to chapter 5

D.1 Additional information

Table D.1 – List of measurement stations and their data availability during the APEX stripes and * for data availability problems

Station	2010						2013				2016			
name / (ID)	1B	2B	3B	4B	5B	6B	1B	2B	3B	4B	1B	2B	3B	4B
Zuerich Heubeeribueel (HEU)	X					*X	*X	X						X
Zuerich Kaserne, NABEL (KAS)		X			X			X					X	
Zuerich Schimmelstr. (SCH)		X			X			X					X	
Zuerich Stampfenbachstr. (STA)		X			X			X					X	
Wettswil Filderen (FIL)		X	X	X	X			X						
Duebendorf NABEL (DUB)	X					*X	X	X						X
Opfikon Balsberg (OPB)			X	X						X	X			

Table D.2 – Ground stations coordinates

Station	lon	lat
HEU	8.5659	47.3815
KAS	8.5304	47.378
SCH	8.5236	47.371
STA	8.5398	47.387
FIL	8.4619	47.341
DUB	8.6134	47.403
OPB	8.5701	47.439

D.2 Additional figures

Table D.3 – APEX stripe times

Stripe	Date	Time UTC	
		Begin	End
ZH-2010-1B	2010-06-26	07:56:00	08:00:00
ZH-2010-2B	2010-06-26	08:05:00	08:09:00
ZH-2010-3B	2010-06-26	08:13:00	08:17:00
ZH-2010-4B	2010-06-26	15:27:00	15:32:00
ZH-2010-5B	2010-06-26	15:35:00	15:49:00
ZH-2010-6B	2010-06-26	15:43:00	15:48:00
ZH-2013-1B	2013-08-30	11:24:00	11:30:00
ZH-2013-2B	2013-08-30	11:36:00	11:42:00
ZH-2013-3B	2013-08-30	11:49:00	11:54:00
ZH-2013-4B	2013-08-30	11:59:00	12:05:00
ZH-2016-1B	2016-07-07	10:35:00	10:39:00
ZH-2016-2B	2016-07-07	10:45:00	10:50:00
ZH-2016-3B	2016-07-07	10:55:00	11:00:00
ZH-2016-4B	2016-07-07	11:06:00	11:11:00

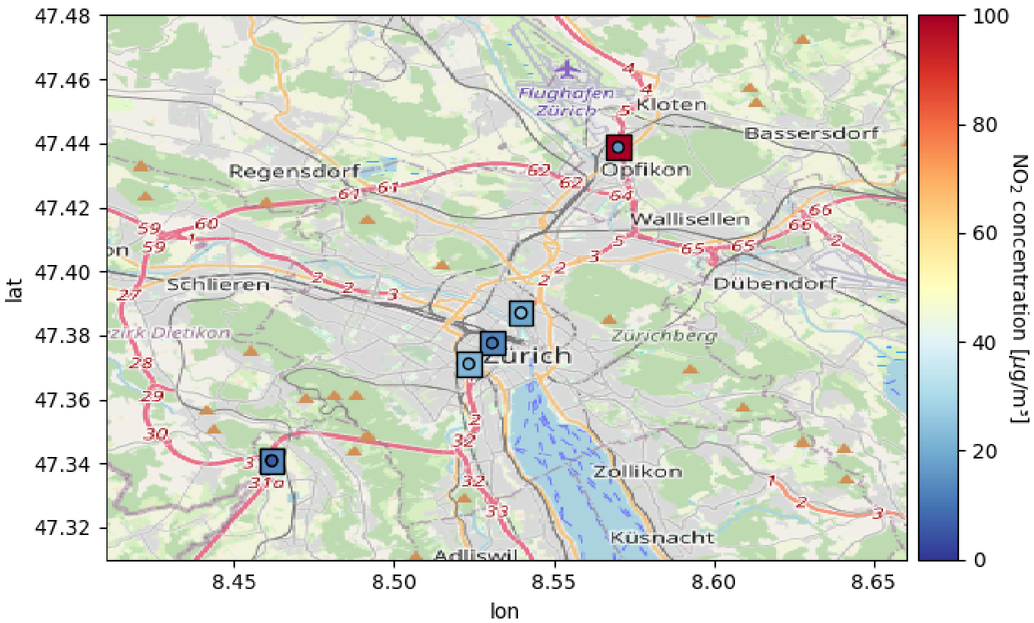

Figure D.1 – Near surface concentrations from APEX (APEX 2010 afternoon campaign), retrieved with the 3D-box AMFs (squares) and ground measurement concentrations at 4 m at the location of ground air pollution monitoring stations (circles). Map informations were obtained from OpenStreetMap (© OpenStreetMap contributors 2022. Distributed under the Open Data Commons Open Database License (ODbL) v1.0.)

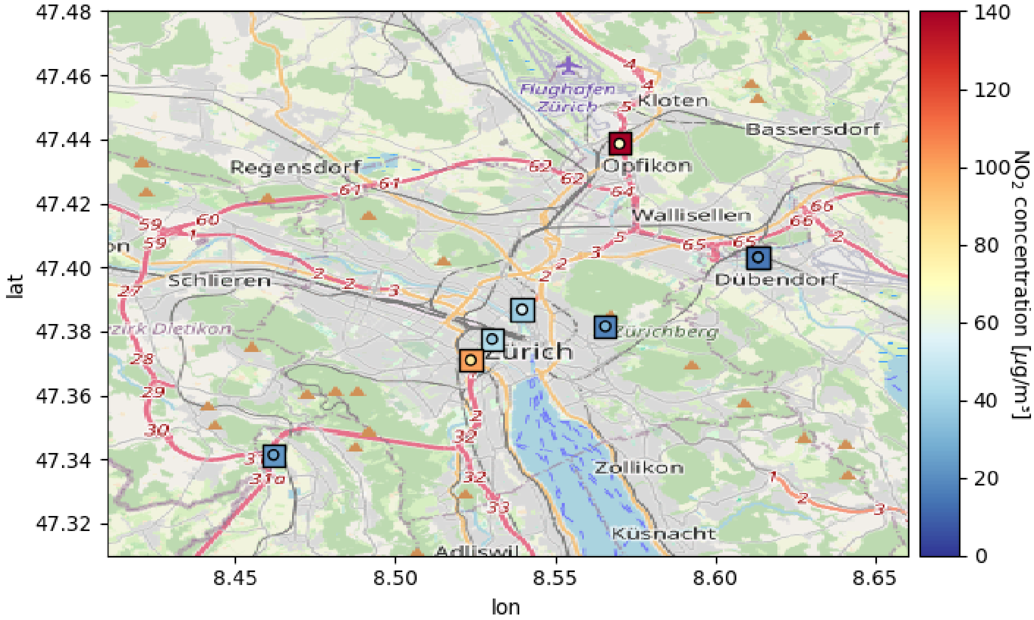

Figure D.2 – Near surface concentrations from APEX (APEX 2013 campaign), retrieved with the 3D-box AMFs (squares) and ground measurement concentrations at 4 m at the location of ground air pollution monitoring stations (circles). Map informations were obtained from OpenStreetMap (© OpenStreetMap contributors 2022. Distributed under the Open Data Commons Open Database License (ODbL) v1.0.)

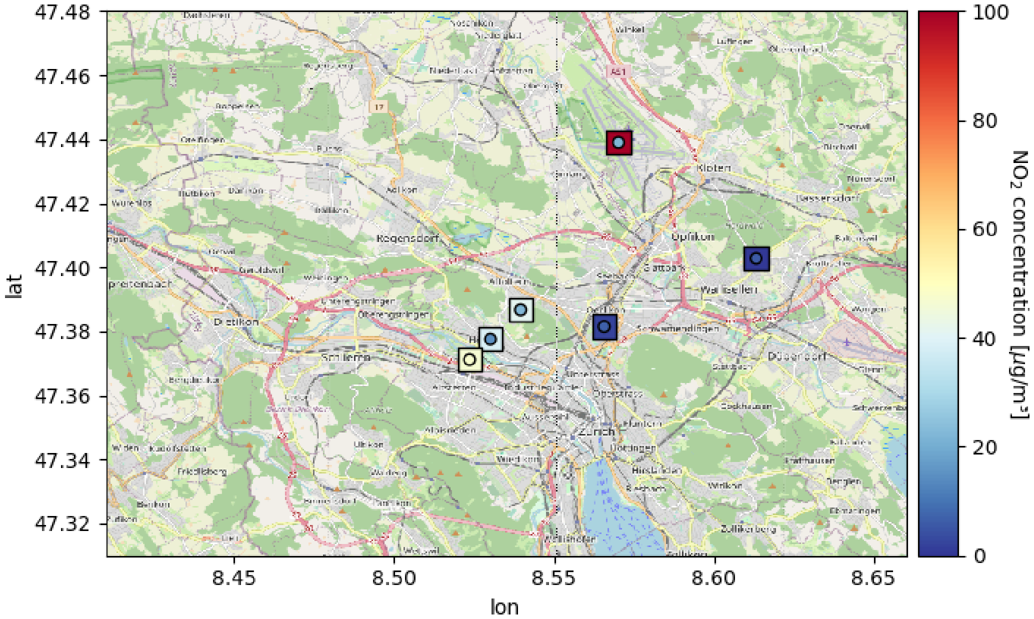

Figure D.3 – Near surface concentrations from APEX (APEX 2016 campaign), retrieved with the 3D-box AMFs (squares) and ground measurement concentrations at 4 m at the location of ground air pollution monitoring stations (circles). Map informations were obtained from OpenStreetMap (© OpenStreetMap contributors 2022. Distributed under the Open Data Commons Open Database License (ODbL) v1.0.)

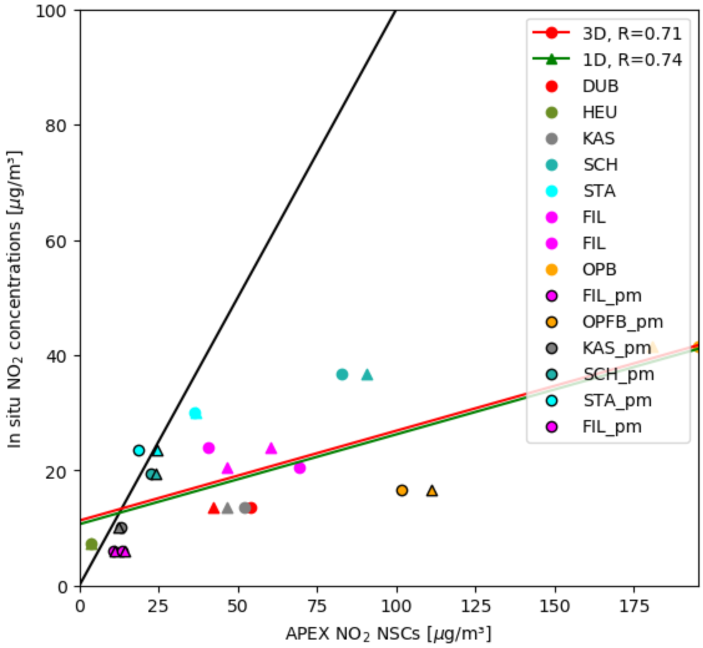

Figure D.4 – Scatter plot between surface in-situ NO_2 concentrations and APEX 2010 NO_2 near surface concentrations retrieved with 1D-layer AMFs (triangles) and 3D-box AMFs (circles). The symbols from the afternoon strip are marked with a black contour. The 1:1 line is plotted in black and the fitted line in red and green for 3D and 1D AMFs, respectively.

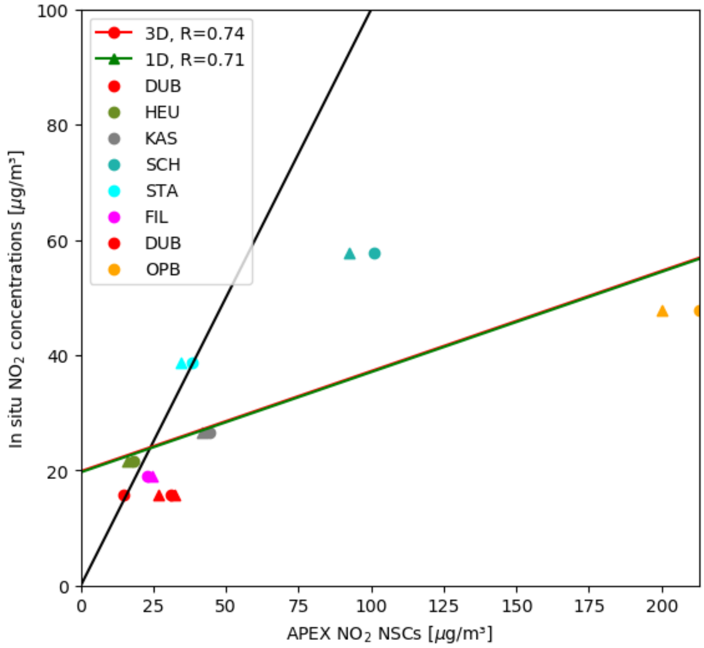

Figure D.5 – Scatter plot between surface in-situ NO_2 concentrations and APEX NO_2 near surface concentrations retrieved with 1D-layer AMFs (triangles) and 3D-box AMFs (circles) for the 2013 APEX campaign. The 1:1 line is plotted in black and the fitted line in red and green for 3D and 1D AMFs, respectively.

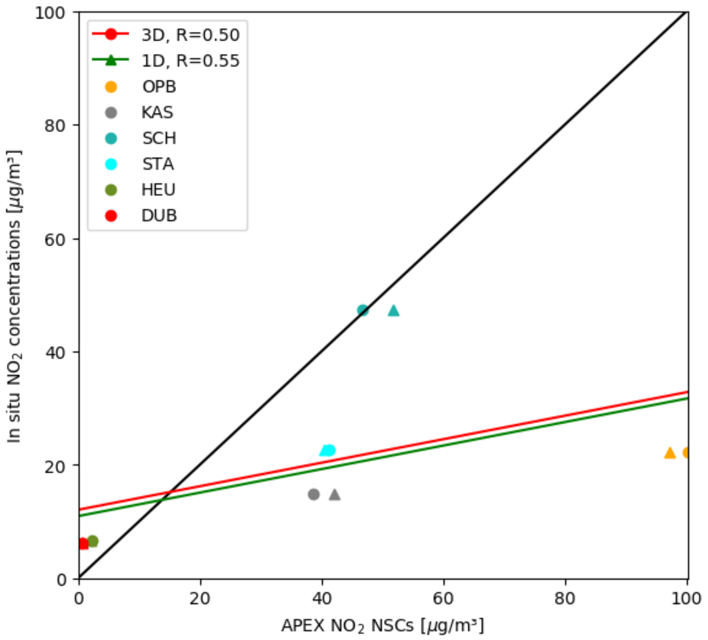

Figure D.6 – Scatter plot between surface in-situ NO_2 concentrations and APEX NO_2 near surface concentrations retrieved with 1D-layer AMFs (triangles) and 3D-box AMFs (circles) for the APEX 2016 campaign. The 1:1 line is plotted in black and the fitted line in red and green for 3D and 1D AMFs, respectively.

Bibliography

BAFU (2020). Luftqualität 2019. Messresultate des Nationalen Beobachtungsnetzes für Luftfremdstoffe (NABEL). Report.

Beelen, R., Raaschou-Nielsen, O., Stafoggia, M., Andersen, Z. J., Weinmayr, G., Hoffmann, B., Wolf, K., Samoli, E., Fischer, P., Nieuwenhuijsen, M., Vineis, P., Xun, W. W., Katsouyanni, K., Dimakopoulou, K., Oudin, A., Forsberg, B., Modig, L., Havulinna, A. S., Lanki, T., Turunen, A., Oftedal, B., Nystad, W., Nafstad, P., De Faire, U., Pedersen, N. L., Östenson, C.-G., Fratiglioni, L., Penell, J., Korek, M., Pershagen, G., Eriksen, K. T., Overvad, K., Ellermann, T., Eeftens, M., Peeters, P. H., Meliefste, K., Wang, M., Bueno-de Mesquita, B., Sugiri, D., Krämer, U., Heinrich, J., de Hoogh, K., Key, T., Peters, A., Hampel, R., Concin, H., Nagel, G., Ineichen, A., Schaffner, E., Probst-Hensch, N., Künzli, N., Schindler, C., Schikowski, T., Adam, M., Phuleria, H., Vilier, A., Clavel-Chapelon, F., Declercq, C., Grioni, S., Krogh, V., Tsai, M.-Y., Ricceri, F., Sacerdote, C., Galassi, C., Migliore, E., Ranzi, A., Cesaroni, G., Badaloni, C., Forastiere, F., Tamayo, I., Amiano, P., Dorronsoro, M., Katsoulis, M., Trichopoulou, A., Brunekreef, B., and Hoek, G. (2014). Effects of long-term exposure to air pollution on natural-cause mortality: an analysis of 22 European cohorts within the multicentre ESCAPE project. *The Lancet*, 383(9919):785–795.

Bell, M. L., Peng, R. D., and Dominici, F. (2006). The Exposure-Response Curve for Ozone and Risk of Mortality and the Adequacy of Current Ozone Regulations. *Environmental Health Perspectives*, 114(4):532–536.

Berchet, A., Zink, K., Muller, C., Oettl, D., Brunner, J., Emmenegger, L., and Brunner, D. (2017). A cost-effective method for simulating city-wide air flow and pollutant dispersion at building resolving scale. *Atmospheric Environment*, 158:181–196.

Berk, A., Anderson, G. P., Bernstein, L. S., Acharya, P. K., Dothe, H., Matthew, M. W., Adler-Golden, S. M., Chetwynd Jr, J. H., Richtsmeier, S. C., Pukall, B., et al. (1999). MODTRAN4 radiative transfer modeling for atmospheric correction. In *Optical Spectroscopic Techniques and Instrumentation for Atmospheric and Space Research III*, volume 3756, pages 348–353, International Society for Optics and Photonics, Denver, CO, United States.

Boersma, K. F., Eskes, H. J., Dirksen, R. J., van der A, R. J., Veefkind, J. P., Stammes, P., Huijnen, V., Kleipool, Q. L., Sneep, M., Claas, J., Leitão, J., Richter, A., Zhou, Y., and Brunner, D.

(2011). An improved tropospheric NO_2 column retrieval algorithm for the Ozone Monitoring Instrument. *Atmospheric Measurement Techniques*, 4(9):1905–1928.

Bouwman, A. F., Van Vuuren, D. P., Derwent, R. G., and Posch, M. (2002). A Global Analysis of Acidification and Eutrophication of Terrestrial ecosystems. *Water, Air, and Soil Pollution*, 141(1):349–382.

Burrows, J. P., Weber, M., Buchwitz, M., Rozanov, V., Ladstätter-Weißenmayer, A., Richter, A., DeBeek, R., Hoogen, R., Bramstedt, K., Eichmann, K. U., , Eisinger, M., and Perner, D. (1999). The Global Ozone Monitoring Experiment (GOME): Mission Concept and First Scientific Results. *Journal of the Atmospheric Sciences*, 56(2):151–175.

Bär, P. (2016). Luftbilanz 2016: Resultate der flächendeckenden Messkampagne. Available at: https://www.stadt-zuerich.ch/gud/de/index/umwelt_energie/luftqualitaet/publikationen/luftbilanz-2016.html (last access: 5 October 2021).

Casaballe, N., Di Martino, M., Osorio, M., Ferrari, J., Wagner, T., and Frins, E. (2020). Improved algorithm with adaptive regularization for tomographic reconstruction of gas distributions using DOAS measurements. *Applied Optics*, 59(13):D179–D188.

Cracknell, A. P. and Varotsos, C. (2012). *Remote sensing and atmospheric ozone: Human activities versus natural variability*. Springer Science & Business Media, Berlin/Heidelberg, Germany.

Crutzen, P. J. (1970). The influence of nitrogen oxides on the atmospheric ozone content. *Quarterly Journal of the Royal Meteorological Society*, 96(408):320–325.

de Goeij, B. T. G., Otter, G. C. J., van Wakeren, J. M. O., Veefkind, J. P., Vlemmix, T., Ge, X., Levelt, P. F., Dirks, B. P. F., Toet, P. M., van der Wal, L. F., and Jansen, R. (2017). First aircraft test results of a compact, low cost hyperspectral imager for earth observation from space. In *International Conference on Space Optics — ICSO 2016*, volume 10562, pages 465 – 475, International Society for Optics and Photonics, Biarritz, France. SPIE.

de Graaf, M., Sihler, H., Tilstra, L. G., and Stammes, P. (2016). How big is an OMI pixel? *Atmos. Meas. Tech.*, 9(8):3607–3618.

Deutschmann, T., Beirle, S., Frieß, U., Grzegorski, M., Kern, C., Kritten, L., Platt, U., Prados-Román, C., Puķīte, J., Wagner, T., Werner, B., and Pfeilsticker, K. (2011). The Monte Carlo atmospheric radiative transfer model McArtim: Introduction and validation of Jacobians and 3D features. *Journal of Quantitative Spectroscopy and Radiative Transfer*, 112(6):1119–1137.

Dimitropoulou, E., Van Roozendael, M., Hendrick, F., Merlaud, A., Tack, F., Fayt, C., Hermans, C., and Pinardi, G. (2019). One year of 3-D MAX-DOAS tropospheric NO2 measurements over Brussels. In *EGU General Assembly Conference Abstracts*, EGU General Assembly Conference, 7–12 April 2019, page 5874, Vienna, Austria.

Düring, I., Bächlin, W., Ketzel, M., Baum, A., Friedrich, U., and Wurzler, S. (2011). A new simplified NO/NO_2 conversion model under consideration of direct NO_2-emissions. *Meteorologische Zeitschrift*, 20(1):67.

D'Amato, G., Bergmann, K. C., Cecchi, L., Annesi-Maesano, I., Sanduzzi, A., Liccardi, G., Vitale, C., Stanziola, A., and D'Amato, M. (2014). Climate change and air pollution: Effects on pollen allergy and other allergic respiratory diseases. *Allergo Journal International*, 23(1):17–23.

Emde, C., Buras-Schnell, R., Kylling, A., Mayer, B., Gasteiger, J., Hamann, U., Kylling, J., Richter, B., Pause, C., Dowling, T., and Bugliaro, L. (2016). The libRadtran software package for radiative transfer calculations (version 2.0.1). *Geoscientific Model Development*, 9(5):1647–1672.

Emde, C. and Mayer, B. (2007). Simulation of solar radiation during a total eclipse: a challenge for radiative transfer. *Atmospheric Chemistry and Physics*, 7(9):2259–2270.

Emde, C., Yu, H., Kylling, A., van Roozendael, M., Stebel, K., Veihelmann, B., and Mayer, B. (2022). Impact of 3D cloud structures on the atmospheric trace gas products from UV–Vis sounders – Part 1: Synthetic dataset for validation of trace gas retrieval algorithms. *Atmospheric Measurement Techniques*, 15(5):1587–1608.

Fischer, E. M. and Schär, C. (2010). Consistent geographical patterns of changes in high-impact European heatwaves. *Nature Geoscience*, 3(6):398–403.

Frankenberg, C., Platt, U., and Wagner, T. (2005). Iterative maximum a posteriori (IMAP)-DOAS for retrieval of strongly absorbing trace gases: Model studies for CH_4 and CO_2 retrieval from near infrared spectra of SCIAMACHY onboard ENVISAT. *Atmospheric Chemistry and Physics*, 5(1):9–22.

Frieß, U., Monks, P. S., Remedios, J. J., Rozanov, A., Sinreich, R., Wagner, T., and Platt, U. (2006). MAX-DOAS O_4 measurements: A new technique to derive information on atmospheric aerosols: 2. Modeling studies. *Journal of Geophysical Research: Atmospheres*, 111(D14).

Frins, E., Bobrowski, N., Platt, U., and Wagner, T. (2006). Tomographic multiaxis-differential optical absorption spectroscopy observations of Sun-illuminated targets: a technique providing well-defined absorption paths in the boundary layer. *Applied optics*, 45(24):6227–6240.

García-Herrera, R., Díaz, J., Trigo, R. M., Luterbacher, J., and Fischer, E. M. (2010). A Review of the European Summer Heat Wave of 2003. *Critical Reviews in Environmental Science and Technology*, 40(4):267–306.

Gastellu-Etchegorry, J.-P., Yin, T., Lauret, N., Cajgfinger, T., Gregoire, T., Grau, E., Feret, J.-B., Lopes, M., Guilleux, J., Dedieu, G., Malenovský, Z., Cook, D. B., Morton, D., Rubio, J., Durrieu, S., Cazanave, G., Martin, E., and Ristorcelli, T. (2015). Discrete Anisotropic Radiative Transfer (DART 5) for Modeling Airborne and Satellite Spectroradiometer and LIDAR Acquisitions of Natural and Urban Landscapes. *Remote Sensing*, 7(2).

Guerreiro, C. B., Foltescu, V., and de Leeuw, F. (2014). Air quality status and trends in Europe. *Atmospheric Environment*, 98:376–384.

Heimann, I., Bright, V., McLeod, M., Mead, M., Popoola, O., Stewart, G., and Jones, R. (2015). Source attribution of air pollution by spatial scale separation using high spatial density networks of low cost air quality sensors. *Atmospheric Environment*, 113:10–19.

Hendrick, F., Müller, J.-F., Clémer, K., Wang, P., Mazière, M. D., Fayt, C., Gielen, C., Hermans, C., Ma, J. Z., Pinardi, G., Stavrakou, T., Vlemmix, T., and Van Roozendael, M. (2014). Four years of ground-based MAX-DOAS observations of HONO and NO_2 in the Beijing area. *Atmospheric Chemistry and Physics*, 14(2):765–781.

Hönninger, G. and Platt, U. (2002). Observations of BrO and its vertical distribution during surface ozone depletion at Alert. *Atmospheric Environment*, 36(15-16):2481–2489.

Hueni, A., Lenhard, K., Baumgartner, A., and Schaepman, M. E. (2013). Airborne Prism Experiment Calibration Information System. *IEEE Transactions on Geoscience and Remote Sensing*, 51(11):5169–5180.

Irie, H., Takashima, H., Kanaya, Y., Boersma, K. F., Gast, L., Wittrock, F., Brunner, D., Zhou, Y., and Van Roozendael, M. (2011). Eight-component retrievals from ground-based MAX-DOAS observations. *Atmospheric Measurement Techniques*, 4(6):1027–1044.

Iwabuchi, H. (2006). Efficient Monte Carlo Methods for Radiative Transfer Modeling. *Journal of the Atmospheric Sciences*, 63(9):2324–2339.

Iwabuchi, H. and Okamura, R. (2017). Multispectral Monte Carlo radiative transfer simulation by the maximum cross-section method. *Journal of Quantitative Spectroscopy and Radiative Transfer*, 193:40–46.

Kazahaya, R., Mori, T., Kazahaya, K., and Hirabayashi, J.-i. (2008). Computed tomography reconstruction of SO_2 concentration distribution in the volcanic plume of Miyakejima, Japan, by airborne traverse technique using three UV spectrometers. *Geophysical research letters*, 35(13).

Krings, T., Gerilowski, K., Buchwitz, M., Hartmann, J., Sachs, T., Erzinger, J., Burrows, J. P., and Bovensmann, H. (2013). Quantification of methane emission rates from coal mine ventilation shafts using airborne remote sensing data. *Atmospheric Measurement Techniques*, 6(1):151–166.

Krings, T., Gerilowski, K., Buchwitz, M., Reuter, M., Tretner, A., Erzinger, J., Heinze, D., Pflüger, U., Burrows, J. P., and Bovensmann, H. (2011). MAMAP – a new spectrometer system for column-averaged methane and carbon dioxide observations from aircraft: retrieval algorithm and first inversions for point source emission rates. *Atmospheric Measurement Techniques*, 4:1735–1758.

Krueger, A. J., Walter, L. S., Bhartia, P. K., Schnetzler, C. C., Krotkov, N. A., Sprod, I., and Bluth, G. J. S. (1995). Volcanic sulfur dioxide measurements from the total ozone mapping spectrometer instruments. *Journal of Geophysical Research: Atmospheres*, 100(D7):14057–14076.

Kuhlmann, G. (2021). flexDOAS – a flexible python library for DOAS analysis. https://gitlab.com/empa503/remote-sensing/flexdoas, last access: December 29, 2021.

Kuhlmann, G., Berchet, A., and Brunner, D. (2017). High-resolution remote sensing and modelling of NO_2 air pollution over the city of Zurich. In *10th EARSeL SIG Imaging Spectroscopy Workshop 2017*, Zurich, Switzerland.

Kuhlmann, G., Chan, K. L., Donner, S., Zhu, Y., Schwaerzel, M., Dörner, S., Chen, J., Hueni, A., Nguyen, D. H., Damm, A., Schütt, A., Dietrich, F., Brunner, D., Liu, C., Buchmann, B., Wagner, T., and Wenig, M. (2022). Mapping the spatial distribution of NO_2 with in situ and remote sensing instruments during the Munich NO_2 imaging campaign. *Atmospheric Measurement Techniques*, 15(6):1609–1629.

Kuhlmann, G., Hueni, A., Damm, A., and Brunner, D. (2016). An Algorithm for In-Flight Spectral Calibration of Imaging Spectrometers. *Remote Sensing*, 8(12):1017.

Kylling, A., Emde, C., Yu, H., van Roozendael, M., Stebel, K., Veihelmann, B., and Mayer, B. (2021). Impact of 3D Cloud Structures on the Atmospheric Trace Gas Products from UV-VIS Sounders – Part III: bias estimate using synthetic and observational data. *Atmospheric Measurement Techniques Discussions*, 2021:1–28.

Landrigan, P. J., Fuller, R., Acosta, N. J. R., Adeyi, O., Arnold, R., Basu, N., Baldé, A. B., Bertollini, R., Bose-O'Reilly, S., Boufford, J. I., Breysse, P. N., Chiles, T., Mahidol, C., Coll-Seck, A. M., Cropper, M. L., Fobil, J., Fuster, V., Greenstone, M., Haines, A., Hanrahan, D., Hunter, D., Khare, M., Krupnick, A., Lanphear, B., Lohani, B., Martin, K., Mathiasen, K. V., McTeer, M. A., Murray, C. J. L., Ndahimananjara, J. D., Perera, F., Potočnik, J., Preker, A. S., Ramesh, J., Rockström, J., Salinas, C., Samson, L. D., Sandilya, K., Sly, P. D., Smith, K. R., Steiner, A., Stewart, R. B., Suk, W. A., van Schayck, O. C. P., Yadama, G. N., Yumkella, K., and Zhong, M. (2018). The *Lancet* Commission on pollution and health. *The Lancet*, 391(10119):462–512.

Lee, C., Martin, R. V., van Donkelaar, A., O'Byrne, G., Krotkov, N., Richter, A., Huey, L. G., and Holloway, J. S. (2009). Retrieval of vertical columns of sulfur dioxide from SCIAMACHY and OMI: Air mass factor algorithm development, validation, and error analysis. *Journal of Geophysical Research: Atmospheres*, 114(D22).

Leigh, R. J., Corlett, G. K., Frieß, U., and Monks, P. S. (2007). Spatially resolved measurements of nitrogen dioxide in an urban environment using concurrent multi-axis differential optical absorption spectroscopy. *Atmospheric Chemistry and Physics*, 7(18):4751–4762.

Lerot, C., Van Roozendael, M., Lambert, J.-C., Granville, J., Van Gent, J., Loyola, D., and Spurr, R. (2010). The GODFIT algorithm: a direct fitting approach to improve the accuracy of total ozone measurements from GOME. *International Journal of Remote Sensing*, 31(2):543–550.

Lyapustin, A. and Kaufman, Y. (2001). Role of adjacency effect in the remote sensing of aerosol. *Journal of Geophysical Research: Atmospheres*, 106(D11):11909–11916.

Marchuk, G. I., Mikhailov, G. A., Nazaraliev, M. A., Dacbinjan, R. A., Kargin, B. A., and Elepov, B. S. (1980). *Monte Carlo methods in atmospheric optics*. Springer Series in Optical Sciences, Springer, Berlin/Heidelberg, Germany.

Marshak, A. and Davis, A. (2005). *3D Radiative Transfer in Cloudy Atmospheres*. Springer, Heidelberg, Germany.

Martin, R. V., Jacob, D. J., Chance, K., Kurosu, T. P., Palmer, P. I., and Evans, M. J. (2003). Global inventory of nitrogen oxide emissions constrained by space-based observations of NO_2 columns. *Journal of Geophysical Research*, 108(D17).

Massie, S. T., Sebastian Schmidt, K., Eldering, A., and Crisp, D. (2017). Observational evidence of 3-D cloud effects in OCO-2 CO_2 retrievals. *Journal of Geophysical Research: Atmospheres*, 122(13):7064–7085.

Mayer, B. (2009). Radiative transfer in the cloudy atmosphere. In *EPJ Web of Conferences*, volume 1, pages 75–99, Les Ulis, France.

Mayer, B. and Kylling, A. (2005). Technical note: The libRadtran software package for radiative transfer calculations - description and examples of use. *Atmospheric Chemistry and Physics*, 5(7):1855–1877.

McPeters, R. D., Frith, S., and Labow, G. J. (2015). OMI total column ozone: extending the long-term data record. *Atmospheric Measurement Techniques*, 8(11):4845–4850.

Merlaud, A., Constantin, D., Mingireanu, F., Mocanu, I., Fayt, C., Maes, J., Murariu, G., Voiculescu, M., Georgescu, L., and Van Roozendael, M. (2013). Small whiskbroom imager for atmospheric composition monitoring (SWING) from an unmanned aerial vehicle (UAV). In *Proceedings of the 21st ESA Symposium on European Rocket & Balloon Programmes and related Research*, pages 9–13, Thun, Switzerland.

Mijling, B., van der A, R. J., and Zhang, Q. (2013). Regional nitrogen oxides emission trends in East Asia observed from space. *Atmospheric Chemistry & Physics*, 13(23).

Minomura, M., Kuze, H., and Takeuchi, N. (2001). Adjacency Effect in the Atmospheric Correction of Satellite Remote Sensing Data: Evaluation of the Influence of Aerosol Extinction Profiles. *Optical review*, 8(2):133–141.

Mueller, M. D., Wagner, M., Barmpadimos, I., and Hueglin, C. (2015). Two-week NO_2 maps for the City of Zurich, Switzerland, derived by statistical modelling utilizing data from a routine passive diffusion sampler network. *Atmospheric Environment*, 106:1–10.

Mussetti, G., Brunner, D., Henne, S., Allegrini, J., Krayenhoff, E. S., Schubert, S., Feigenwinter, C., Vogt, R., Wicki, A., and Carmeliet, J. (2020). COSMO-BEP-Tree v1. 0: a coupled urban climate model with explicit representation of street trees. *Geoscientific Model Development*, 13(3):1685–1710.

Nowlan, C. R., Liu, X., Leitch, J. W., Chance, K., González Abad, G., Liu, C., Zoogman, P., Cole, J., Delker, T., Good, W., Murcray, F., Ruppert, L., Soo, D., Follette-Cook, M. B., Janz, S. J., Kowalewski, M. G., Loughner, C. P., Pickering, K. E., Herman, J. R., Beaver, M. R., Long, R. W., Szykman, J. J., Judd, L. M., Kelley, P., Luke, W. T., Ren, X., and Al-Saadi, J. A. (2016). Nitrogen dioxide observations from the Geostationary Trace gas and Aerosol Sensor Optimization (GeoTASO) airborne instrument: Retrieval algorithm and measurements during DISCOVER-AQ Texas 2013. *Atmospheric Measurement Techniques*, 9(6):2647–2668.

Oettl, D. (2015). Quality assurance of the prognostic, microscale wind-field model GRAL 14.8 using wind-tunnel data provided by the German VDI guideline 3783-9. *Journal of Wind Engineering and Industrial Aerodynamics*, 142:104–110.

Oettl, D. (2016). Documentation of the prognostic mesoscale model GRAMM (Graz Mesoscale Model) Vs. 15.12. http://app.luis.steiermark.at/berichte/Download/Fachberichte/Lu_01_2017_GRAL_Documentation_Sep2017.pdf, last accessed 10 January 2022.

Oettl, D. (2017). Documentation of the Lagrangian Particle Model GRAL (Graz Lagrangian Model) Vs. 17.9. http://app.luis.steiermark.at/berichte/Download/Fachberichte/Lu_01_2017_GRAL_Documentation_Sep2017.pdf, last accessed 10 January 2022.

Palmer, P. I., Jacob, D. J., Chance, K., Martin, R. V., Spurr, R. J. D., Kurosu, T. P., Bey, I., Yantosca, R., Fiore, A., and Li, Q. (2001). Air mass factor formulation for spectroscopic measurements from satellites: Application to formaldehyde retrievals from the Global Ozone Monitoring Experiment. *Journal of Geophysical Research: Atmospheres*, 106(D13):14539–14550.

Platt, U. and Stutz, J. (2008). *Differential optical absorption spectroscopy: principles and applications*. Springer Verlag, Heidelberg, Germany.

Pöhler, D. (2010). *Determination of two dimensional trace gas distributions using tomographic LP-DOAS measurements in the city of Heidelberg, Germany*. PhD thesis, University of Heidelberg.

Popp, C., Brunner, D., Damm, A., Van Roozendael, M., Fayt, C., and Buchmann, B. (2012). High-resolution NO_2 remote sensing from the Airborne Prism EXperiment (APEX) imaging spectrometer. *Atmospheric Measurement Techniques*, 5(9):2211–2225.

Postylyakov, O. (2004). Radiative transfer model MCC++ with evaluation of weighting functions in spherical atmosphere for use in retrieval algorithms. *Advances in Space Research*, 34(4):721–726.

Puķīte, J., Kühl, S., Deutschmann, T., Dörner, S., Jöckel, P., Platt, U., and Wagner, T. (2010). The effect of horizontal gradients and spatial measurement resolution on the retrieval of global vertical NO_2 distributions from SCIAMACHY measurements in limb only mode. *Atmospheric Measurement Techniques*, 3(4):1155–1174.

Pundt, I., Mettendorf, K.-U., Laepple, T., Knab, V., Xie, P., Lösch, J., Friedeburg, C., Platt, U., and Wagner, T. (2005). Measurements of trace gas distributions using Long-path DOAS-Tomography during the motorway campaign BAB II: experimental setup and results for NO_2. *Atmospheric Environment*, 39(5):967–975.

Richter, A., Eyring, V., Burrows, J. P., Bovensmann, H., Lauer, A., Sierk, B., and Crutzen, P. J. (2004). Satellite measurements of NO_2 from international shipping emissions. *Geophysical Research Letters*, 31(23).

Richter, A., Godin, S., Gomez, L., Hendrick, F., Hocke, K., Langerock, B., van Roozendael, M., and Wagner, T. (2013). Spatial Representativeness of NORS observations. Technical report, Network of Remote Sensing Ground-Based Observations for the GMES Atmospheric Service. available at: http://nors.aeronomie.be/projectdir/PDF/D4.4_NORS_SR.pdf, last access: 12 August 2020.

Richter, R. (1990). A fast atmospheric correction algorithm applied to Landsat TM images. *International Journal of Remote Sensing*, 11(1):159–166.

Rozanov, A., Rozanov, V., Buchwitz, M., Kokhanovsky, A., and Burrows, J. P. (2005). SCIATRAN 2.0–A new radiative transfer model for geophysical applications in the 175–2400nm spectral region. *Advances in Space Research*, 36(5):1015–1019.

Rozanov, V. V. and Rozanov, A. V. (2010). Differential optical absorption spectroscopy (DOAS) and air mass factor concept for a multiply scattering vertically inhomogeneous medium: theoretical consideration. *Atmospheric Measurement Techniques*, 3(3):751–780.

Russell, A. R., Valin, L. C., and Cohen, R. C. (2012). Trends in OMI NO_2 observations over the United States: effects of emission control technology and the economic recession. *Atmospheric Chemistry and Physics*, 12(24):12197–12209.

Schaepman, M. E., Jehle, M., Hueni, A., D'Odorico, P., Damm, A., Weyermann, J., Schneider, F. D., Laurent, V., Popp, C., Seidel, F. C., Lenhard, K., Gege, P., Küchler, C., Brazile, J., Kohler, P., De Vos, L., Meuleman, K., Meynart, R., Schläpfer, D., Kneubühler, M., and Itten, K. I. (2015). Advanced radiometry measurements and earth science applications with the Airborne Prism Experiment (APEX). *Remote Sensing of Environment*, 158:207–219.

Schaub, D., Brunner, D., Boersma, K. F., Keller, J., Folini, D., Buchmann, B., Berresheim, H., and Staehelin, J. (2007). SCIAMACHY tropospheric NO_2 over Switzerland: estimates of NO_x lifetimes and impact of the complex Alpine topography on the retrieval. *Atmospheric Chemistry and Physics*, 7(23):5971–5987.

Schönhardt, A., Altube, P., Gerilowski, K., Krautwurst, S., Hartmann, J., Meier, A. C., Richter, A., and Burrows, J. P. (2015). A wide field-of-view imaging DOAS instrument for two-dimensional trace gas mapping from aircraft. *Atmospheric Measurement Techniques*, 8(12):5113–5131.

Schwaerzel, M., Brunner, D., Jakub, F., Emde, C., Buchmann, B., Berne, A., and Kuhlmann, G. (2021). Impact of 3D radiative transfer on airborne NO_2 imaging remote sensing over cities with buildings. *Atmospheric Measurement Techniques*, 14(10):6469–6482.

Schwaerzel, M., Emde, C., Brunner, D., Morales, R., Wagner, T., Berne, A., Buchmann, B., and Kuhlmann, G. (2020). Three-dimensional radiative transfer effects on airborne and ground-based trace gas remote sensing. *Atmospheric Measurement Techniques*, 13(8):4277–4293.

Shettle, E. (1989). Models of aerosols, clouds and precipitation for atmospheric propagation studies. In *in AGARD, Atmospheric Propagation in the UV, Visible, IR and MM-Region and Related System Aspects*, volume CP-454. NATO Advisory Group for Aerospace Research and Development, Copenhagen, Denmark.

Solomon, S., Schmeltekopf, A. L., and Sanders, R. W. (1987). On the interpretation of zenith sky absorption measurements. *Journal of Geophysical Research*, 92(D7):8311–8319.

Spurr, R., Kurosu, T., and Chance, K. (2001). A linearized discrete ordinate radiative transfer model for atmospheric remote-sensing retrieval. *Journal of Quantitative Spectroscopy and Radiative Transfer*, 68(6):689–735.

Steinbacher, M., Fischer, A., Vollmer, M. K., Buchmann, B., Reimann, S., and Hüglin, C. (2007). Perennial observations of molecular hydrogen (H_2) at a suburban site in Switzerland. *Atmospheric Environment*, 41(10):2111–2124.

Strandgren, J., Krutz, D., Wilzewski, J., Paproth, C., Sebastian, I., Gurney, K. R., Liang, J., Roiger, A., and Butz, A. (2020). Towards spaceborne monitoring of localized CO_2 emissions: an instrument concept and first performance assessment. *Atmospheric Measurement Techniques*, 13(6):2887–2904.

Tack, F., Merlaud, A., Iordache, M.-D., Danckaert, T., Yu, H., Fayt, C., Meuleman, K., Deutsch, F., Fierens, F., and Van Roozendael, M. (2017). High-resolution mapping of the NO_2 spatial distribution over Belgian urban areas based on airborne APEX remote sensing. *Atmospheric Measurement Techniques*, 10(5):1665–1688.

Tack, F., Merlaud, A., Meier, A. C., Vlemmix, T., Ruhtz, T., Iordache, M.-D., Ge, X., van der Wal, L., Schuettemeyer, D., Ardelean, M., Calcan, A., Constantin, D., Schönhardt, A., Meuleman, K., Richter, A., and Van Roozendael, M. (2019). Intercomparison of four airborne imaging DOAS systems for tropospheric NO_2 mapping – the AROMAPEX campaign. *Atmospheric Measurement Techniques*, 12(1):211–236.

United States Committee on Extension to the Standard Atmosphere (1976). *US Standard Atmosphere*, volume 76. National Oceanic and Atmospheric Administration, National Oceanic and Atmospheric Administration and United States, United States Air Force, Washington D.C., United States.

Villefranque, N., Fournier, R., Couvreux, F., Blanco, S., Cornet, C., Eymet, V., Forest, V., and Tregan, J.-M. (2019). A Path-Tracing Monte Carlo Library for 3-D Radiative Transfer in

Highly Resolved Cloudy Atmospheres. *Journal of Advances in Modeling Earth Systems*, 11(8):2449–2473.

Vlemmix, T., Ge, X., de Goeij, B. T. G., van der Wal, L. F., Otter, G. C. J., Stammes, P., Wang, P., Merlaud, A., Schüttemeyer, D., Meier, A. C., Veefkind, J. P., and Levelt, P. F. (2017). Retrieval of tropospheric NO_2 columns over Berlin from high-resolution airborne observations with the spectrolite breadboard instrument. *Atmospheric Measurement Techniques Discussions*, 2017:1–34.

Wagner, T., Burrows, J. P., Deutschmann, T., Dix, B., von Friedeburg, C., Frieß, U., Hendrick, F., Heue, K.-P., Irie, H., Iwabuchi, H., Kanaya, Y., Keller, J., McLinden, C. A., Oetjen, H., Palazzi, E., Petritoli, A., Platt, U., Postylyakov, O., Pukite, J., Richter, A., van Roozendael, M., Rozanov, A., Rozanov, V., Sinreich, R., Sanghavi, S., and Wittrock, F. (2007). Comparison of box-air-mass-factors and radiances for Multiple-Axis Differential Optical Absorption Spectroscopy (MAX-DOAS) geometries calculated from different UV/visible radiative transfer models. *Atmospheric Chemistry and Physics*, 7(7):1809–1833.

Wagner, T., Dix, B. v., Friedeburg, C. v., Frieß, U., Sanghavi, S., Sinreich, R., and Platt, U. (2004). MAX-DOAS O_4 measurements: A new technique to derive information on atmospheric aerosols—Principles and information content. *Journal of Geophysical Research: Atmospheres*, 109(D22).

Wenig, M. O., Cede, A. M., Bucsela, E. J., Celarier, E. A., Boersma, K. F., Veefkind, J. P., Brinksma, E. J., Gleason, J. F., and Herman, J. R. (2008). Validation of OMI tropospheric NO_2 column densities using direct-Sun mode Brewer measurements at NASA Goddard Space Flight Center. *Journal of Geophysical Research*, 113(D16):D16S45.

World Health Organization (2021). *WHO global air quality guidelines: particulate matter (PM2.5 and PM10), ozone, nitrogen dioxide, sulfur dioxide and carbon monoxide*. World Health Organization.

Wu, F., Xie, P., Li, A., Chan, K., Hartl, A., Wang, Y., Si, F., Zeng, Y., Qin, M., Xu, J., et al. (2013). Observations of SO_2 and NO_2 by mobile DOAS in the Guangzhou eastern area during the Asian Games 2010. *Atmospheric Measurement Techniques*, 6(9):2277–2292.

Yu, H., Emde, C., Kylling, A., Veihelmann, B., Mayer, B., Stebel, K., and Van Roozendael, M. (2021). Impact of 3D Cloud Structures on the Atmospheric Trace Gas Products from UV-VIS Sounders – Part II: impact on NO_2 retrieval and mitigation strategies. *Atmospheric Measurement Techniques Discussions*, 2021:1–34.

Zhou, Y., Brunner, D., Hueglin, C., Henne, S., and Staehelin, J. (2012). Changes in OMI tropospheric NO_2 columns over Europe from 2004 to 2009 and the influence of meteorological variability. *Atmospheric Environment*, 46:482–495.

Marc Schwärzel

Email: marcschwaerzel@gmail.com
Phone: +41 79 226 63 87
ORCID: 0000-0002-5640-5870
Citizenship: Switzerland

Research interests

Air pollution, trace gas remote sensing, radiative transfer modelling, air quality monitoring

Education

École Polytechnique Fédérale de Lausanne — Lausanne, Switzerland
PhD student at Doctoral Program in Civil and Environmental Engineering
Mai 2018 – Present
Supervisors: Prof. Dr. Alexis Berne & Prof. Dr. Dominik Brunner

ETH Zürich — Zurich, Switzerland
Master in Atmospheric and Climate Science, Minor in Glaciology
September 2016 – March 2018
Master thesis supervisor: Prof. Dr. Thomas Peter

University of Lausanne — Lausanne, Switzerland
Bachelor in Environmental Sciences, Natural Sciences
September 2013 – July 2017
Bachelor thesis supervisor: Dr. Jean-Michel Fallot

Publications

Mapping the spatial distribution of NO_2 with in situ and remote sensing instruments during the Munich NO_2 imaging campaign
Kuhlmann, G., Chan, K. L., Donner, S., Zhu, Y., Schwaerzel, M., Dörner, S., Chen, J., Hueni, A., Nguyen, D. H., Damm, A., Schütt, A., Dietrich, F., Brunner, D., Liu, C., Buchmann, B., Wagner, T., and Wenig, M.
Atmospheric Measurement Techniques, 2022.

Impact of 3D radiative transfer on airborne NO_2 imaging remote sensing over cities with buildings
Schwaerzel, M., Brunner, D., Jakub, F., Emde, C., Buchmann, B., Berne, A., and Kuhlmann, G.
Atmospheric Measurement Techniques, 2021.

Three-dimensional radiative transfer effects on airborne and ground-based trace gas remote sensing
Schwaerzel, M., Emde, C., Brunner, D., Morales, R., Wagner, T., Berne, A., Buchmann, B., and Kuhlmann, G.
Atmospheric Measurement Techniques, 2020.

Research experience

Air Pollution and Environmental Technology, Empa

Mentors: Dominik Brunner & Gerrit Kuhlmann (Empa) April 2018 – Present

My work consists in development of the MYSTIC radiative transfer solver by implanting 3D and building features, their validation and the testing these new features. I also presented my results on divers occasions including other PhD students, my laboratory at Empa, an external lab at LMU and during conferences (poster and oral presentations).

Meteorological Institute Munich, LMU

Mentor: Claudia Emde (LMU) April 2019 – October 2019

During my exchange semester, I worked on an implementation of buildings and ground properties into the MYSTIC radiative transfer solver. I also attended the ”Monte Carlo Radiative Transfer” and ”Advanced Atmospheric Observation and Data Processing Techniques” lectures during my stay.

Air Pollution and Environmental Technology, Empa

Mentor: Joachim Mohn (Empa) September 2017 – March 2018

Master thesis with the title ”Development of an enhanced technique for accurate measurements of N_2O isotopes in ambient air”.

The goal of the Master thesis was developing a method to improve the N_2O isotopes measurement expanding the instrumental set-up. The used instrument is a laser spectrometer with a pre-concentration unit. The thesis included instrumental set-up development, instrumental calibration, measurement of standards, and presentation of results. The Master thesis is available on request or at the ETH library.

Teaching experience

Teaching assistant, Dept. of Civil, Environmental and Geomatic Engineering (ETH Zürich)

Fall 2021

ETH 102-0635-01L: Air Pollution Control

Correction of exercises, answer student question, correcting exams.

Teaching assistant, Department of Geography (University of Zurich)

Spring 2021

ESS 367: Remote Sensing of the Atmosphere

Answer questions during exercises, testing exam

Teaching assistant, Dept. of Civil, Environmental and Geomatic Engineering (ETH Zürich)

Fall 2020

ETH 102-0635-01L: Air Pollution Control

Extension of the lecture script, correction of exercises, answer student question, creating exam questions, correcting exams.

Teaching assistant, Department of Geography (University of Zurich)
Spring 2020
ESS 367: Remote Sensing of the Atmosphere
Testing exercises, answer questions during exercises, proofreading exam corrections

Teaching assistant, Dept. of Civil, Environmental and Geomatic Engineering (ETH Zürich)
Fall 2019
ETH 102-0635-01L: Air Pollution Control
correction of exercises, correcting exams.

Teaching assistant, Dept. of Civil, Environmental and Geomatic Engineering (ETH Zürich)
Fall 2018
ETH 102-0635-01L: Air Pollution Control
Extension of the lecture script, correction of exercises, answer student question, correcting exams.

Other experience

Empa, Dübendorf, Switzerland
Technical translator February 2018 - present
German-French translations for Empa press release and website.

Allenbach Transport SA, Nyon, Switzerland
Truck driver 2013 - 2017
Driving milk on weekends.

Talks and posters

Impact of 3D radiative transfer on NO_2 remote sensing over built-up areas December 2021
AGU Fall Meeting 2021 - Poster

Impact of 3D radiative transfer on airborne NO_2 imaging remote sensing over cities with buildings November 2021
Empa PhD Symposium - Poster

NO_2 Remote Sensing Over Built-Up Areas: The Effects Of 3D Radiative Transfer November 2021
esa ATMOS-2021 - Talk

Three-dimensional radiative transfer effects on airborne and ground-based trace gas remote sensing November 2020
Empa PhD Symposium - Talk

Effects of spatial variability of NO_2 concentrations on NO_2 remote sensing at city scale studied with a 3D radiative transfer model November 2019
Swiss Geoscience Meeting - Talk

Implementation Of Three-Dimensional Box-Air-Mass-Factors In The LibRadtran Radiative Transfer Model
esa ATMOS-2018 - Poster

Skills

Programming
Proficient in: programming Python
Good Knowledge in: C
Familiar with: programming Matlab, R, Bash, C++

Languages
French (mother tongue), German (mother tongue), English (advanced)

Other interests

Mountaineering, ski-touring, cycling, music, football

Other informations

Address: Querstrasse 4, 8600 Dübendorf; Marital status: single; Date of birth: 24.01.1993; Military service: fully completed; Driving licence: yes.